THESIS FOR THE DEGREE OF DOCTOR OF PHILOSOPHY

Electrochemical Capacitors for Miniaturized Self-powered Systems: Challenges and Solutions

Qi Li

Department of Microtechnology and Nanoscience

CHALMERS UNIVERSITY OF TECHNOLOGY

Gothenburg, Sweden 2020

Electrochemical Capacitors for Miniaturized Self-powered Systems: Challenges and Solutions

QI LI

ISBN 978-91-7905-313-0

Doktorsavhandlingar vid Chalmers tekniska högskola
Ny serie nr 4780
ISSN 0346-718X

Department of Microtechnology and Nanoscience
Chalmers University of Technology
SE–412 96 Göteborg, Sweden
Telephone + 46 (0) 31 – 772 1000

Cover: Photograph of a graphite / vertical cabon nanotubes material

Printed by Chalmers Reproservice
Gothenburg, Sweden 2020

To the fight against COVID-19

ABSTRACT

Electrochemical capacitors (ECs), also known as supercapacitors, are recognized as a key technology that will enable miniaturized self-powered systems, which will constitute the hardware base nodes of the internet of things (IoT), the internet of everything (IoE) and the tactile internet. Systems employing ECs can be designed to be maintenance-free thanks to the ultra-long cycling stability of ECs. Besides the function as a main or backup energy storage unit, advanced ECs can be used to support batteries at peak power load and they can be a substitute for conventional electrolytic capacitors used in a.c. line filtering, with clear advantages for system down-sizing due to their superior capacitance density.

However, a number of challenges remain to be solved to advance the development of ECs for miniature systems. Regarding the performance as a competitor to e.g. batteries, the ECs suffer from inferior energy density, low working voltage, severe self-discharge and leakage current. For IoT systems embedded in a harsh environment, the ability to enduring extreme temperature is inadequate for most general-purpose ECs. The response at high frequency needs to be enhanced to enable functions such as a.c. line filtering. As for encapsulation and integration, novel concepts are appreciated for compatibility with surface mount technology and reflow soldering, allowing convenient adaption in the form factor and making possible an arbitrary choice of EC materials (electrodes, electrolytes and separators).

To address the challenges, the thesis (1) explores the utilization of the redox electrolyte KBr to enhance the energy density of EDLCs; (2) adopts an ionic liquid electrolyte EMImAc to achieve working temperature beyond 120 °C; (3) uses an advanced graphite/VACNTs material for high-frequency ECs as a.c. line filters and low loss storage units in microsystems; (4) develops a bipolar EC prototype that doubles the working voltage limit; (5) mitigates the self-discharge and leakage current through the liquid crystal additive in an electrolyte; and (6) presents a cellulose-derived carbon nanofiber-based electrode material with enhanced capacitive performance.

Generic strategies and methods to address each identified challenge are provided in the thesis, highlighting a step-by-step optimization route starting from the material properties, moving on to the electrode structures, and further to the device design.

KEYWORDS

electrochemical capacitors, supercapacitors, energy storage, a.c. line filters, carbon, redox electrolytes, bipolar, encapsulation, miniaturized self-powered systems.

ACKNOWLEDGEMENTS

It feels like I have been expecting the year 2020 to come for a long time. Finally, it is here, and I am drawing a concluding mark on my Ph. D. student journey. This day would be impossible without help from a lot of wonderful people. I cannot mention every individual on this page, but certainly, every bit of your help is greatly appreciated and memorized!

My Ph. D. is financed by the European Union Horizon 2020 Research and Innovation program the smart-MEMPHIS and the Knut and Alice Wallenberg Foundation for Wallenberg Wood Science Center (WWSC). I also acknowledge the funding from Sweden's Innovation Agency Vinnova and Chalmers Area of Advance. Thanks to the Electronics Materials and Systems laboratory, Nanofabrication laboratory, and MC2 department for the administration and support of the infrastructures and resources.

I wish to address my sincere thanks to my examiner and main supervisor Peter Enoksson for taking me here in the Micro- and Nanosystems groups. I really appreciate your trust in me, and your help and guidance whenever I need it!

"Tusen tack" to my co-supervisor Per Lundgren. All our meetings and your constructive suggestions will be remembered, and your attitude towards work and life is really inspiring!

Thanks to my assistant supervisors Volodymyr Kuzmenko and Anderson Smith. Thank you Vova for your great advice especially in the early stage of my Ph.D., and the joyful lunches together! Thank you Andy for your help in the cleanroom and writing, and best wishes to your family!

Thank you to all my colleagues at Chalmers, in the smart-MEMPHIS, WWSC, and the iKnow-who project consortiums. It was a great pleasure to work and discuss with you!

I would also like to thank my master's program supervisors Prof. Guangshe Li and Prof. Liping Li who are now working at Jilin University, for your continuous care and advice!

Last but definitely not least – thank you all my friends, the happy gatherings, dinners, and travels together will never be forgotten! And deepest gratitude to my parents, grandparents, and family relatives for your endless support and understanding!

Göteborg, May 2020

QI LI

LIST OF PUBLICATIONS

This thesis is based on the following appended papers:

Paper I. Q. Li, M. Haque, V. Kuzmenko, N. Ramani, P. Lundgren, A. D. Smith, P. Enoksson. *Redox enhanced energy storage in an aqueous high-voltage electrochemical capacitor with a potassium bromide electrolyte.* Journal of Power Sources, 348 (2017) 219-228.

Paper II. M. Haque, Q. Li, V. Kuzmenko, E. Köhler, P. Lundgren, P. Enoksson. *Thermal influence on the electrochemical behavior of a supercapacitor containing an ionic liquid electrolyte.* Electrochimica Acta, 263 (2018) 249-260.

Paper III. Q. Li*, S. Sun*, A. D. Smith, P. Lundgren, Y. Fu, P. Su, T. Xu, L. Ye, L. Sun, J. Liu, P. Enoksson. *Compact and low loss electrochemical capacitors using a graphite / carbon nanotube hybrid material for miniaturized systems.* Journal of Power Sources, 412 (2019) 374-383. (*equal contribution)

Paper IV. J. Hansson*, Q. Li*, A. D. Smith, I. Zakaria, T. Nilsson, A. Nylander, L. Ye, P. Lundgren, J. Liu, P. Enoksson. *Bipolar electrochemical capacitors using double-sided carbon nanotubes on graphite electrodes.* Journal of Power Sources, 451 (2020) 227765. (*equal contribution)

Paper V. M. Haque, Q. Li, A. D. Smith, V. Kuzmenko, P. Rudquist, P. Lundgren, P. Enoksson. *Self-discharge and leakage current mitigation of neutral aqueous based supercapacitor by means of liquid crystal.* Journal of Power Sources, 453 (2020) 227897.

Paper VI. Q. Li, V. Kuzmenko, M. Haque, A. D. Smith, P. Lundgren, P. Enoksson. *Explanation of anomalous rate capability enhancement by manganese oxide incorporation in carbon nanofiber electrodes for electrochemical capacitors.* Electrochimica Acta, 340 (2020) 135921.

Contribution statements *(according to CRediT – Contributor Roles Taxonomy)*

Paper I: Conceptualization, Formal analysis, Investigation, Methodology, Project administration, Resources, Supervision, Validation, Visualization, Writing – original draft, Writing – review & editing

Paper II. Conceptualization, Formal analysis, Investigation, Methodology, Resources, Supervision, Validation, Visualization, Writing – review & editing

Paper III. Conceptualization, Formal analysis, Investigation, Methodology, Project administration, Resources, Supervision, Validation, Visualization, Writing – original draft, Writing – review & editing

Paper IV. Conceptualization, Formal analysis, Investigation, Methodology, Project administration, Resources, Supervision, Validation, Visualization, Writing – original draft, Writing – review & editing

Paper V. Conceptualization, Formal analysis, Investigation, Methodology, Resources, Supervision, Validation, Visualization, Writing – review & editing

Paper VI. Conceptualization, Formal analysis, Investigation, Methodology, Project administration, Resources, Supervision, Validation, Visualization, Writing – original draft, Writing – review & editing

Other journal publications not included in the thesis (Chronological order)

[**01**] A. Vyas, K. Wang, A. Anderson, A. Velasco, R. Eeckhoudt, M. Haque, **Q. Li**, A. Smith, P. Lundgren, P. Enoksson, *Enhanced electrode deposition for on-chip integrated micro-supercapacitors by controlled surface roughening.* ACS Omega, 5 (2020) 5219-5228.

[**02**] A. D. Smith, **Q. Li**, A. Vyas, M. Haque, K. Wang, A. Velasco, X. Zhang, S. Thurakkal, A. Quellmalz, F. Niklaus, K. Gylfason, P. Lundgren, P. Enoksson. *Carbon-based electrode materials for microsupercapacitors in self-powering sensor networks: Present and future development.* Sensors, 19 (2019) 4231.

[**03**] A. Vyas, **Q. Li**, F. Cornaglia, K. Wang, A. Anderson, M. Haque, V. Kuzmenko, A. D. Smith, P. Lundgren, P. Enoksson. *Surface roughening with iron nanoparticles for promoted adhesion of spin coated microsupercapacitor electrodes.* MRS Advances, 23 (2019) 1335-1340.

[**04**] G. Li, **Q. Li**, L. Li, J. Fan, Q. Ge, D. Xie, J. Zheng, G. Li. *Surface element segregation and electrical conductivity of lithium layered transition-metal oxide cathode materials.* Applied Surface Science, 427 (2018) 226-232.

[**05**] D. Xie, G. Li, **Q. Li**, C. Fu, J. Fan, L. Li. *Improved cycling stability of cobalt-free Li-rich oxides with a stable interface by dual doping.* Electrochimica Acta, 196 (2016) 505-516.

[**06**] Y. Zhang, L. Li, **Q. Li**, J. Fan, J. Zheng, G. Li. *Smart solution chemistry to Sn-containing intermetallic compounds through a self-disproportionation process.* Chemistry - A European Journal, 22 (2016) 14196-14204.

[**07**] **Q. Li**, G. Li, C. Fu, D. Luo, J. Fan, D. Xie, L. Li. *Balancing stability and specific energy in Li-rich cathodes for lithium ion batteries: a case study of a novel Li-Mn-Ni-Co oxide.* Journal of Materials Chemistry A, 3 (2015) 10592-10602.

[**08**] **Q. Li**, G. Li, C. Fu, D. Luo, J. Fan, J. Zheng, D. Xie, L. Li. *A study on storage characteristics of pristine Li-rich layered oxide* $Li_{1.2}Mn_{0.54}Co_{0.13}Ni_{0.13}O_2$*: effect of storage temperature and duration.* Electrochimica Acta, 154 (2015) 249-258.

[**09**] Y. Wang, L. Li, X. Huang, **Q. Li**, G. Li. *New insights into fluorinated* TiO_2 *(brookite, anatase and rutile) nanoparticles as efficient photocatalytic redox catalysts.* RSC Advances, 5 (2015) 34302-34313.

[**10**] D. Luo, G. Li, C. Fu, J. Zheng, J. Fan, **Q. Li**, L. Li, $LiMO_2$ (M = Mn, Co, Ni) hexagonal sheets with (101) facets for ultrafast charging-discharging lithium ion batteries, Journal of Power Sources, 276 (2015) 238-246.

[**11**] J. Fan, G. Li, D. Luo, C. Fu, **Q. Li**, J. Zheng, L. Li. *Hydrothermal-assisted synthesis of Li-rich layered oxide microspheres with high capacity and superior rate-capability as a cathode for lithium-ion batteries*. Electrochimica Acta, 173 (2015) 7-16.

[**12**] Y. Zhang, L. Li, J. Zheng, **Q. Li**, Y. Zuo, E. Yang, G. Li. *Two-step grain-growth kinetics of sub-7 nm* SnO_2 *nanocrystal under hydrothermal condition*. The Journal of Physical Chemistry C, 119 (2015) 19505-19512.

[**13**] S. Chen, L. Li, W. Hu, X. Huang, **Q. Li**, Y. Xu, Y. Zuo, G. Li. *Anchoring highconcentration oxygen vacancies at interfaces of* CeO_{2-x}/Cu *toward enhanced activity for preferential CO oxidation*. ACS Applied Materials Interfaces, 7 (2015) 22999-23007.

[**14**] **Q. Li**, G. Li, C. Fu, D. Luo, J. Fan, L. Li. *K-doped* $Li_{1.2}Mn_{0.54}Co_{0.13}Ni_{0.13}O_2$*: a novel cathode material with an enhanced cycling stability for lithium-ion batteries*. ACS Applied Materials Interfaces, 6 (2014) 10330-10341.

[**15**] D. Luo, G. Li, C. Fu, J. Zheng, J. Fan, **Q. Li**, L. Li. *A new spinel-layered Li-rich microsphere as a high-rate cathode material for Li-ion batteries*. Advanced Energy Materials, 4 (2014) 1400062.

[**16**] C. Fu, G. Li, D. Luo, **Q. Li**, J. Fan, L. Li. *Nickel-rich layered microspheres cathodes: lithium/nickel disordering and electrochemical performance*. ACS Applied Materials Interfaces, 6 (2014) 15822-15831.

Conference contributions and publications

[**01**] A. Velasco, A. Vyas, K. Wang, **Q. Li**, A. D. Smith, P. Lundgren, P. Enoksson. *Investigation of vertical carbon nanosheet growrth and its potential for microsupercapacitors*. 30th Micromechanics and Microsystems Europe (MME) workshop 2019, August 18-21, Oxford, United Kingdom.

[**02**] A. D. Smith, **Q. Li**, A. Anderson, A. Vyas, V. Kuzmenko, M. Haque, H. Staaf, P. Lundgren, P. Enoksson. *Toward CMOS compatible wafer-scale fabrication of carbon-based microsupercapacitors for IoT*. 17th Power MEMS 2017, November 14-17, Kanazawa, Japan. Paper in Journal of Physics: Conference Series, 1052 (2018), 012143.

[**03**] **Q. Li**, A. D. Smith, A. Vyas, F. Cornaglia, A. Anderson, M. Haque, V. Kuzmenko, E. Khöler, P. Enoksson. *Giving micro-supercapacitor fingers?* 29th Micromechanics and Microsystems Europe (MME) workshop 2018, August 26-29, Bratislava, Slovakia.

[**04**] A. Vyas, F. Cornaglia, T. Rattanasawatesun, **Q. Li**, M. Haque, J. Sun, V. Kuzmenko, A. D. Smith, P. Lundgren, P. Enoksson. *Investigation of palladium current collectors for vertical graphene-based microsupercapacitors*. 29th Micromechanics and Microsystems Europe (MME) workshop

2018, August 26-29, Bratislava, Slovakia. Paper in Journal of Physics: Conference Series, 1319 (2019) 012007.

[**05**] **Q. Li**. *Supercapacitors for miniaturized self-powered systems.* Supercapacitor: Store for the Future 2018, June 11-13, Gothenburg, Sweden.

[**06**] **Q. Li**, A. D. Smith, P. Lundgren, P. Enoksson. *Electrochemical capacitors as AC line filters for miniaturized system.* Micronano System Workshop MSW 2018, May 13-18, Espoo, Finland.

[**07**] **Q. Li**, A. D. Smith, M. Haque, V. Kuzmenko, E. Köhler, H. Staaf, A. Vyas, P. Lundgren, P. Enoksson. *A carbon based high frequency electrochemical capacitor for miniaturized smart systems.* MRS Spring Meeting 2018, April 2-6, Arizona, United States.

[**08**] **Q. Li**, A. D. Smith, M. Haque, V. Kuzmenko, P. Lundgren, P. Enoksson. *High voltage aqueous asymmetric supercapacitor with thin film* MnO_2 *and carbon nanotube electrodes.* Advanced Energy Materials 2017, September 11-13, Surrey, United Kingdom.

[**09**] **Q. Li**, A. D. Smith, M. Haque, A. Vyas, V. Kuzmenko, P. Lundgren, P. Enoksson. *Graphite paper/carbon nanotube composite: A potential supercapacitor electrode for powering microsystem technology.* 28th Micromechanics and Microsystems Europe (MME) workshop 2017, August 23-25, Uppsala, Sweden. Paper in Journal of Physics: Conference Series, 922 (2017) 012014.

[**10**] M. Haque, **Q. Li**, V. Kuzmenko, A. D. Smith, P. Enoksson. *Ionic liquid electrolyte for supercapacitor with high temperature compatibility.* 28th Micromechanics and Microsystems Europe (MME) workshop 2017, August 23-25, Uppsala, Sweden. Paper in Journal of Physics: Conference Series, 922 (2017) 012011.

[**11**] **Q. Li**, M. Haque, V. Kuzmenko, N. Ramani, P. Lundgren, A. D. Smith, P. Enoksson. *Redox enhanced supercapacitor with an aqueous potassium bromide electrolyte.* smart-MEMPHIS Summer School 2017, June 26-28, Valletta, Malta.

[**12**] **Q. Li**, V. Kuzmenko, M. Haque, P. Lundgren, E. Khöler, H. Staaf, P. Enoksson. *Nanocomposite materials for miniaturized supercapacitors.* International Conference and Exhibition on Integration Issues of Miniaturized Systems 2017, March 8-9, Cork, Ireland.

[**13**] E. Köhler, H. Staaf, V. Kuzmenko, **Q. Li**, P. Enoksson. *Flexible supercapacitor for high temperature applications.* PRiME (230th ECS Meeting) 2016, October 2-7, Hawaii, United States.

[**14**] **Q. Li**, V. Kuzmenko, M. Haque, P. Lundgren, P. Enoksson. *Freestanding 3D nano structured composite material with improved capacitive performance.* Nature Conference on Materials for Energy 2016, June 11-14, Wuhan, China.

Patent applications

[**01**] T. Braun, R. Kahle, P. Enoksson, P. Lundgren, **Q. Li**, Housing based on printed circuit board technology for energy storage devices, pending

[**02**] L. Li, **Q. Li**, C. Fu, G. Li, A lithium ion battery positive electrode material and preparation method, Publication number CN104091919B.

LIST OF ACRONYMS

5CB	--	4-n-pentyl-4′ -cyanobiphenyl
AAAS	--	American Association for the Advancement of Science
a.c.	--	alternating current
ACS	--	American Chemical Society
ABPBI	--	poly[2,5 benzimidazole]
AC	--	activated carbon
AN	--	acetonitrile
BMImCl	--	1-Butyl-3-methylimidazolium chloride
BQ	--	*p*-benzoquinone
CCD	--	cyclic charge/discharge
CDC	--	carbide-derived carbon
CN	--	cyanonitrile
CNTs	--	carbon nanotubes
COF	--	covalent organic framework
COTS	--	commercial off-the-shelf
CPR	--	capacitive potential range
CV	--	cyclic voltammogram / cyclic voltammetry
d.c.	--	direct current
DSGC	--	double-sided graphite/VACNTs
EC	--	electrochemical capacitor
EDCC	--	electrical double-cylinder capacitor
EDL	--	electrical double layer
EDLC	--	electrical double layer capacitor
EIS	--	electrochemical impedance spectroscopy
EMImAc	--	1-Ethyl-3-methylimidazolium acetate
EMImBF_4	--	1-Ethyl-3-methylimidazolium tetrafluoroborate
EMImTFSI	--	1-Ethyl-3-methylimidazolium bis(trifluoromethylsulfonyl)imide
EWCC	--	electrical wire-in-cylinder capacitor
GCD	--	galvanostatic charge/discharge
GO	--	graphene oxide
GPE	--	gel polymer electrolyte
HER	--	hydrogen evolution reaction
HOMO	--	highest unoccupied molecular orbital
IEC	--	International Electrochemical Commission
IEEE	--	Institute of Electrical and Electronics Engineers
IHP	--	inner Helmholtz plane
IL	--	ionic liquid
IoE	--	internet of everything
IOP	--	Institute of Physics

IoT -- internet of things
ITO -- indium tin oxide
LC -- liquid crystal
LDH -- layered double hydroxide
LIB -- lithium-ion battery
LIC -- lithium ion capacitor
LUMO -- lowest unoccupied molecular orbital
MOF -- metal-organic-framework
MPPT -- maximum power point tracking
MSC -- microsupercapacitors
MSPS -- miniaturized self-powered systems
NCNF -- nitrogen-doped carbon nanofiber
NHE -- normal hydrogen electrode
OER -- oxygen evolution reaction
OFG -- oxygen-containing functional groups
OHP -- outer Helmholtz plane
OLC -- onion-like carbon
PAA -- polyacrylic acid
PAMPS -- poly(2-acrylamido-2-methyl-1-propanesulfonic acid
PANI -- polyaniline
PBI -- poly-[2, 20-m-phenylene-5, 50-bibenzimidazole]
PC -- propylene carbonate
PCB -- printed circuit board
PE -- polyethylene
PEDOT:PSS -- poly(3,4-ethylenedioxythiophene) polystyrene sulfonate
PEEK -- polyether ether ketone
PEO -- polyethylene oxide
PIP$_{13}$FSI -- N-methyl-N-propylpiperidinium bis(fluorosulfonyl)imide
PMMA -- poly(methyl methacrylate)
PMPyrrTFSI -- 1-propyl-3-methylpyrrolidinium bis(trifluoromethylsulfonyl)imide
PMU -- power management unit
PP -- polypropylene
PPO -- poly(p-phenylene oxide)
Ppy -- polypyrrole
PSD -- pore size distribution
PTFE -- polytetrafluoroethylene
PVA -- polyvinyl alcohol
PVDF -- poly(vinylidene fluoride)
PVP -- polyvinyl pyrrolidone
PYR$_{14}$FSI -- N-butyl-N-methylpyrrolidinium bis(fluorosulfonyl)imide
PZV -- potential of zero voltage
rGO -- reduced graphene oxide

RT -- room temperature
SAE -- Society of Automotive Engineers
SBP BF_4 -- spiro-(1, 1')-bipyrrolidinium tetrafluoroborate
SCE -- saturated calomel electrode
SDS -- sodium dodecyl sulfate
SEI -- solid electrolyte interface
SoC -- state-of-charge
SPECS -- step potential electrochemical spectroscopy
SSA -- specific surface area
SSGC -- single-sided graphite/VACNTs
TEA BF_4 -- tetraethylammonium tetrafluoroborate
TEMA BF_4 -- triethylmethylammonium tetrafluoroborate
TLM -- transmission line model
TMD -- transition metal dichalcogenides
Triton X-100 -- p-t-octylophenol
UPD -- underpotential deposition
VACNT -- vertically aligned carbon nanotubes
VOGN -- vertically oriented graphene nanosheets
WiSE -- water-in-salts electrolyte

CONTENTS

CHAPTER 1

Introduction

1.1 Miniaturized self-powered systems

Human technology evolution has thrived on successful energy conversion: Starting from thermal energy by burning coal, converting to mechanical energy by steam engines, and further to electrical energy by the electromagnetic generators. Modern power plants worldwide serve our essential need for powering home appliances, factory machinery, and electric locomotives. With the aid of energy storage in batteries that can be re-charged at any location with access to wired-power, we extend the reach of cable-transmitted power to enjoy the convenience brought by portable electronics. However, with the emergence of wireless sensor networks and implantable medical devices in the era of the internet of things (IoT), seeking a new energy source becomes necessary since the conventional way of transmitting power from power plants to the new applications, either directly or via an energy storage, becomes difficult [1]. Specifically, in the IoT era, billions of devices are connected to the cloud, and well distributed to every location on the planet or even in space. Maintenance-free and energy-autonomous systems are in increasing demand as a more attractive option than to have to replace dead batteries.

If the energy from power plants can be perceived as *concentrated, ordered and high-quality*, there exists another type - *distributed* energy, which is *disordered* and *relatively low-quality*. The concentrated energy from power grids is fed into various applications and devices. Obeying the energy conservation law, the concentrated energy does not vanish, but is converted to different forms and distributed as radiation, motion, vibration, heat and chemical energy in the environment. The distributed energy is regarded as a new energy source for the IoT era [1]. By leveraging energy harvesting technologies (solar cells, thermoelectric, piezoelectric, triboelectric generators, etc.), distributed energy can be collected and used as an alternative to batteries for the IoT systems. Miniaturization is essential for IoT applications, and it also makes the "self-powered", i.e. energy-autonomous, concept feasible because the power consumption of miniature electronics can be as small as micro- to mili-watts. Being self-sustainable, IoT can be maximized to its full potential.

Miniaturized self-powered systems (MSPS) find applications in wearable personal electronics, industrial facilities, structure health monitoring, agriculture, transportation, military and medical care, etc. [2]. These systems comprise energy harvester, energy storage, functional device e.g. sensor, and control units, and can operate by themselves without an external power source. Design and fabrication of such systems in a constrained form factor are demanding, nevertheless, prototypes have been demonstrated. A representative system architecture schematic and device before and after the encapsulation is displayed in Figure 1. The fully encapsulated system is as small as 2×2×4.15 mm^3 with integrated solar cells as a harvester and a thin-film battery. A similar yet even smaller system of 1.5 mm^3 (1.5×2×0.5 mm^3) energy-autonomous wireless intraocular pressure sensor system was developed for intraocular pressure measurement of glaucoma patients [3]. The microsystem contains an integrated micro solar cell as the energy harvester, a thin-film micro-battery (1 µAh) as the storage unit, a MEMS pressure sensor, an integrated circuit including a wireless transceiver for wireless communication. All the components are encapsulated in a biocompatible glass housing. The system can achieve energy-autonomy by harvesting the solar energy that enters the eye through the transparent cornea so that it can be functional for years to convey a suitable glaucoma treatment. A similar microsystem was recently adapted for downhole environmental monitoring that is routinely required by the petroleum industry [4]. The size constraint is not as aggressive as in the former example, however, to achieve a higher spatial resolution of the sensed temperature and pressure in locations of narrow confines, the system size is still in the mm^3 range (2.9×1.1×1.5 mm^3 for the chip stack). With proper encapsulation in epoxy and stainless steel shell, the microsystem was able to perform tasks in a harsh environment (150 °C and 10000 psi in a concentrated brine, oil or cement slurry). With the advent of IoT, the demands for such systems will be ever-increasing, thereby calling for efforts in the development of suitable components for such applications.

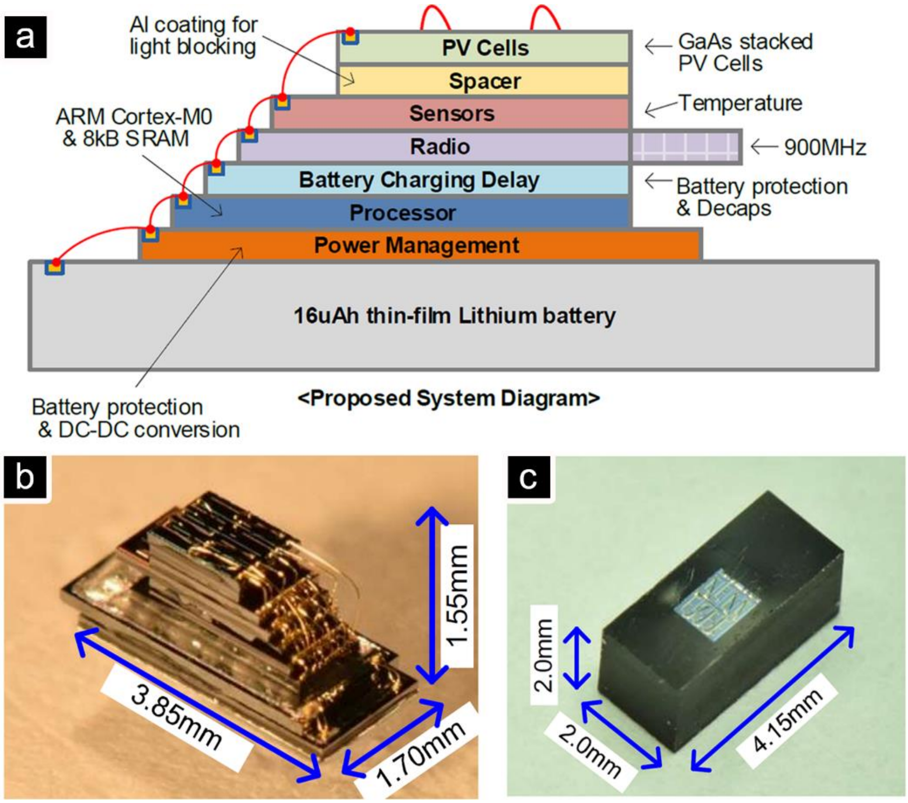

Figure 1. A miniaturized self-powered system. (a) Proposed system diagram; (b) System before encapsulation; (c) System after encapsulation [5]. (Reproduced with permission from IEEE)

1.2 Micro-storage options: why electrochemical capacitors

If the direct output from an energy harvester is sufficient to power the electronics in the microsystem, an energy storage unit may be omitted. This type of design sometimes requires oversizing of the energy harvester to ensure the output power, which necessarily increases the volume of the whole system [6]. Instead, with an energy storage unit, a smaller harvester can be implemented and the harvested energy can thus be accumulated and regulated. The storage unit also compensates for the intermittency of harvestable ambient energy. For example, a solar cell based self-powered system can rely on the stored energy to continue performing tasks during the night. This type of harvest-storage-use architecture of autonomous systems improves the quality of service.

The last few decades have witnessed a strong advancement of various energy storage technologies, from mechanical- (e.g. flywheel), electrochemical- (e.g. secondary batteries, flow batteries, electrochemical capacitors or supercapacitors), chemical- (e.g. fuel cells), electrical-, to thermal storage and their respective hybrids [7]. Considering the technology readiness in terms of miniaturization as well as environmental aspects, the electrochemical storage, with lithium-ion batteries (LIBs) and electrochemical capacitors (ECs, more often termed as supercapacitors) as representatives, is the most promising for practical applications in microsystems.

A device manufacturing procedure of slurry making, coating, tailoring, stacking and packaging for the production of pouch, prismatic and cylindrical cells has been optimized over the years [8]. The mature procedure dominates the LIBs and ECs markets for large storage devices and modules for consumer electronics, electric vehicles and stationary electrical infrastructures. Adapting LIBs and ECs for miniature systems poses several new challenges that require special attention. Miniaturization of energy storage devices has driven the research and development toward unconventional device configurations; including 2D stack, 2D in-plane, 3D in-plane, and 3D stack devices, as shown in Figure 2. The miniature unconventional storage devices are termed as *micro-storage devices*, referring to miniaturized storage devices that are designed and fabricated to serve as power sources or energy storage units in microelectronic devices [9, 10].

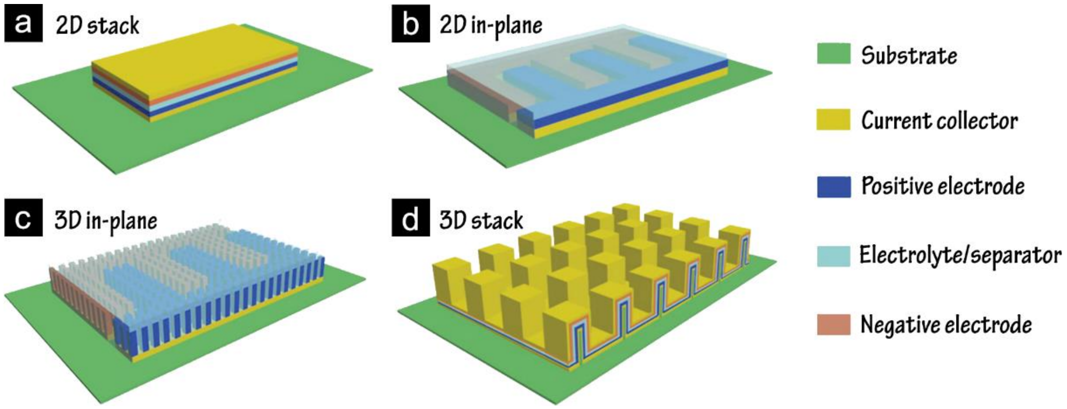

Figure 2. Micro-storage device configurations: (a) 2D stack, (b) 2D in-plane, (c) 3D in-plane and (d) 3D stack [9]. (Reproduced with permission from Wiley)

In general comparison, LIBs have a high energy density but moderate power density and cycling stability. On the other hand, ECs have complementary key performance, i.e. high power density and stability but low energy density. Which option fits better depends heavily on the system design in a specific case, however, ECs have gained increasing attention as a more suitable storage solution for miniaturized self-powered systems [2]. The reasons can be understood in association with the application scenario.

In principle, a high energy density of the storage unit is not the most prominent metrics in self-powered systems. Coupling with an energy harvester, energy input is “infinite”. If the storage unit has sufficient capacity in storing charges from a harvester and if it also satisfies other system demands, a higher energy density is unnecessary. This is different from conventional systems relying on a high-energy primary battery as the power source. The system comes to end-of-life when the battery is drained.

A more attractive feature for the storage unit in self-powered systems is that it can be continuously charged/discharged for a prolonged period, thus ensuring a longer lifespan of the system, fitting well the vision of maintenance-free, fit-and-forget IoT systems. The composition of the LIBs component is complex in its pristine state, and becomes even more complicated once the LIBs are being cycled, which gives poor prospects for obtaining long-term reliability. The classic ECs utilize high surface area carbon as electrodes with simpler composition, less complicated chemistry and lower extent of parasitic side reactions, therefore the cycling stability of ECs is up to 10^5 -10^6 cycles, sometimes referred to as “limitless”. The ultra-long cycle lifetime of ECs can eliminate the storage unit being any bottleneck of the system’s lifespan.

Bearing in mind that in self-powered systems, the output from energy harvesters, i.e. the input to charge the storage unit, is typically pulsed rather than constant. This requires the storage unit have a good capability of rapid charging with low resistance. In this regard, ECs outperform LIBs with their capacity for rapid energy intake.

Due to the distinct storage mechanisms, LIBs and ECs exhibit different charge/discharge characteristics. The LIBs often exhibit a plateau-like feature for the constant current charge/discharge profile, while for ECs, a typical feature is linear profiles starting from 0 V to its maximum operating voltage. As a result, a voltage converter together with a maximum power point tracking (MPPT) may be necessary for a LIB-embedded self-powered system to effectively charge a LIB at a relatively fast speed [11]. Power management is relatively more complicated [5] due to difficulties in the prediction of state-of-charge (SoC). For systems with ECs as storage units, MPPT and converters can be omitted since ECs can be trickle-charged from 0 V, without impairing their long term stability [6]. Power management is also easier for charge/discharge curve linearity. These imply that circuitry can be simplified, energy loss through converter can be avoided [11], and the size as well as the cost can be minimized in the case of using ECs as a storage unit.

Moreover, due to the hysteresis caused by mass transport and diffusion in solids, the energy efficiency of LIBs are usually lower than ECs. It is also generally acknowledged that the working temperature range of ECs is wider than that of LIBs. Besides, ECs can perform functions beyond energy storage (detailed in the next section) in electronic systems. A more complete list of advantageous aspects in terms of using ECs as storage units is summarized in **Table 1**. With all these said, we promote ECs as suitable micro-storage options in miniaturized self-powered systems.

Table 1. EC features and their implicative benefits when used in miniaturized self-powered systems.

Advantageous features	**Implicative benefits for self-powered systems**
Long cycle life	a. Eliminating the need for replacing batteries; b. Making maintenance-free systems.
High power density	a. Effectively absorbing the intermittent energy pulse from energy harvesters; b. Releasing burst energy (depending on the application e.g. RF transmitting).
High charge/discharge energy efficiency	a. Minimizing energy loss during energy conversion.
Linear charging curve	a. Indicating SoC; b. Allowing for easy behavior prediction, power management.
Can be charged from 0 V	a. Allowing for trickle charging; b. Simplifying charging circuitry, and converter-less design minimizing energy loss.
A wide temperature tolerance range	a. Being suitable for harsh environment applications.
Function beyond storing energy	a. Battery buffer, supporting peak power; b. Potentially replacing conventional capacitors e.g. electrolytic smoothing capacitors to downsize the system.

1.3 Functions of electrochemical capacitors beyond main energy storage

It is possible to use ECs for undertaking tasks beyond storing charges as the main storage unit (Figure 3a-b). Buffering batteries and a.c. (alternating current) line filtering are two examples in this regard. The two types of functions are valuable in miniaturized self-powered systems.

In autonomous sensor nodes, the system is usually programmed into active mode and sleeping mode to reduce power consumption. For example, the intraocular sensor mentioned in section 1.1 measures the eye pressure for 19.2 seconds (ca. 7.2 μW power consumption), then rest for 15 mins in the sleep mode (ca. 3.5 nW), and transmits data (ca. 48 mW for 0.13 s) once per day [3]. Different phases exhibit substantially different power consumption. Due to physical and chemical constraints, a battery often cannot supply a required high power while retaining its open-circuit voltage. Specifically, the 48 mW in the transmitting phase may cause over-discharge and thus be destructive for a micro-battery. Therefore, a buffer capacitor, also called hold-up capacitor, is connected in parallel to support peak power needs, leveling out the load on the batteries (Figure 3c-d). Other circumstances needing peak power includes data acquisition, data storage, micro-controller start-up, etc., which are common tasks for IoT systems. Implementing ECs to replace conventional capacitors can be beneficial for system miniaturization because of the higher capacitance density for ECs.

Perceiving the nature of ECs as a capacitor, the electrical response of ECs in ac circuits should exhibit a feature that the current leads voltage by 90°. Complying with this feature, ECs can smooth out ripple voltage in rectifying circuits (Figure 3e-f). Rectifying is needed in self-powered systems since the output from an energy harvester is often a.c. signals which need to be rectified for charging storage units. With a filter capacitor, the rectified signals become more steady and constant. The bigger capacitance the filter has, the smoother the signal will be, as the ripple voltage ΔV is defined as

$$\Delta V = \frac{I_L}{2f \cdot C} \qquad \text{Equation 1}$$

where I_L is the load current required for the application, f is the frequency of input signal and C is the capacitance of the smoothing capacitor. Because ECs vast superiority in charges per weight or volume compared to conventional capacitors, using ECs for such an application is beneficial for constructing compact systems that are pursued by the IoT technology.

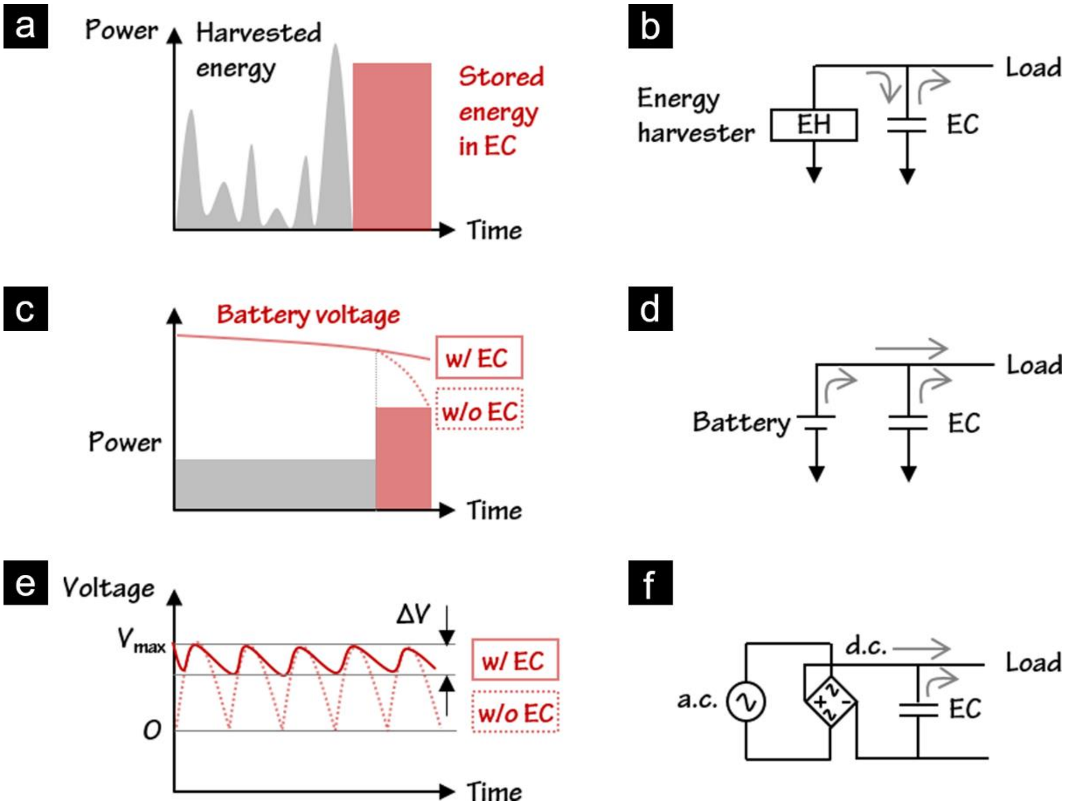

Figure 3. Schematic of types of functions for ECs. (a-b) Main storage unit in energy harvesting systems; (b-c) Battery load leveling; (e-f) a.c. line filtering.

1.4 Challenges facing electrochemical capacitors

Despite the advantageous aspects of ECs as discussed above, several challenges remain to boost their practical application in miniaturized self-powered systems. The nature of the challenge is usually application-specific; therefore, a neat classification of diverse challenges facing ECs in this field is not always possible. In this thesis, the challenges are grouped into two major categories. The first refers to achieving desired performance metrics depending on the role that ECs play in the system (energy storage, battery buffer or a.c. line filter), and the second group emphasizes the need for robust encapsulation and integration solutions that hermetically seal EC components while complying to specific form factor requirements. Similarities can be identified in the two categories; hence, the discussed aspects are cross-referenced in the different sections.

1.4.1 Device performance challenges

As an energy storage unit, the most common and critical benchmarking metrics are energy and power densities, cycling stability and efficiency. Although a high energy density is not the primary concern for self-powered systems, the need for improving ECs toward high energy content is still of paramount importance, because for the current state-of-art ECs, especially micro-scale ECs, energy density remains a bottleneck for their implementation in many IoT systems [12]. Another driver for pursuing high energy density ECs is to miniaturize the unit weight, area, and volume. In fact, for miniature systems, it is more beneficial to display high areal and volumetric energy, since the primary limitation in these systems is the footprint area or volume allocated for energy storage units, rather than the weight. In some cases, the optimization of energy density of ECs may eventually lead to a common battery system, posing a question of how to keep the capacitor-level power performance and cycling stability while increasing the storage capacity.

Self-discharge and leakage current also remain as a critical problem to be resolved, to minimize the loss of input energy from the micro energy harvester. If the leakage current of ECs is comparable to the charging current (can be as low as nA to μA), the ECs cannot be effectively charged, as the charging curve would deviate from linearity under low current charging. The deviation threatens the claimed benefits in Table 1. The leakage current usually increases with the increase of capacitance and voltage (energy). Knowledge and methodology in reducing leakage with no sacrifice in energy density are of great significance.

The Other important aspect is the pulse charge/discharge performance. In application scenarios where ECs are charged or discharged by short current pulses, the ability of rapid energy storage and release needs to be addressed. Power density and resistance are related parameters to be optimized, though the elimination of the semicircle appearing on the Nyquist plot (assignment of the semicircle to physical meaning differs in systems and reports) and the transmission-line effect caused by rich porosity may be more relevant. Unfortunately, this characterization and consideration of pulse charge/discharge performance have not yet been widely included in standard measurement protocols in the literature.

If ECs are adopted as a.c. line filters in IoT systems, the performance requirement is focused on a low RC time constant (ms range) of the EC, and at the same a high capacitance density (mF cm^{-2} range) to compete with electrolytic capacitors. As the capacitance *C* is a factor determining the RC time constant, a high capacitance inevitably decreases the high-frequency performance. Therefore, the manipulation of the RC product becomes a viable yet challenging topic. The maximum operating voltage is also of high importance for a.c. line filter ECs. Often 2-3 V may be sufficient for bypass and filtering purpose ECs in many electronic systems [13]. Such a voltage can be achieved with organic electrolyte systems, though the difficulty in realizing a good high-frequency response increases because of the more resistive nature of organic electrolytes compared with the aqueous counterparts. For the latter, the high voltage requires advanced designs and fabrication processes, e.g. bipolar configurations.

Durability in a harsh environment of extreme temperature and pressure, as well as in a corrosive medium, is also highly wanted and challenging to achieve for ECs. The warrant is in accordance with application cases of e.g. sensor nodes that are designed for a downhole environment with a depth of 12000 ft, temperature 125 °C, pressure 1000 to 6000 psi and salinity levels from 50000 to 150000 ppm [4, 14]. Exceeding temperature tolerance beyond 60 °C and -40 °C is a demanding task for state-of-art ECs. Addressing this issue can rely on component materials' thermal stability, especially the electrolyte. On the other hand, the tolerance limit may be extended by advanced encapsulation technology, especially for high pressure and corrosive environments [4].

As can be seen from above, several conflicting metrics can be identified that one improves at the cost of deteriorating the other, such as energy and power, leakage current and capacitance, leakage current and voltage, time constant and capacitance, etc. To some extent, the performance challenge is to minimize the trade-offs while improving the most critical metrics toward application requirements.

1.4.2 Device encapsulation and integration challenges

The goal of encapsulation is to isolate the EC components (electrodes, electrolytes, and separators) from the ambient humidity and atmosphere, to make ECs leakage-proof with good electrical insulation and good resistance to environmental extremes, thus guaranteeing long-term operation stability. We can find commercial off-the-shelf (COTS) ECs encapsulated as coin- or button-, cylindrical-, prismatic and pouch cells. These COTS devices are usually too bulky for miniature systems. While miniaturizing these configurations is possible [15] yet difficult, the storage device can become the limiting factor of further system sizing down [4].

The abovementioned COTS configurations can also present challenges in integrating ECs with other components. The existing COTS ECs have a limited choice of the positioning of positive and negative terminals, therefore, the system layout design is restricted and space efficiency may not be optimized. Comparably, surface mount configurations are beneficial to save space and convenient for integration. New EC encapsulation and integration concepts that allow for easy geometry tailoring and arbitrary assigning the location of terminals is therefore desired for miniaturization and seamless integration.

Moreover, many concurrent encapsulation and packaging techniques for printed circuit board (PCB) electronics, such as reflow soldering [16], are high-temperature processes, which require the ECs to withstand elevated temperature (more than 100 °C) for a certain period [17]. Therefore, high-temperature durability is of great interest. This aspect overlaps with the performance challenges in a harsh environment, which relies on the development of specialized electrolytes. But if any low-temperature encapsulation/integration concept can be adopted, the library of usable electrolyte options can be significantly widened.

The major challenges facing ECs for their application in miniaturized self-powered systems are summarized as follows. The solutions to the challenges would rely on the development of interdisciplinary themes.

Device performance challenges

- Improving energy density while keeping high power density and long cycling stability
- Increasing the maximum operating voltage limit
- Achieving high power density at extreme low-temperature, and high stability at extreme high-temperature
- Strengthening efficiency in pulse charging and discharging
- Minimizing the self-discharge and leakage current
- Enhancing frequency response properties with a high capacitance density

Device encapsulation/integration challenges

- Developing new encapsulation and integration concepts allowing for surface mounting with a low profile and compatibility with a wide choice of materials
- Enhancing the tolerance to high-temperature exposure that is required for reflow soldering and/or other encapsulation and integration method.

1.5 Scope of the thesis

This thesis mainly focuses on the strategies and methods for the identified challenges. Several topical mini-reviews of state-of-art development in diverse sections have been included. The thesis research work, i.e. the appended publications, is interwoven with the review in the corresponding categories, elaborated together with the advantages, but also the limitations, concerning the applications.

Except for some specialized requirements in miniaturized self-powered systems, the extensive summary of strategies and methods are also applicable to the R&D of EC in other application fields.

The thesis layout is as follows: Chapter 1 introduces the application background, and the challenges facing ECs in the specific application. Chapter 2 elucidates the fundamentals, performance metrics, and evaluation methods. Chapter 3 explores the solutions to device performance problems. Chapter 4 focuses on encapsulation and integration aspects. Chapter 5 summarizes the thesis and discusses prospects.Chapter 6 presents an executive summary of each appended research publication.

This Ph.D. dissertation thesis is an extension of the author’s licentiate thesis through the reorganization and implementation of supplementary and new perspectives. It is also an aim that the thesis can serve as a quick reference and be helpful to students at Chalmers who are new to the relevant research topics.

CHAPTER 2

Fundamentals of electrochemical capacitors

2.1 Charge storage mechanisms

Three main categories of charge mechanisms are identified: electrical double layer, pseudocapacitive and battery-type. Understanding these mechanisms is essential for efficient device design towards diverse applications.

2.1.1 Electrical double layer

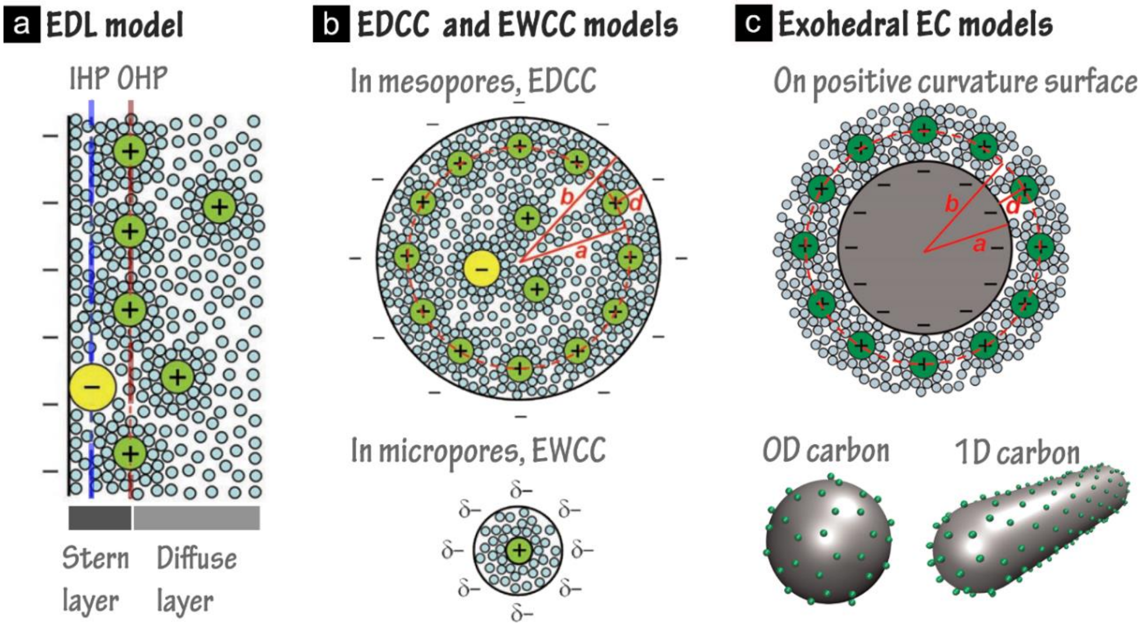

Figure 4. EDL theory models. (a) The classic EDL model on a negatively charged planar surface [18]; (b) EDCC and EWCC models [18]. (c) Exohedral EC models with a cross-section view of exohedral capacitor, and schematics of surface charge on 0D spherical and 1D cylindrical carbon [19]. (Reproduced with permission from Wiley and MRS)

The electrical double layer (EDL) mechanism refers to charge storage via the reversible electrostatic accumulation of ions on the surface, forming an electrical double layer structure at the interface between the electrode and electrolyte. No charge transfer or Faradaic process occurs across the interface. The capacitance via EDL storage mechanism can be estimated using Helmholtz model that considers a simplified parallel plate capacitor [20]

$$C_{EDL} = \frac{\varepsilon_r \varepsilon_0 \times A}{d} \qquad \text{Equation 2}$$

where ε_r is the dielectric constant related to the electrolyte, ε_0 is the vacuum permittivity, A is the accessible surface area to electrolyte ions, and d is the charge separation distance. With Debye length (5 – 10 Å, depending on electrolyte concentration and the dimension of ions and solvation shell) as the charge separation distance, the area normalized capacitance for carbon electrodes is in the range of 10 – 21 μF cm^{-2}. A porous electrode can have a high specific surface area (SSA) more than 1000 m^2 g^{-1}, and a specific capacitance up to 200 F g^{-1}.

The simple Helmholtz model [20] was later modified by Gouy [21], Chapman [22] and Stern [23], and came to a classic EDL structure including the Stern layer (inner Helmholtz plane IHP and outer Helmholtz plane OHP) and a diffuse layer. With the advancement of nanomaterials, new EDL structures were proposed to account for the influence of electrode surface curvature. The classic parallel plate capacitor model (Figure 4a) is eligible for macropore regions (> 50 nm), while for mesopore regions (2 – 50 nm), the counter ions enter the mesopore forming an electrical double-cylinder capacitor (EDCC, Figure 4b) [18], and for micropore regions (< 2 nm), solvated/desolvated counter ions line up along the pore axis to form an electrical wire-in-cylinder capacitor (EWCC, Figure 4b) [18, 19]. The new models allow the explanation of some anomalous phenomena e.g. an anomalous increase in capacitance at pores smaller than the solvated electrolyte ions [24]. Moreover, taking into account the curvature influence, the exohedral EC models (**Figure 4**c) were proposed to account for the charge storage on 0D and 1D carbon materials with positive curvature.

The electrochemical signature of the EDL mechanism is characterized by a rectangular shape in cyclic voltammograms (CV), and linear curves in galvanostatic charge/discharge (GCD) response.

2.1.2 Pseudocapacitive storage

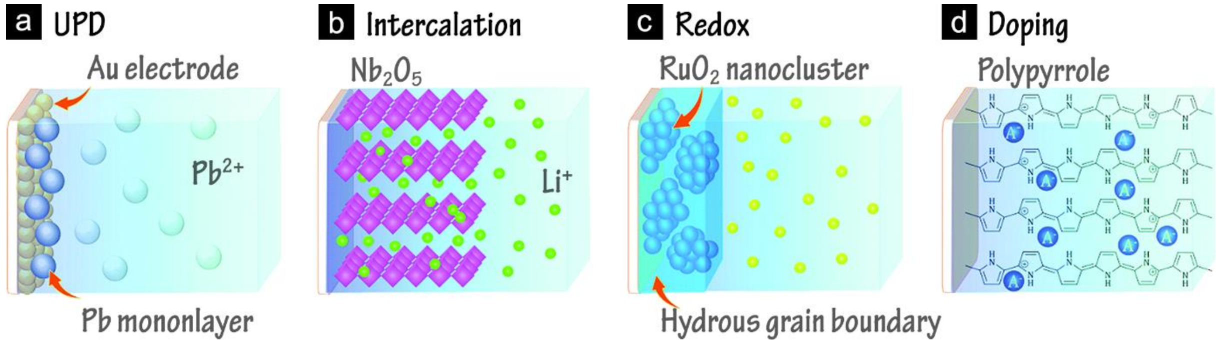

Figure 5. Pseudocapacitive mechanisms [25]. (a) Underpotential deposition e.g. Au/Pb; (b) Intercalation pseudocapacitance e.g. Nb_2O_5; (c) Redox pseudocapacitance e.g. RuO_2; (d) Doping pseudocapacitance e.g. polypyrrole. (Reproduced with permission from RSC)

Pseudocapacitive mechanism refers to reversible fast surface-confined redox reactions. The nature of the pseudocapacitive mechanism is the Faradaic process involving electron transfer across the interface, but the electrochemical signature is capacitive. The identified pseudocapacitance mechanisms include:

(1) Underpotential deposition (UPD) pseudocapacitance

The UPD is a process of electrodeposition of metal species M on a substrate metal S at a potential less negative than the equilibrium potential for the reduction of M. An example is shown in Figure 5a for Pb deposition on Au:

$$Au + xPb^{2+} + 2xe^{-} \leftrightarrow Au \cdot xPb_{ads.} \qquad \text{Equation 3}$$

The formation of M is usually monolayer sorption over a surface, therefore the UPD is regarded as a 2D process [26].

(2) Intercalation pseudocapacitance

Intercalation pseudocapacitance is the insertion of ions into the layered host structure without triggering phase transformation, such as lithium intercalation in Nb_2O_5 (Figure 5b):

$$Nb_2O_5 + xLi^{+} + xe^{-} \leftrightarrow Li_xNb_2O_5 \qquad \text{Equation 4}$$

The intercalation process is considered as a *quasi*-2D process as the intercalation takes place between alternating 2D gaps between the 3D layered host structure [26].

(3) Redox pseudocapacitance

For the redox pseudocapacitance, it occurs when ions are adsorbed on or near the surface of an electrode, or sometimes protons are inserted into the host structure which is similar to the quasi-2D intercalation process [26]. A typical redox pseudocapacitive materials is RuO_2, as shown in Figure 5c:

$$RuO_x(OH)_y + \delta H^{+} + \delta e^{-} \leftrightarrow RuO_{x-\delta}(OH)_{y+\delta} \qquad \text{Equation 5}$$

(4) Doping pseudocapacitance

As for the doping pseudocapacitance, it refers to charge storage in conjugated conducting polymer materials with the capability of being electrochemically oxidized or reduced by withdrawing or injection of electrons, and the terms of p-doping and n-doping originating from semiconductor science are used to describe the oxidation and reduction, respectively. As sketched in Figure 5d, the pseudocapacitance of conducting polymer *PPy* is through the reaction

$$PPy \cdot nA^{-} + ne^{-} \leftrightarrow PPy + nA^{-} \qquad \text{Equation 6}$$

The charge storage is a quasi-1D process along the polymer chains [27] (Chap 12 p318). Doping pseudocapacitance can be regarded as a specific type of redox pseudocapacitance.

From the perspective of thermodynamics, all the four pseudocapacitive mechanisms feature a quantity y, which is proportional to the stored charge, satisfying a universal relation with respect to electrode potential E in the following format [27] (Chap 10).

$$\frac{y}{1-y} = K \exp(\frac{EF}{RT}) \qquad \text{Equation 7}$$

where K is a constant specific to each system, E is the potential of the electrode at equilibrium, F is the Faraday constant, R is the gas constant and T is the temperature, the correspondence of y and its conventional symbol as well as the physical meaning for each mechanism is specified in Table 2.

The form of the function originates from Langmuir type isotherm for UPD processes with the variant y in above eq. referring to a fractional coverage of absorbate, in the symbol of θ. Solving the equation, the expression of θ with respect to E can be obtained

$$\theta = \frac{K\exp(\frac{EF}{RT})}{1+K\exp(\frac{EF}{RT})} \qquad \text{Equation 8}$$

Since the amount of charge is proportional to the coverage for the UPD, then the pseudocapacitance is defined

$$C_{\varphi} = q_{\theta=1}\frac{d\theta}{dE} \qquad \text{Equation 9}$$

where $q_{\theta=1}$ is the amount of charge at full surface monolayer coverage. Combining Equations 8-9, it can be solved

$$C_{\varphi} = \frac{q_{\theta=1}F}{RT}\theta(1-\theta) \qquad \text{Equation 10}$$

The Langmuir model above does not consider any interaction among the absorbates and substrate atoms, therefore a lateral interaction term $g\theta$ is introduced to the isotherm for a more realistic model:

$$\frac{\theta}{1-\theta} = K\exp(-g\theta)\exp(\frac{EF}{RT}) \qquad \text{Equation 11}$$

then the pseudocapacitance is expressed as

$$C_{\varphi} = \frac{q_{\theta=1}F}{RT}\frac{\theta(1-\theta)}{1+g\theta(1-\theta)} \qquad \text{Equation 12}$$

When g is greater than 0, the interaction is repulsive, which means the deposition process becomes more difficult (as a result, the higher potential is required) as the surface is covered by absorbates. When g is smaller than 0, the interaction is attractive in general, suggesting that the deposition is more facile when the coverage θ increases, hence a steeper slope for the θ vs. E isotherm. When $g = 0$, it represents the ideal Langmuir model.

The introduction of the parameter g allows us to mathematically describe how the pseudocapacitive mechanism originates from Faradaic processes but exhibits a capacitive electrochemical response. Figure 6 compares the theoretical response in linear sweep voltammograms for different scenarios of g signs and values. When θ is in the intermediate range 0.3 to 0.7 and g is at an appreciable value (e.g. g greater than 4), the fractional coverage θ changes linearly with E, the pseudocapacitance is stretched over a wider range of potential than for the case of negative g values (Figure 6a), thus the response is highly analogous to that of EDL mechanism (the shadowed region in Figure 6c, d). When more than one reaction is occurring successively with overlapping in their potential ranges, the apparent capacitance can be maintained at an almost constant value over a wide range potential [28]. Besides, the capacitive response i.e. constant current flow with a linear variation of potential, for pseudocapacitive materials was explained qualitatively using band theory [29].

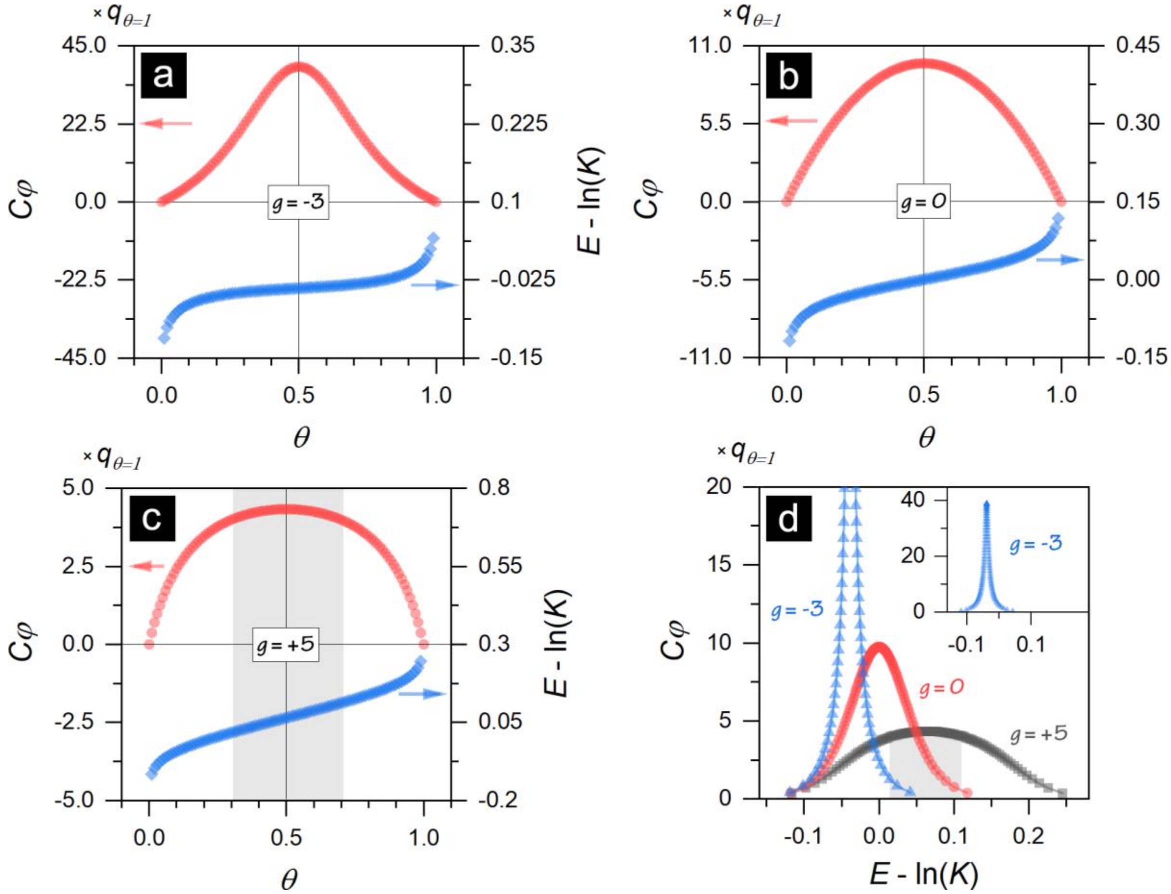

Figure 6. The patterns of pseudocapacitance C_φ and potent E variation at different g values. C_φ and E as a fuction of θ at (a) g = -3, (b) g = 0, and (c) g = 5; (d) C_φ as a function of E. Plotted per Equation 11-12, at T = 298 K.

The surface-confined processes discussed above proceed under equilibrium or quasi-equilibrium conditions. For each coverage value θ, it corresponds to an equilibrium potential E, which is in the form of Nernst equation for relative extents of vacancy 1-θ and occupancy θ of surface sites [26]

$$E = E^0 + \frac{RT}{zF}\ln(\frac{\theta}{1-\theta}) \qquad \text{Equation 13}$$

where E^0 is the standard electrode potential, z is the number of electrons transferred in the cell reaction, and R, T and F follow the meanings in Equation 7. The Nernstian form equations for all the pseudocapacitive mechanisms are summarized in Table 2. These relationships describe the thermodynamic basis of pseudocapacitances, however, the practical use of these materials for EC technology is in their fast kinetics. Hence, the pseudocapacitive reaction should occur at the surface, free from diffusion-control, without phase transformation and is highly reversible. The typical electrochemical signature is preferably close to EDL type with no peak appearance on a CV curve, and linear GCD profiles. It is also broadly defined that pseudocapacitance is counted in the case that peaks are present in the CV, given that the peaks are broad and exhibit small peak-to-peak separation [30]. The corresponding GCD curve is sloping with no distinct plateau, and the voltage hysteresis is small. These features need to be satisfied in the time domain of about 10 s to 10 min for pseudocapacitance, to distinguish it from high power batteries [30].

To meet the kinetics requirement for pseudocapacitance, the reaction center that contributes to the Faradaic pseudocapacitance should be located near the surface of the oxide, at a distance, $l \ll (2Dt)^{1/2}$ [31], where D is the diffusion coefficient for charge-compensating ions, and t is time. Nanosizing the materials can improve kinetics to a great extent by reducing the diffusion pathway, and can even make typical battery material exhibit capacitive response. In this regard, the term *intrinsic* and *extrinsic* pseudocapacitance are proposed. Intrinsic refers to materials that are capacitive regardless of their particle size and morphologies, and extrinsic refers to materials which exhibit capacitance only in nano-size particles and not in bulk states, e.g. nano-size $LiCoO_2$ [32].

Table 2. The Nernstian form of equations for pseudocapacitive mechanisms

Mechanism	Nernst form	symbol meaning
Underpotential deposition	$E = E^0 + \frac{RT}{zF}\ln\left(\frac{\theta}{1-\theta}\right)$	θ, Fractional site occupancy
Intercalation	$E = E^0 + \frac{RT}{zF}\ln\left(\frac{X}{1-X}\right)$	X, fractional lattice site occupancy
Redox	$E = E^0 + \frac{RT}{zF}\ln\left(\frac{R}{1-R}\right)$	R = [Ox]/([Ox]+[Red])
Doping	$E = E^0 + \frac{RT}{zF}\ln\left(\frac{R}{1-R}\right)$	R, fractional extent of oxidation of the polymer chain

2.1.3 Battery-type mechanism

The battery-type mechanism is also redox Faradaic reactions in nature, involving electron transfer across the interface, similar to pseudocapacitance. The distinction to pseudocapacitive mechanism is that the electrochemical signatures for battery-type are non-capacitive, so that sharp peaks appear on CV, and plateaus are displayed upon GCD. A number of materials exhibit state-of-charge dependence on the potential for fundamental thermodynamic reasons (e.g. rechargeable battery materials show sloping discharge curves defined by Gibbs phase rule) but are not regarded as pseudocapacitive materials because of slow kinetics due to a diffusion-controlled polarization in solid phase or liquid phase (redox electrolyte). For the battery-type mechanism, the peak separation on CV increases appreciably when increasing the sweep rate, and the voltage hysteresis of GCD curves is significantly enlarged with an increase in current density.

2.1.4 Distinguishing capacitive and non-capacitive contributions

Distinguishing capacitive (EDL- or pseudocapacitive) mechanism from non-capacitive ones (battery-type) is essential to correctly characterize the charge storage ability of the materials [31]. With the fast advancement of materials science, there is an increasing number of new materials that display electrochemical signatures neither purely capacitive nor purely battery-like [33]. This has caused some incorrect reports using capacitance for non-capacitive materials. This problem has been emphasized in recent critical reviews [34-36] to arouse attention in standardizing. For obvious battery-type behaviors, the use of "capacitance" should be avoided, instead, capacity in units of Ah g^{-1} or C g^{-1} should be reported.

With a given material, decomposing the overall storage into capacitive and non-capacitive contributions provides means of understanding the charge/discharge mechanisms that are operating. The electrode kinetics difference makes the decomposition possible using electrochemical methods, which includes (1) *i-v* dependence (the response current dependence on sweep rate in CV), (2) *q-v* dependence (voltammetric charge dependence on sweep rate in CV) and (3) step potential electrochemical spectroscopy (SPECS).

Table 3. The limitation of methods for distinguishing capacitive and non-capacitive contributions

Method	Limitations
i-v	Non-linear fitting for large sweep rate range; Inaccuracy at high sweep rates for peak-shaped CVs due to peak shifting and broadening [37, 38].
q-v	Non-linear fitting of equations for desired sweep rate range [39]; Unrealistic assumptions (infinite/zero sweep rate);
SPECS	Time-consuming in data collection and analysis; The mathematical fitting might generate multiple solutions and physically meaningless parameters.

The advantages and disadvantages of the three methods are compared in ref. [40]. The limitations of these methods are displayed in Table 3. In general, the *q-v* method may overestimate the diffusion-controlled contribution as well as overall capacitance, because the method is based on extrapolation to either finite or zero sweep rate. Both *i-v* and *q-v* methods have a limitation that they should be used at low sweep rate ranges. For the SPECS method, although it is comparably more time consuming, this method can differentiate the capacitive and diffusion-controlled and residual processes over a wide range of sweep rates and potentials. However, it is not mentioned in the comparison but what might be a problem for SPECS is that the mathematical fitting can result in multiple solutions and unrealistic parameters. Therefore, preferably these methods are corroborated with other techniques.

2.2 Device classifications

ECs can be classified according to diverse principles. For example, depending on the working mechanism, the devices can be specified as electrical double-layer capacitors (EDLCs), pseudocapacitors, etc.; depending on the device configuration, the term symmetric and asymmetric devices can be applied. The definition for the terms is not always unified in reports, especially when it comes to "hybrid" types. Here in this thesis, the definitions for the terms are clarified in Table 4.

Table 4. The classification of ECs

Classification principle	Term	Components		
		Electrode 1	Electrode 2	Electrolyte
Mechanism	EDLC	EDL	EDL	Regular
	Pseudocapacitor	Pseudocapacitive	Pseudocapacitive	Regular
		Pseudocapacitive	EDL	Regular
	Hybrid device	Battery-type	Capacitive	Regular
		Capacitive	Capacitive	Redox
Configuration	Symmetric device	With two identical electrodes (material, mass, etc.)		Arbitrary
	Asymmetric device	With two different materials as electrodes, or the same material but in different weight		Arbitrary

2.3 Performance characteristics and evaluation

The evaluation of performance characteristics is the foundation of understanding the materials and devices concerning their applications. In this section, the common electrochemical evaluation methods will be introduced, and the key performance characteristics of ECs are clarified. In general, obtaining a set of data from the measurement instrument is straightforward, however, the interpretation of data requires special attention. There is a certain inconsistency in performance normalization in both academia and the industry. The concerns are discussed and particular issues in the application for miniaturized self-powered systems are highlighted.

2.3.1 Performance evaluation methods

2.3.1.1 Measurement techniques

The commonly applied techniques can be grouped as d.c. methods and a.c. methods. The former include cyclic voltammetry (CV), chronopotentiometry (galvanostatic charge/discharge, GCD), etc., and the latter is mainly electrochemical impedance spectroscopy (EIS). The d.c. methods are favorable for transient state study, and the EIS is used to investigate the steady-state of the material or device, hence, EIS data is preferable to be acquired when the studied subject reaches its equilibrium.

(1) Cyclic voltammetry (CV)

CV is a versatile technique that can provide a semi-quantitative study on kinetics, storage mechanisms, voltage window, etc. This technique imposes a linear voltage sweep loop within the voltage window and records the responding current. For a simple series RC circuit, as shown in Figure 7a, the current response is expressed as

$$i = vC\left(1 - \exp(-\frac{t}{RC})\right)$$ Equation 14

The response of the RC circuit differs from the ideal capacitor by exhibiting blunt corners due to the effect of the series resistance.

(2) Galvanostatic charge/discharge (GCD)

GCD is a chronopotentiometry method that applies a constant current to charge the device to its maximum voltage and discharge to its minimum. This test resembles the practical application scenario of many storage devices. The important characteristics can be extracted are the resistance, capacitance or capacity, energy and power densities. By repeating the GCD measurements, the evolution of different metrics can be mapped, therefore, the stability can be evaluated.

For a series R-C circuit (Figure 7b), the voltage variation follows the equation

$$V = IR + I\frac{t}{C}$$ Equation 15

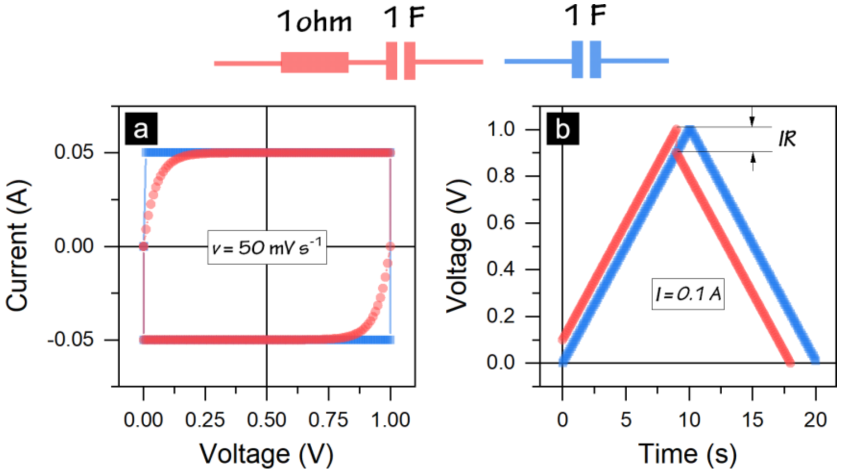

Figure 7. Simulated CV and GCD curves for a series R-C and a single C circuits, with R = 1 ohm and C = 1 F. (a) CV response at 50 mV s^{-1} sweep rate; (b) GCD response at 0.1 A current.

(3) electrochemical impedance spectroscopy (EIS)

The EIS technique excites the material or device with a small amplitude of the voltage or current in the form of sinusoidal signals. The frequency of the signals varies from mHz to kHz, therefore, information about different processes occurring at different time scales can be differentiated. As the excitation is small, a linear relation following the form of Ohm's law exists over the frequency range

$$V = IZ$$ Equation 16

where Z is the impedance. Applying Euler's formula, the impedance under the sinusoidal excitations can be formulated in a complex form

$$Z = Z_{Re} + jZ_{Im}$$ Equation 17

The impedance data is presented as a Nyquist plot or Bode plot. Equivalent circuits that exhibit the same impedance of the electrochemical system can be developed for a better understanding of the reaction kinetics. Figure 7 presented above are simplified circuits, the actual devices are much more complicated. The physical interpretation of the same type of impedance can be found multiple and often contradictory in literature [41], therefore, special care is needed when fitting the impedance to a particular circuit.

2.3.1.2 Electrochemical cells

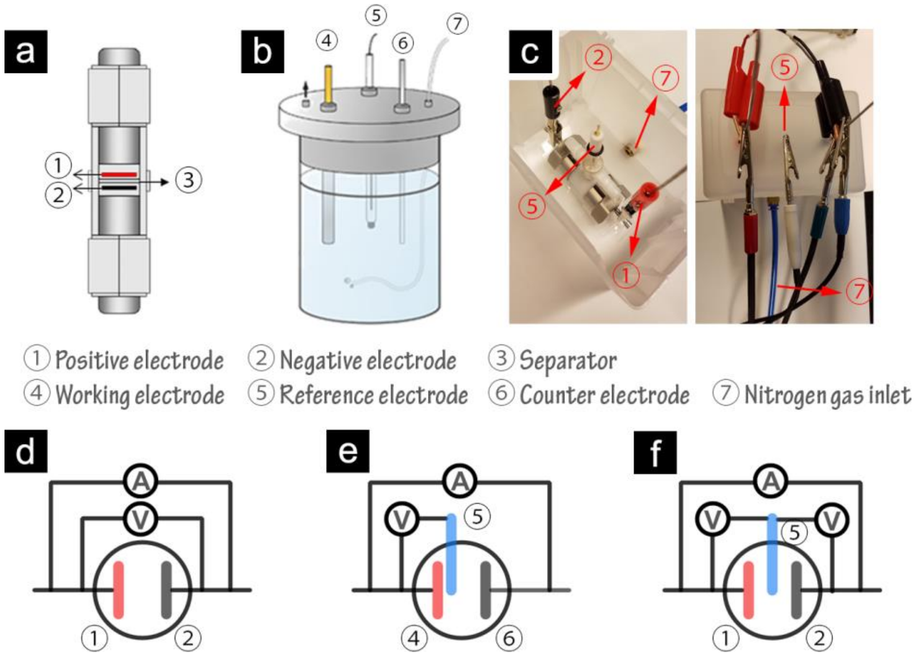

Figure 8. Measurement setups. (a, d) Two-electrode system: Swagelok cell; (b, e) Conventional three-electrode cell; (c, f) Modified three-electrode system: T-type Swagelok cell.

The electrochemical measurements can be performed with different configurations of cells (Figure 8). The two-electrode cell mimics the structure of a practical device, where the current and voltage across the positive and negative electrodes are recorded. The conventional three-electrode allows the investigation of the properties of a material in an electrolyte. The current flows through the working electrode (the studied material) and counter electrode, while the potential of the material is monitored against a reference electrode. The modified three-electrode system is a two-electrode system in principle, but with an inserted reference electrode, which can allow the recording of the individual electrode's potential change during the device charging or discharging.

2.3.2 Key performance characteristics

(1) Capacitance

Capacitance is a measure of quantifying the ability to store electrical charge. The calculation of capacitance C always follows the basic equation following the definition

$$C = \frac{\Delta Q}{\Delta V} \qquad \text{Equation 18}$$

where ΔQ is the change of storage charge amount, and ΔV is the change of potential (or voltage) window. Ideally, capacitance is potential-independent, indicating that ΔV is linear to ΔQ. The capacitance of the electrochemical cell can be evaluated from CV, GCD or EIS methods.

With the CV method, capacitance value can be calculated by the selection of an arbitrary segment of the CV curve. It is recommended to use the whole CV loop to obtain an average value [42]. The following two equivalent equations can be used for calculation

$$C_{s,CV} = \frac{\oint_{V_1}^{V_2} IdV}{2 \cdot v \cdot (V_2 - V_1) \cdot \Pi} \qquad \text{Equation 19}$$

$$C_{s,CV} = \frac{\oint_{0}^{2(V_2 - V_1)/v} Idt}{2 \cdot (V_2 - V_1) \cdot \Pi} \qquad \text{Equation 20}$$

where V_1 and V_2 (V) are the vertex voltages of the measured CV loop, I (A) is the response current, v (V s^{-1}) is the sweep rate, t (s) is time and Π can be mass, area or volume depending on normalization needs. The subscript "s" in $C_{s,\,CV}$ means that the capacitance is normalized thus the $C_{s,\,CV}$ has a unit of e.g. F g^{-1}, F cm$^{-3,}$ or mF cm^{-2}. Noting that conversion factors may be necessary for unit conversions. Evaluation of capacitance from CV is mostly adopted by electrochemists for small laboratory scale cells, and rarely seen for large capacitance cells because of technical difficulty in handling the huge current [43]. The more commonly used method by both academia and industry is the GCD technique. In principle, the normalized capacitance can be extracted from the linear part of the discharge curve, in terms of the equation

$$C_{s,GCD} = \frac{I}{\Pi} \cdot \frac{\Delta t}{\Delta V} \qquad \text{Equation 21}$$

where I (A) is the current for charging or discharging, Δt (s) is the time difference in relation to the voltage change ΔV (V). Similar to CV, the selection of the GCD curve segment can influence the obtained value, especially when the curve is not entirely linear. In that case, an effective capacitance value can be obtained by first calculating the stored energy during discharge, and then extract the capacitance according to the relationship between energy and capacitance for capacitors

$$C_{s,GCD} = \frac{2 \cdot E}{\Delta V^2 \cdot \Pi} = \frac{2 \cdot \int I \cdot V dt}{\Delta V^2 \cdot \Pi} \qquad \text{Equation 22}$$

where E (J) is the amount of energy being released. For both cases, if taking into account the whole discharge curve, the IR drop should be excluded from the potential range, i.e. $\Delta V = V_2 - V_1 - V_{IR}$.

It is worth noting the capacitance calculation from a two-electrode cell: If Π is the mass of two electrodes in a symmetric EC, a factor of 4 should be applied in equations 19-22 to obtain the (average) specific capacitance value of a single electrode. This is because EDL structure forms on both electrodes, therefore, the device can be represented by two capacitors connected in series.

Capacitance can also be extracted from the impedance, presenting in the form of a complex capacitance [44]

$$C = C_{Re} - jC_{Im} \qquad \text{Equation 23}$$

with

$$C_{Re} = \frac{-Z_{Im}}{2\pi f|Z|^2} \qquad \text{Equation 24}$$

$$C_{Im} = \frac{Z_{Re}}{2\pi f|Z|^2} \qquad \text{Equation 25}$$

Therefore the capacitances as a function of frequency can be obtained. A way of correlating the frequency (Hz) in the impedance measurement here with the d.c. discharge time is by $t = 1/4f$ (one period of the a.c. wave consists of 4 charge or discharge sub-periods). For example, the C_{Re} value at 0.1 Hz could roughly correspond to the capacitance at a GCD discharge time of 2.5 s.

(2) Resistance

The measurement of resistance is mostly achieved by measuring the *IR* drop at the initiation of the galvanostatic discharge. In the case of a GCD curve (Figure 9a), the resistance *R* is estimated by

$$R = \frac{\Delta V}{\Delta I} = \frac{V_{IR}}{2I} \qquad \text{Equation 26}$$

The determination of ΔV is critical for some electrochemical cells when the *V*-*t* curve does not become linear immediately at the initiation of the discharge. In this case, the estimation of *R* using the initial *IR* drop gives only a "transient-state" resistance, R_0. For practical applications, it is the "steady-state" resistance, R_{ss}, that is more relevant for calculating power densities, electrical losses, heating, etc. [43] (chap. 12). To assess the steady-state resistance, the discharge curve should be extrapolated back to $t = 0$ as shown in Figure 9b, and measure the *IR* drop to be inserted in the above equation.

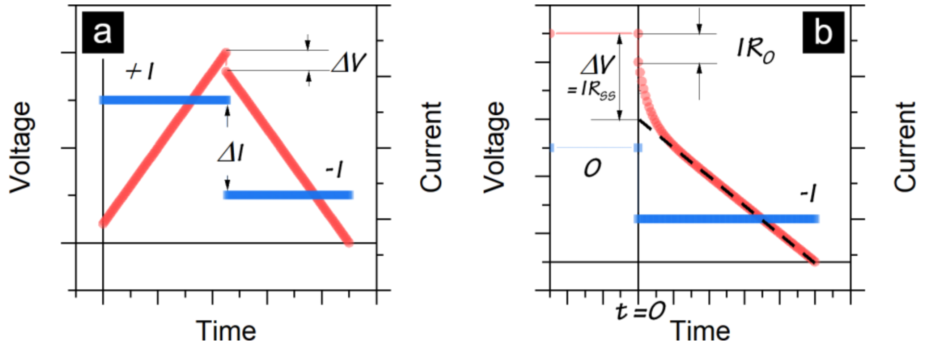

Figure 9. Resistance evaluation. (a) Calculation from a regular GCD curve; (b) Schematic showing the method for determining R_{ss}.

The a.c. impedance value at 1 kHz is common for commercial cell specifications. However, this value is always significantly lower than the d.c. resistance [45].

(3) Energy and power densities

For capacitors, the energy density E (Wh kg^{-1}) is measured by

$$E = \frac{1}{2 \times 3.6} C_s \cdot \Delta V^2 \qquad \text{Equation 27}$$

where C_s (F g^{-1}) is the normalized device capacitance, and ΔV (V) is the maximum voltage window excluding IR drop. For non-linear GCD curves, accurate quantification of E (Wh kg^{-1}) should adopt the following equation

$$E = \frac{\int I \cdot V dt}{3.6 \times \Pi} \qquad \text{Equation 28}$$

where I (A) is the current applied in GCD test, V (V) is the voltage at time t (s), and Π, in this case, should be the weight (g) of the device or at least the two electrodes.

The power density (W kg^{-1}) of a device is often calculated by

$$P_{max} = \frac{V_{max}^2}{4R \cdot \Pi} \qquad \text{Equation 29}$$

where $V_{\max}$ (V) is the maximum operating voltage, and R (ohm) is the internal resistance. $P_{\max}$ represents a maximum and probably not very useful power value. This value is reached at the load resistance equals to the internal resistance R, hence the efficiency is just 50% with the other 50% of energy is dissipated as heat. If an efficiency requirement of 95% sets in, the power can be as low as 10% of the impedance-match power as above. In literature regarding materials development, average power (W kg^{-1}) over the entire discharge curve is often applied

$$P_{avg} = \frac{3600 \times E}{t} \qquad \text{Equation 30}$$

where E (Wh kg^{-1}) is the energy density obtained through Equation 27 or 28, and t (s) is the discharge time during the GCD test.

(4) Maximum operating voltage

Qualitatively, the maximum operating voltage can be determined through a series of CV measurements with progressively increased operating voltage limits; When an abrupt current surge appears, the voltage has exceeded its maximum voltage that ensures a capacitive behavior. There is no standard quantitative measure for determining the operating voltage of an EC device, however, it is recommended [46] to define the voltage limit by fixing a threshold for the charge/discharge coulombic efficiency (e.g., 99%) [47].

(5) Cycling stability

The cycling stability is measured by repeating the GCD measurements for a number of cycles, referring to cyclic charge/discharge (CCD). Then the capacitance, efficiency as well as resistance evolution during the cycling process can be known. In combination with the impedance test, a more detailed study can be done in terms of differentiating processes with different time constants.

An alternative to the cycling test is the constant load or float test performed by holding the capacitor at the nominal cell voltage and determining the capacitance as a function of time by occasional charge/discharge cycles [48, 49].

(6) Self-discharge and leakage current

Self-discharge is a voltage loss of a charged device throughout its storage time. Evaluation can be done by recording the voltage decay of a charged device under an open circuit condition. Before the recording, the device can be held at its nominal voltage for a certain period. The leakage current is a compensating current needed to maintain the device at the rated voltage, therefore, it is normally evaluated by recording the current when holding the device at a specified voltage. Normally, it is recorded as the compensating current required to hold a fully charged device after 72 h.

(7) Working temperature range

The working temperature range influences almost all the performance characteristics, with the electrolyte playing the most critically determining role. The determination of the operational temperature range is assisted by examining performance metrics at different test temperatures. Generally, high-temperature impairs lifetime, and low-temperature significantly increases ESR and thus limits the power output.

(8) Phase angle, cut-off frequency and time constant

The phase angle quantifies the harmonic pace between voltage and current of a device under ac excitation. An ideal capacitor has a phase angle of -90°, i.e. the voltage lags behind the current by 90°. In the impedance measurement, the phase angle is defined by

$$\varphi = \arctan(\frac{Z_{Im}}{Z_{Re}}) \qquad \text{Equation 31}$$

The phase angle of capacitors will change from a value close to -90° to 0° with the increase of frequency. When the phase angle is -45 °, the capacitor component has an equal magnitude to the resistive component, and the frequency at φ = -45° is a characteristic figure-of-merit frequency, also called cut-off frequency f_0. And the time constant τ can be obtained by

$$\tau = \frac{1}{f_0} \qquad \text{Equation 32}$$

The time constant is related to modeling the capacitor with RC circuits, therefore, it is also called the *RC time constant*. For EDLC using porous carbon as the electrodes, the EDL formation in micropores is more accurately represented with the transmission line model [50], with several RC elements connected in a ladder, accounting for the transport of the ions into the EDL length or depth of the micropore. In this model, multiple time constants exist. Nonetheless, for most applications, the single time constant predicts with reasonable accuracy the response of electrochemical devices [43].

The time constant is an indicator of how fast the device can be charged and discharged, which can be conveniently inferred from the C_{im}-*f* or φ-*f* plots. Figure 10 displays the results of two distinct devices in **Paper II** and **Paper III**. By identifying the frequencies at which the peak of *C''* (i.e. C_{Im}) is reached (Figure 10a) or at which the phase angle is -45° (Figure 10b), time constants can be calculated by taking the reciprocal of the frequency values.

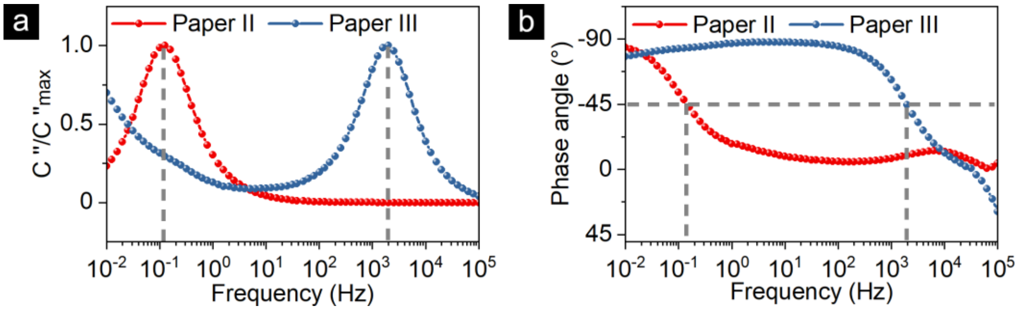

Figure 10. Determination of time constants: (a) Bode plots; (b) Phase angle plots (**Paper II and III**).

2.3.3 Inconsistencies in performance evaluation

Inconsistencies in performance evaluation can be observed in both academia and industry, making a fair comparison among various materials and devices difficult. The inconsistency is caused by multiple reasons. Researchers use different testing cell configurations, diverse techniques for electrode preparation (yielding diverse electrode mass loadings and geometries), various testing protocols, as well as different standards for calculation and normalization (and sometimes employing incorrect usage of the capacitance concept).

In recent years, guidelines and recommendations [12, 31, 34, 35, 42, 46, 51, 52] aiming to standardize performance evaluation in the research publications have been proposed. Table 5 aims to sharpen the key points from these proposed guidelines.

In industry, several international standards for performance evaluation have been compiled by national and international institutes [50]. The evaluation method is heavily dependent on application scenarios. Therefore, many standards aim for specific application fields, for example, automobile propulsion (Society of Automotive Engineers, SAE, document J3051), hybrid electric vehicles (International Electrochemical Commission, IEC, document 62576). A performance characteristic measured per one standard is not necessarily the same as the other standard aiming for a different application. The industry has established several common practices that are different from the research community. For instance, the Ragone plot is more accurately mapped by measuring a series of energy densities under constant power discharge, while the materials research papers usually calculate the energy and power density values from GCD curves at a few different current densities. In the commercial device specification sheets, it is common

Table 5. Recommendations towards standardizing performance evaluation and report

	Items	Guidelines and recommendations
General ECs	Mass loading	a. Should be reported; b. Should not be too low; 1-10 mg cm^{-2} is preferred.
	Capacitance	a. Report F g^{-1} and preferably also C g^{-1} for capacitive materials; b. Report C g^{-1} or mAh g^{-1} for battery-type materials; c. Report areal and volumetric values when it can be measured reliably; d. State the type of cells, two- or three-electrode, and mind the relationship between the device capacitance and electrode capacitance for the two-electrode cells.
	Operating voltage	a. Fix a coulombic efficiency threshold for determination; b. Investigate materials stability window with the three-electrode system first to provide information for device voltage determination.
	Energy	a. Must be derived from the two-electrode device; b. Integrating the GCD curve to calculated average energy density; c. Specify at which current density the energy density is calculated.
	Power	a. Must be derived from the two-electrode device; b. State whether it is maximum or average power; c. Specify at which current density the energy density is calculated.
	Ragone plot	a. Must be derived from the two-electrode device; b. Plot with at least 4 different current densities; c. Divide by a factor of 3-5 to extrapolate real device performance from a laboratory cell.
	Cycling stability	a. Data from the two-electrode device is more realistic; b. At least 10000 cycles for EDLCs, 5000 cycles for pseudocapacitors; c. Preferably perform both CCD and floating tests.
MSCs	Topology	State the reported MSC is an interdigitated or stacked structure.
	Class	State the reported MSC is based on thin-film, thick-film or 3D technology
	Thicknesses	a. State the thicknesses of the substrate, current collectors, electrodes; b. If proposing a solid-state device, the thickness of the electrolyte should also be stated; c. State the possibility (or not) to scale up the electrode thickness.
	Areas	a. State the geometry area of each electrode, and the device b. Enable the calculation of the gap area for interdigitated MSCs
	Normalization	a. Normalize capacitance, energy and power to both electrode and device geometry area, to report in mF cm^{-2}, μWh cm^{-2}, mW cm^{-2}. b. Further normalize to the electrode thickness, report in mF cm^{-2} μm^{-1}, μWh cm^{-2} μm^{-1}, mW cm^{-2} μm^{-1}.

to find that the power density measurements are performed according to the IEC 62391-2 standard. This standard defines a parameter named usable power density, calculated by

$$P = \frac{0.12V_{max}^2}{R_{SS} \cdot m} \qquad \text{Equation 33}$$

where m is the weight of the device. This value is the average power between 80% V_{max} and 40% V_{max} under constant current I that causes a 20% V_{max} IR drop. This type of calculation is rarely seen in academia.

2.3.4 Specialties in evaluating ECs for miniaturized self-powered systems applications

For emerging applications of ECs for miniaturized self-powered systems, compiling an evaluation protocol according to its special circumstances would be very valuable. With a few to mention, the self-discharge and leakage current issues are critical for this field. Evaluation of these two features in the industry usually specified a period of 72 hours to extract self-discharge rate or leakage current. To guarantee the quality of service of the autonomous systems, the storage EC is required to be active more often, indicating that a self-discharge rate or leakage current after 72 hours hold or open circuit is not very relevant. Therefore, the new evaluation standard may preferably specify minutes or even seconds.

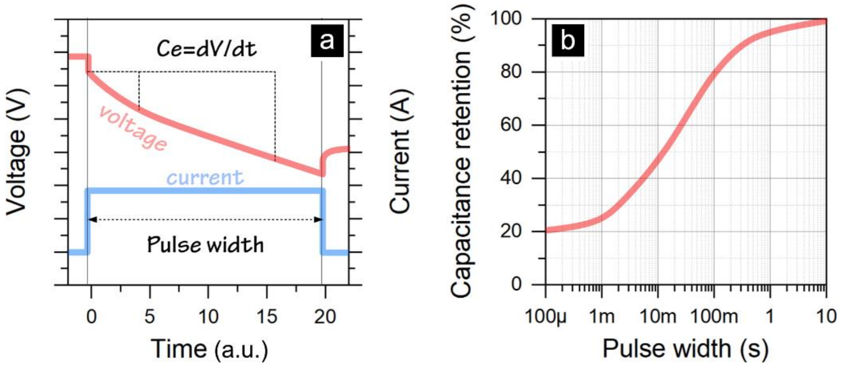

Figure 11. Schematics of evaluating the performance under pulse discharge. (a) The voltage and current curves under a pulse condition; (b) Effective capacitance as a function of the pulse width.

Another specialty concerning self-powered system application is the pulse charge or discharge on the scale of milliseconds. To efficiently handle the pulses, the device must respond quickly. More specifically, the transition period from initial resistance to steady-state resistance should be minimized so that the discharge curve is as linear as possible. It is generally accepted that differentiating initial resistance R_0 and steady-state R_{ss} is only important for large ECs, which could be a reason why the materials research publications rarely care about the shape of the initial section of the discharge curve. To quantify the performance at pulse conditions, the effective capacitance C_e as a function of pulse width can be calculated, as shown in Figure 11. The effective capacitance value will approach the d.c. capacitance (Equation 21) at a larger pulse width. Analytical modeling of EDLCs indicates that the initial transition part of the discharge curve is related to the electrode porosity, and the transition to linearity can finish after a few RC time constants [45, 53]. From the view of the equivalent circuit, the R-R//C circuit may oversimplify the real picture, but it is certain that reducing the circuit to a simple series R-C circuit as in Figure 7, i.e. decreasing the resistance and eventually eliminating all the parallel R//C links and circuit components from the transmission line effect or charge transfer processes, will be helpful.

Also, in miniaturized self-powered systems, the current obtainable from the miniature harvester imply that the current for charging the ECs would be small, down to mA or even µA magnitude. In this case, it is important that the EC can be charged in a capacitive manner, i.e. linear charging curve under extremely low current. This seems to be opposite to the intuition that ECs are supposed to work at high current for conventional applications. The performance in this regard is in principle related to leakage current, however, separate testing may be necessary when it comes to benchmarking performance for these applications.

2.4 Components

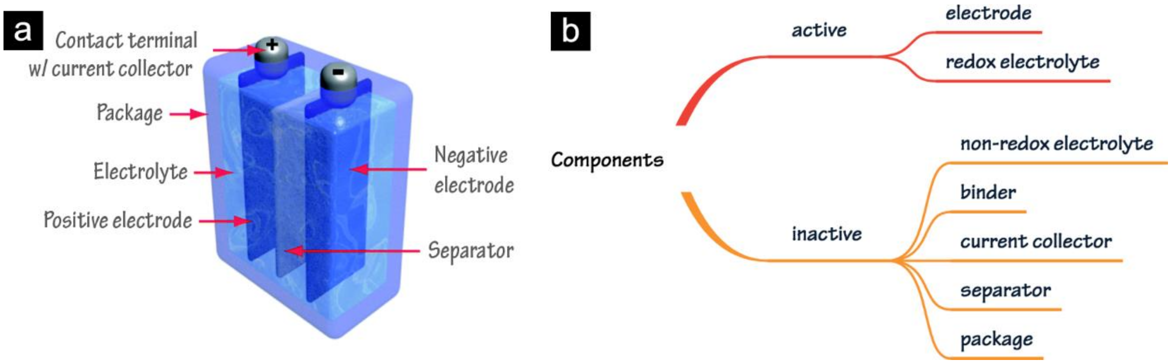

Figure 12. (a) Device schematics [54] and (b) the components. (figure a is reproduced with permission from RSC)

Figure 12 depicts the basic structure of a complete EC device. The components for constructing ECs can be divided into two groups, the active components which contribute directly to energy storage, and inactive components of which the function is to facilitate the energy storage. The active components include electrodes, and electrolytes when they are redox-active; The passive components are mainly the non-redox electrolytes, binders, separators, current collectors and packaging materials. The intensive research efforts in the community have contributed to a great plethora of materials options for each. This section aims to sketch the outline of materials options for each category.

2.4.1 Electrodes

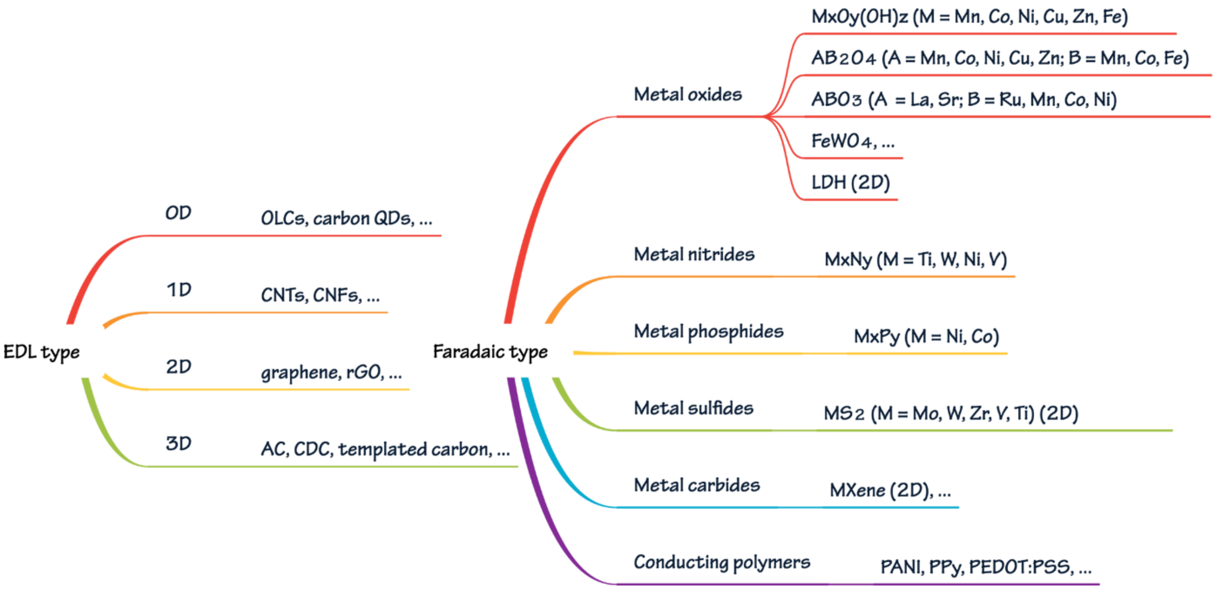

Figure 13. Electrode materials classification.

Electrodes define the storage mechanism and kinetics. Carbon materials are the classic EDL materials - approximately 80% of the commercially available supercapacitors are made of nanostructured carbonaceous materials [55]. Nearly all carbon allotropes are effective in energy storage, including 0D structured onion-like carbon (OLC), 1D carbon nanotubes (CNTs), 2D graphene and 3D activated carbon (AC), carbide-derived carbon (CDC) and templated carbon. As for the Faradaic type materials, it covers metal oxides [30, 56], nitrides [57], sulfides [58], phosphides [59], and conducting polymers [60]. Not all these Faradaic materials are pseudocapacitive, however, they can be coupled with a suitable counter electrode to construct hybrid devices displaying capacitive features. In recent years, emerging 2D materials [61] such as MXene (transition metal carbides and nitrides) [62], layered double hydroxide (LDHs) [63], transition metal dichalcogenides (TMDs) [64] e.g. MoS_2 [65] are proven promising for electrochemical energy storage due to their abundant active surfaces and open ion diffusion channels. Besides, metal-organic-framework (MOF) [66, 67] and covalent organic framework (COF) [68] materials provide a mean to regulate the porosity of metal oxides and carbon have received significant attention in the community.

2.4.2 Electrolytes

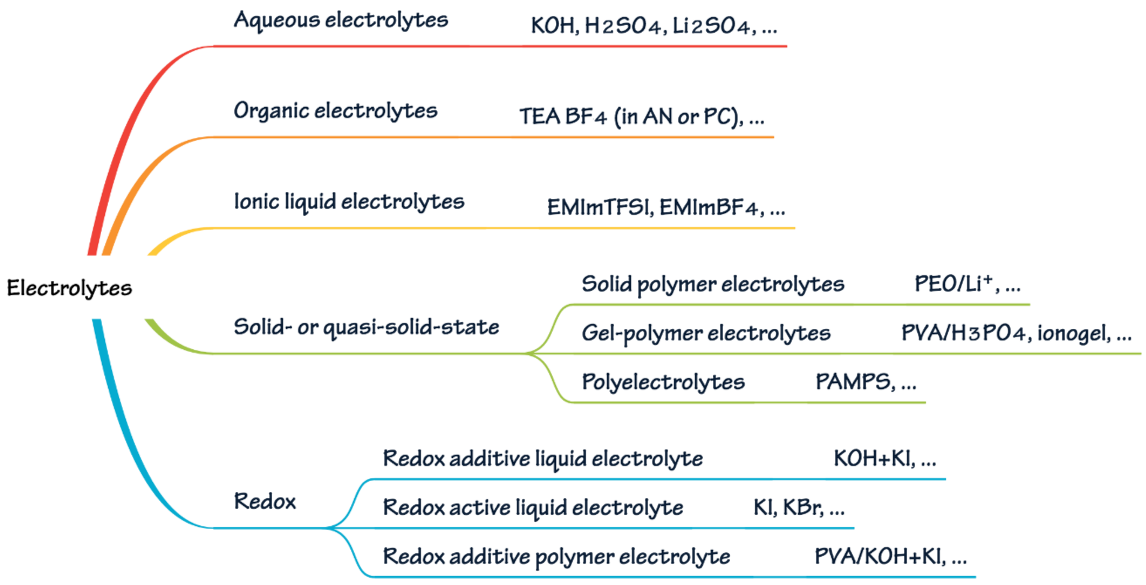

Figure 14. Electrolyte classification.

Electrolytes play a determining role in the operating voltage window, working temperature range and the resistance. The widely used electrolytes are aqueous, organic, ionic liquid electrolytes, and solid or quasi-solid-state electrolytes, as classified in Figure 14.

Polyvinyl alcohol (PVA) based gel electrolytes are also called *hydrogel* polymer electrolytes characterized by 3D polymeric networks trapping H_2O in the PVA matrix mainly through surface tension [69]. The ions move via the solvent H_2O and show good conductivity, but the mechanical strength and operating temperature and voltage are relatively low. Instead of H_2O, gel polymer electrolytes (GPEs) can also be based on organic solvents - "*organogel*" electrolytes. Corresponding polymer matrix options are polyethylene oxide (PEO) [70, 71], poly(methyl methacrylate) (PMMA) [72, 73], polyvinylpyrrolidone (PVP), polyether ether ketone (PEEK) [74] and copolymers [75, 76]. Organogel GPEs have an extended maximum operating voltage up to 3 V [71] compared to hydrogel GPEs. Confining ionic liquids within a silica-like network forms ionogels [16, 77, 78], which can exhibit larger voltage and temperature windows. A general comparison of various types of electrolytes is displayed in Table 6.

Table 6. Typical metric values of liquid and solid- or quasi-solid-state electrolytes

	liquid electrolytes			solid- or quasi-solid-state electrolytes		
	aqueous	organic	IL	hydrogel	organogel	ionogel
V_{max} (V)	0.8-1.6	2.5-2.8	1-4	0.8-1.6	2.5-2.8	1-4
ionic conductivity @RT (S cm^{-1})	up to 1	0.05	10^{-3} -10^{-2}	10^{-3}-10^{-1}	10^{-3}	10^{-3}
temperature range (°C)	-10 -70	-40-70	RT-100+	-10-70	-40-70	RT-100+

Conventionally, an electrolyte is electrochemically inactive, while a redox electrolyte which contributes Faradaic type of energy storage has aroused broad attention recently [79, 80]. Different from the conventional ones, redox electrolytes contain redox-active species such as simple or complexes of transition metal ions (e.g. VO^{2+}), halide ions (e.g. I^-, Br^-), quinones and phenylamide. Redox electrolytes can be classified as *redox-additive electrolytes*, *redox-active electrolytes* and *redox-additive polymer electrolytes*. The first type refers to conventional electrolytes with redox-active species as an additive, while the second refers to those that are inherently able to undergo fast redox reactions, such as KBr (**Paper I**), and the third type refers to redox-active species as an additive in polymer-based electrolytes.

During a charging process on the positive electrode side as shown in Figure 15a, oxidizable species (R_P) from a redox electrolyte donate electrons and are oxidized to O_P, and on the negative side, reducible species O_N accept electrons to be reduced to R_N. A reversible process happens during a discharging process as in Figure 15b. The electrolyte that contributes R_P is called *catholyte*, and the one that provides O_N is called *anolyte*. Note that a redox electrolyte can contain either one of R_P and O_N, or both species. For example, KBr redox electrolyte (**Paper I**) contains only R_P, i.e. bromine ions to be oxidized to O_P (Br_3^-), while potassium ions in KBr are just normal cations to be adsorbed on the surface but undergo no redox reactions.

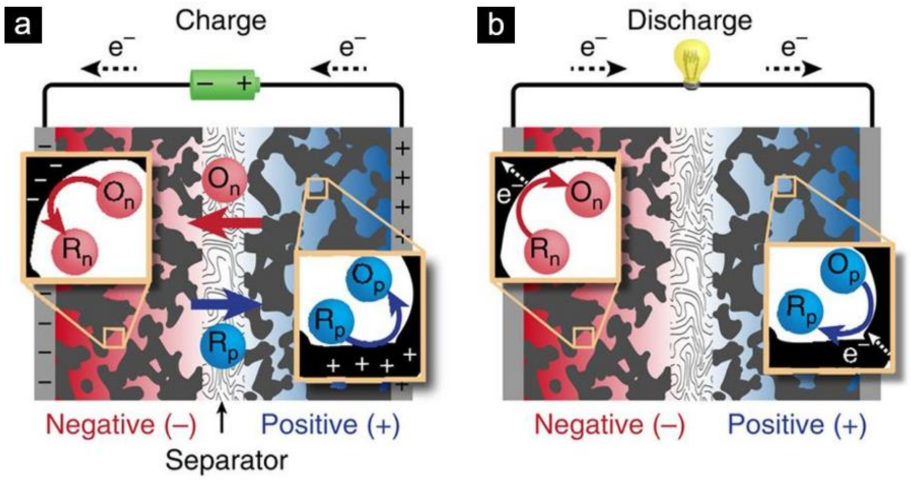

Figure 15. Schematic of redox processes during (a) charging and (b) discharging [81]. (Reproduced with permission from Springer Nature)

2.4.3 Binders

Binders are needed in cases where the electrode materials are in the form of powders in its pristine state so that the electrode can be kept as an intact film that can be practically used in devices. Binders should improve the cohesion between electrode particles, also ensure a strong adhesion to current collectors. The addition of binders can alter the porosity of the active electrode materials [82]. The main materials options for binders are poly(vinylidene fluoride) (PVDF), polytetrafluoroethylene (PTFE), Nafion, natural cellulose, PVP, polyacrylic acid (PAA) and conductive polymers (polypyrrole, polyaniline, etc.) [83].

2.4.4 Separators

The function of separators is to prevent direct contact between positive and negative electrodes and at the same time allow for fast transportation of ionic charge carriers. As part of the "dead" weight and volume of ECs, separators are preferred to be light and thin but should also exhibit certain mechanical strength, thermal and chemical stabilities, and be easily wetted by the electrolyte. Commonly used separators are thin porous polymers (polypropylene PP and polyethylene PE), cellulose and glass fibers. Recently developed options include graphene oxide (GO) films [84] and eggshell membranes [85]. Some of them have different preferences for the type of electrolytes. For example, cellulose separators work well in organic electrolytes but may degrade in aqueous H_2SO_4 electrolytes [86].

The thermal properties of separators are important when designing high-temperature devices. Thermal shrinkage of the separators happens around their decomposition temperature, leading to short circuits between the two electrodes, which may eventually cause thermal runaway (the shrinkage of separators is required to be less than 5 % after 60 min at 90 °C [87]). At low temperatures when ion mobility is limited, the porosity of the separator plays a vital role in the device's overall performance [88, 89].

2.4.5 Current collectors and packaging

Current collectors are typically flat metal foils or grids onto which active electrode materials are cast [90]. They should be chemically and electrochemically stable in the presence of an electrolyte and during device operation. For aqueous acid electrolytes, current collectors should be corrosion-resistant. Noble metals such as gold are an ideal option in terms of stability, but the high cost limits their widespread use. Alternative options are indium tin oxide (ITO) [91], carbon [92] and conducting polymers [92]. For aqueous alkaline electrolytes, common collectors are nickel [93], stainless steel [94] and also carbon-based materials such as carbon fabrics [95], carbon nanotubes [96], carbon fiber papers [97] and graphite [98]. Aqueous neutral electrolytes are much less corrosive, therefore the materials for acid and alkaline electrolytes are also applicable to them. For organic and ionic liquid electrolytes, aluminum is the most common current collector material.

The choice of current collectors influences both device lifetime and resistance. It has been found that an aluminum current collector is involved in the aging of ECs based on organic electrolytes [86] and ionic liquids [99, 100]. An optimal interface between a current collector and an electrode material reduces the internal resistance. Surface treatments of a sol-gel deposit of conducting carbonaceous material on aluminum current collectors have been shown to decrease ohmic drops at the interface [101]. Developing nanostructured current collectors with an increased contact area is a direction towards high-performance devices. The beneficial effect is particularly significant for pseudocapacitive material based ECs. This is because pseudocapacitive materials mostly have low electronic and ionic conductivities, therefore ion access is limited when the material is deposited on planar current collectors in a thick film. With nanostructured current collectors such as a carbon nanotube array, pseudocapacitive materials can be deposited onto it in a conformal way, and the exposed area to the electrolyte is greatly improved [102]. The electrode material in Paper III can be used as 3D current collectors for this purpose.

Packaging materials of ECs depend on the cell configuration and manufacturers. In general, steel is used for coin cells (e.g. stainless steel SS316), cylindrical cells (nickel-plated steel sheets [103]) and prismatic cells (heavy gauge steel [104]). Pouch cells use aluminum laminated film [105] for the casing, from outside to inside, the laminated film consists of a polyamide layer, aluminum foil, and polypropylene with adhesive layers in between. Some suppliers e.g. Cellergy offer prismatic ECs with polymer-based packages.

CHAPTER 3

Device performance challenges

This chapter elaborates on the strategies and methods aiming to address the challenging issues regarding device performance, identified in Chapter 1. Many of the performance-related issues are not only specific to miniaturized systems but also exist for ECs' application in large scale systems, therefore the corresponding strategies and methods can be universal.

3.1 Towards high energy densities with high power and cycling stability

The energy density of an electrochemical energy storage device is determined both by the capacity and the operating voltage. For ECs, the relationship of $E \propto CV^2$ indicated the two strategies for improving energy density, i.e. increase the capacitance and/or improve the maximum operating voltage. The specific solutions can be generalized to material-, electrode- and device-level optimizations. At material-level, electrode materials are improved towards higher capacitance or capacity and greater stability; at electrode-level, novel structural design of thick electrodes, additive-free or current collector-free electrodes can reduce the fraction of inactive components for high overall device energy density; at device-level, the two electrodes cooperate to utilize their working potential range to the full extent, and a bipolar design further decreases the inactive component fraction for an energy density boost.

3.1.1 Material-level optimization

(1) Carbon-based materials

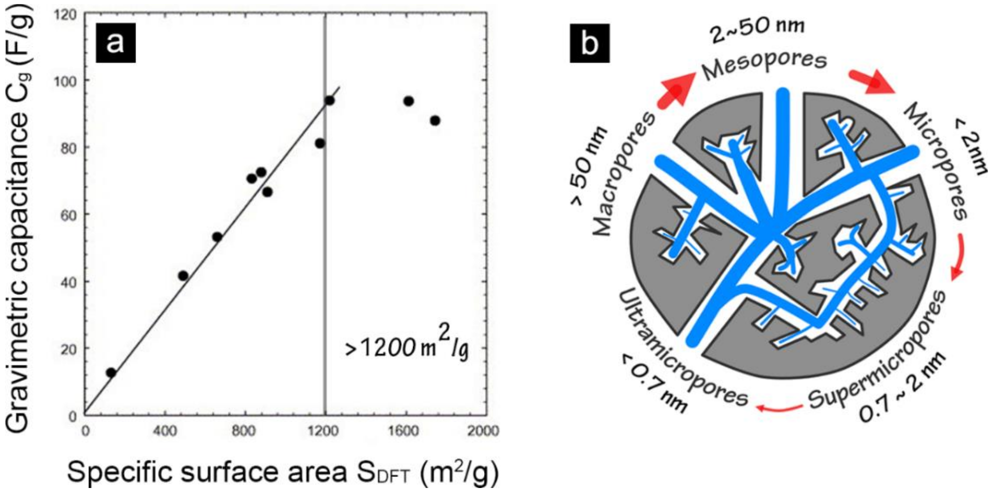

Figure 16. Correlating capacitance and specific surface area, porosity. (a) Gravimetric capacitance vs. specific surface area [106] (Permission from Elsevier); (b) Schematics of a hierarchical porous structure.

Carbon materials often constitute electrodes in EDLCs, relying on ion adsorption on their surface. Therefore, maximizing the specific surface area (SSA) of carbon is effective to improve the capacitance and hence the energy density. The key to ensuring a capacitance increase with surface area is to match the size of the pores to the size of the ions to be adsorbed. Research has found that the linear increase of specific capacitance as a function of SSA seams to cease at SSA $\cong$ 1200 m^2 g^{-1} [106, 107], as shown in Figure 16a. This is because of a mismatch between pore size and ion size. Optimal capacitance is achievable when the pore size is very close to the size of de-solvated ions, implying that solvated ions could undergo a de-solvation process before entering the pore to be electro-adsorbed. This was supported by several experimental and theoretical research [24, 108-119]. Micropores that are smaller than the ions contribute substantially to SSA but little to charge storage due to ion sieving effect [109], while very large pores show worse interaction with ions [115]. Therefore, carbon with both high SSA and relatively narrow pore size distribution (PSD) is preferred to maximize the capacitance. The understanding of capacitance origin has benefited the development of carbon-based ECs. Capacitive performance of activated carbon has been greatly improved from about 120 F g^{-1} in the mid-2000s to more than 200 F g^{-1} in organic electrolytes [120].

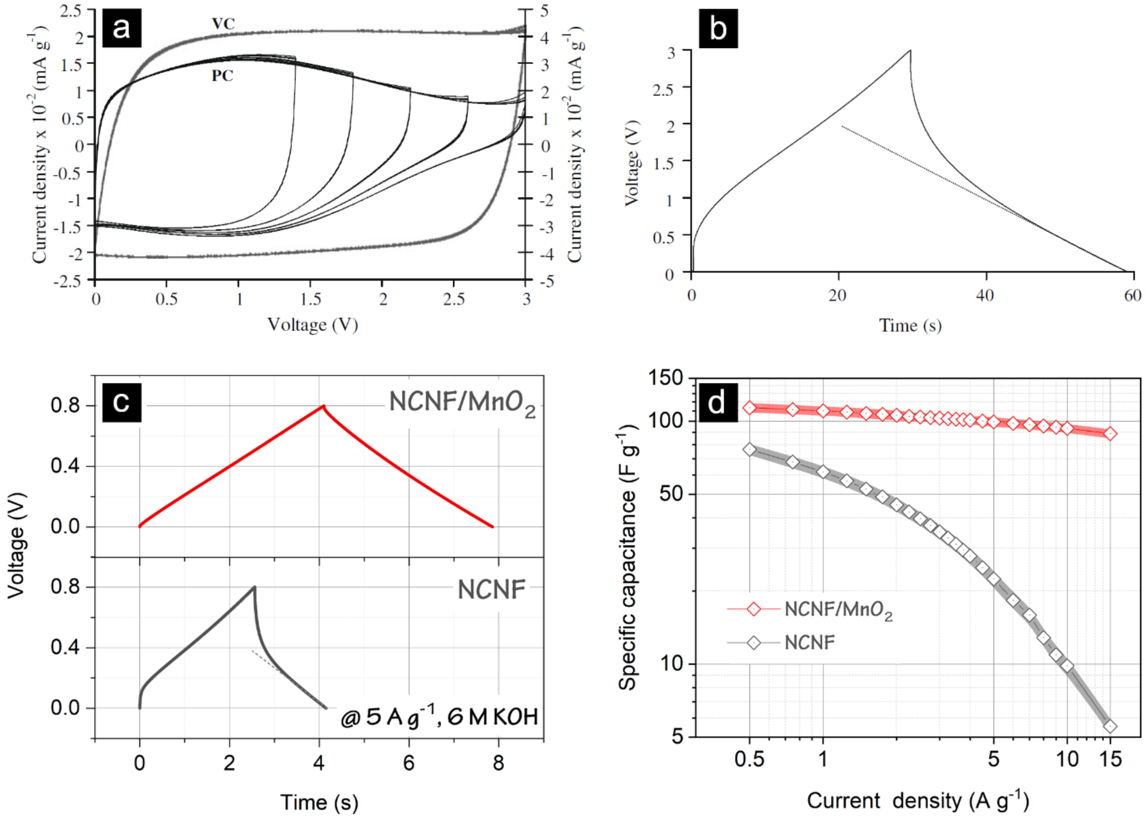

Figure 17. Pore starvation effect. (a) Comparison of VC (viscose-based carbon) and PC (pitch-derived carbon) with PC showing pore starvation effect [121]; (b) GCD curve of PC [121]; (c-d) Comparison of NCNF/MnO$_2$ and NCNF electrodes (**Paper VI**). (Reproduced with permission from Elsevier)

When the accessible SSA is significantly low, a “pore starvation” effect, i.e. porosity saturation within the voltage window, can set in. Figure 17a-b displays the CV curves of a carbon material PC of which the available SSA is fully occupied at a voltage significantly smaller than the maximum voltage 3 V. The effect results in the electrochemical signature as on the CV curves, the capacitive current diminishes when the charging process goes beyond a certain voltage because few ions can be absorbed when reaching the full available SSA coverage. The corresponding GCD curves exhibit features as being concave to the *x*-axis. This type of electrochemical response limits the usable voltage and consequently the energy and power deliverable by an EC.

Paper VI discusses the pore starvation effect between a cellulose-derived nitrogen-doped carbon nanofiber (NCNF), and a composite of NCNF and MnO_2 (NCNF/MnO_2). It was speculated that the MnO_2 component in the NCNF/MnO_2 is mostly inactive because of non-intimate contact between MnO_2 and the NCNF. Therefore, the apparent performance of NCNF/MnO_2 is mostly the NCNF carbon matrix but with more developed porosity and surface area than the pristine NCNF. The GCD curves of the two materials are shown in Figure 17c-d. The NCNF shows the starvation features described above, while its counterpart remains capacitive throughout the whole voltage range. The saturation voltage, at which the available SSA is fully occupied, is proportional to the SSA according to the following consideration.

Before reaching the saturation voltage V_{sat}, the capacitance C_{sat} can be defined as

$$C_{sat} = \frac{Q_{sat}}{V_{sat}} \qquad \text{Equation 34}$$

where Q_{sat} is the maximum charge accumulated up to full surface saturation. In principle, capacitance would decrease once the voltage is beyond V_{sat} because of no available surface area for ion adsorption, i.e. $\Delta Q_{sat} \sim 0$. Assume that the capacitance for a specific material, i.e. the slope of GCD curves, is constant before full coverage of the surface area, the saturation voltage can be expressed as

$$V_{sat} = \frac{Q_{sat}}{C_{sat}} \qquad \text{Equation 35}$$

Moreover, consider

$$Q_{sat} \propto \frac{S_a}{S_{ion}} \qquad \text{Equation 36}$$

it can thus be obtained that the saturation voltage is proportional to the accessible surface area S_a of the electrode, and inversely proportional to C_{sat} and the exterior surface area of electrolyte ions S_{ion} (related to the radius of the ion):

$$V_{sat} \propto \frac{S_a}{S_{ion} \times C_{sat}} \qquad \text{Equation 37}$$

Therefore, increasing the SSA or decreasing the electrolyte ion size should increase the saturation voltage. C_{sat} can be estimated from the linear segment of the GCD curves, and may be relatively constant in a specific system.

A hierarchical porous structure, as shown in Figure 16b, with a combination of micropores, mesopores, and macropores benefits the electrochemical performance the most. The ions initially enter the largest pores and subsequently flow into smaller ones, and finally reach the smallest pores. An optimal network overcomes the drawback of slow mass transportation within micropore-dominated carbon materials, achieving both high capacitance and high rate capability. The beneficial interplay between different pores presents a new benchmark of carbon electrode capacitance beyond 300 F g^{-1} [54].

Besides SSA and porosity, the surface chemistry of carbon is an important factor that influences the performance in specific capacitance, rate capability, and cycling stability. On the one hand, a certain range of surface functional groups and heteroatoms doping may contribute to so-call pseudocapacitance, modulate the electron donor/acceptor concentration and can thus improve the electronic conductivity; by combining the effects both from hierarchical porosity of template carbon and nitrogen doping, a record value of 855 F g^{-1} (at 1 A g^{-1}) has been reported for a few-layer nitrogen-doped (source of pseudocapacitance) mesoporous carbon fabricated from a silica hard template, and an electrode capacitance of 615 F g^{-1} is still retained at 40 A g^{-1} [122]. On the other hand, the incorporation of the chemical compositions may complex the aging mechanism and decrease the maximum working voltage range. It has been suggested that oxygen-containing groups can lead to more side reactions and gas evolution at high polarization voltage [123]. Removing oxygen-containing functional groups was demonstrated to increase the maximum working voltage [124, 125].

(2) Pseudocapacitive materials

Pseudocapacitive materials can store much more charge than pure EDL materials. The theoretical specific capacitance for MnO_2 reaches 1388 F g^{-1} and for RuO_2, 1400 to 2000 F g^{-1} [126-128] depending on the degree of reaction and the potential window within which the reaction is assumed to be completed. Nevertheless, such a high capacitance was rarely achieved in practice [129]. The low electronic conductivity (of amorphous RuO_2) is an important reason for the limitation, which results in poor charge carrier transport and weak interaction between nanoparticles. An intrinsically low electronic conductivity that leads to low capacitance and inferior power capability is a challenge to almost all other transition metal oxide pseudocapacitive materials.

One of the solutions to this problem is to engineer the material into a thin film. The performance of transition metal oxides can thus be greatly improved because the charge carrier transport path is minimized and the interplay between particles is no longer an issue [130]. As a result, the effect of low conductivity is minimized. However, the thin film strategy limits the overall capacity of charge storage, giving low areal capacitance and is suitable only for niche applications. Alternatively, using nanostructured 3D current collectors as a substrate for depositing a conformal layer of materials can be an effective approach to increasing mass loading while still benefiting from the fast dynamics of thin-film electrodes.

Compositing the poorly conductive metal oxide with a relatively high conductivity material, e.g. carbon, seems to be a more prevailing strategy to combat the abovementioned problem. In the configuration of carbon/metal oxide composite, the carbon backbone acts as a highly conductive medium to the current collector, the through-connected porosity serves as a continuous pathway for electrolyte transport, and the nanoscopic MnO_2 phase maximizes the surface-to-volume area to enhance pseudocapacitance originating from the surface. The reported carbon substrates include all sorts of carbon materials for EDLCs: activated carbon [131], carbon nanotubes[132, 133], graphene [134, 135], reduced graphene oxides [136, 137], carbon black [138, 139], carbon nanofibers [131], microporous carbon [140, 141] and so forth. Overall, the incorporation of MnO_2 substantially increases the capacitance compared to the carbon matrix, manifesting the effectiveness of the electrode design. For example, onion-like carbon (OLC) with embedded MnO_2 has more than 21 times higher specific capacitance than a pure OLC device (254 vs. 12 F g^{-1}) [142]. Previous research [143] (Figure 18) proves that intimate contact between MnO_2 and the carbon matrix is favorable for exerting the pseudocapacitance, and accordingly grafting of the oxide to the carbon surface has been demonstrated [137, 143].

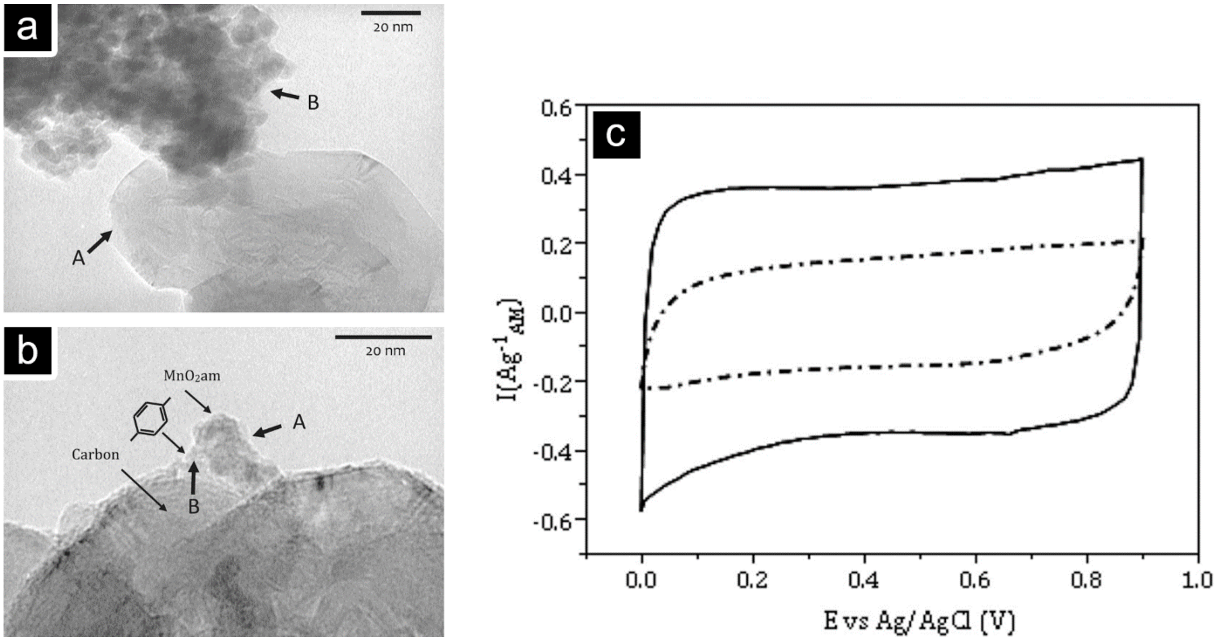

Figure 18. Intimate contact between MnO_2 and carbon facilitates the MnO_2 pseudocapacitance. (a) SEM image showing a simple mixture of MnO_2 and carbon (arrow A - unmodified carbon black, arrow B - amorphous MnO_2; (b) SEM image showing MnO_2 grafted to carbon particles (arrow A - MnO_2 particle, arrow B - an organic layer linking a MnO_2 grain and a carbon black particle); (c) Comparison of CV curves for the simple mixture (dash) and the grafted carbon/MnO_2 (solid) [143]. (Reproduced with permission from IOP)

It is interesting to point out that the compositing chemistry could significantly alter the property of the carbon substrate, therefore the overall performance of the composite material can be largely influenced by the carbon. **Paper VI** presents the composite between NCNF and MnO_2

through the reaction between $KMnO_4$ and carbon under a hydrothermal condition. The reaction conditions lead to the concentration of MnO_2 needles on the exterior surface of NCNF, therefore, it is a non-intimate contact mode of MnO_2 and carbon, as shown in Figure 19a-b. After removing the MnO_2 from NCNF/MnO_2 (sample w-NCNF/MnO_2), the specific capacitance is even higher than that of the NCNF/MnO_2 (Figure 19c), inferring that the electrode performance is mostly the response from the carbon NCNF, while the MnO_2 is inactive. The MnO_2 component could easily detach from the NCNF surface when in contact with the electrolyte, and removed with physical methods e.g. wiping the surface or mild sonication - the NCNF/MnO_2 becomes a unique sample to study how the carbon property is changed through the compositing chemical process. It is found that SSA, porosity as well as surface functional groups composition of NCNF has been improved for higher energy and power densities.

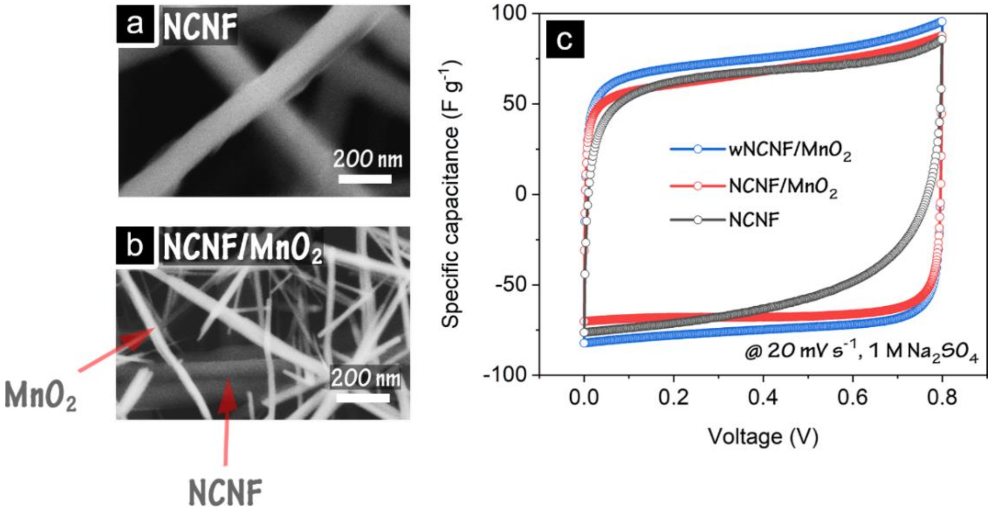

Figure 19. The non-intimate contact between NCNF and MnO_2. (a) SEM image of bare NCNF; (b) SEM image of NCNF/MnO_2 composite; (c) CV curves of NCNF, NCNF/MnO_2 and w-NCNF/MnO_2 (**Paper VI**). (Reproduced with permission from Elsevier)

The other solution to improve conductivity is through the modulation of the materials' composition and electronic structure. Introducing oxygen vacancies, as impurity states in the bandgap, into oxides to tune their intrinsic defects is one way to increase the conductivity of transition metal oxides [144]. The vacancies also serve as active sites for reactions. Oxygen vacancies can be obtained through annealing under vacuum or with a reducing gas (e.g. hydrogen, ammonia) [145]. Another approach for improving conductivity is through doping, via the regulation of donor or acceptor densities. Both non-metal [146] and metal [147] atoms have been demonstrated as dopants to optimize the capacitive performance. The modified materials show improved maximum capacitances, lower resistance and increased power densities.

Compared to oxides, transition metal sulfides, nitrides, and carbides have higher electronic conductivity with rich redox chemistry for energy storage [148-150]. Especially for carbide Ti_3C_2 which exhibits a metallic conductivity of up to 1 500 S cm^{-1}, and an extremely high volumetric capacitance of 900 F cm^{-3} (correspond to 245 F g^{-1}) [151]. Ti_3C_2 is a member of the MXene family which is a new direction of electrode materials for constructing high-performance ECs. Excellent charge storage performance of MXene is partly because of their 2D structures, representative of a large group of 2D and layered structured materials [148, 149]. These materials are only a few atoms thick and therefore have a large number of immediately accessible electrochemically active sites. On the other hand, the rich active sites lead to the instability of such materials, which is also a common problem to pseudocapacitive materials. The remedy could be engineering specific microstructure to tolerate the volume expansion and thus reduce the strain during the charging/discharging processes.

3.1.2 Electrode-level optimization

The energy of a device comes from its active components, electrodes in most cases. Therefore, increasing the weight fraction or volume fraction of the electrodes, i.e. reducing the fraction of current collectors, packages, etc. can boost the overall energy density of the device. For miniature systems, usually, the area or volume is the most critical criteria.

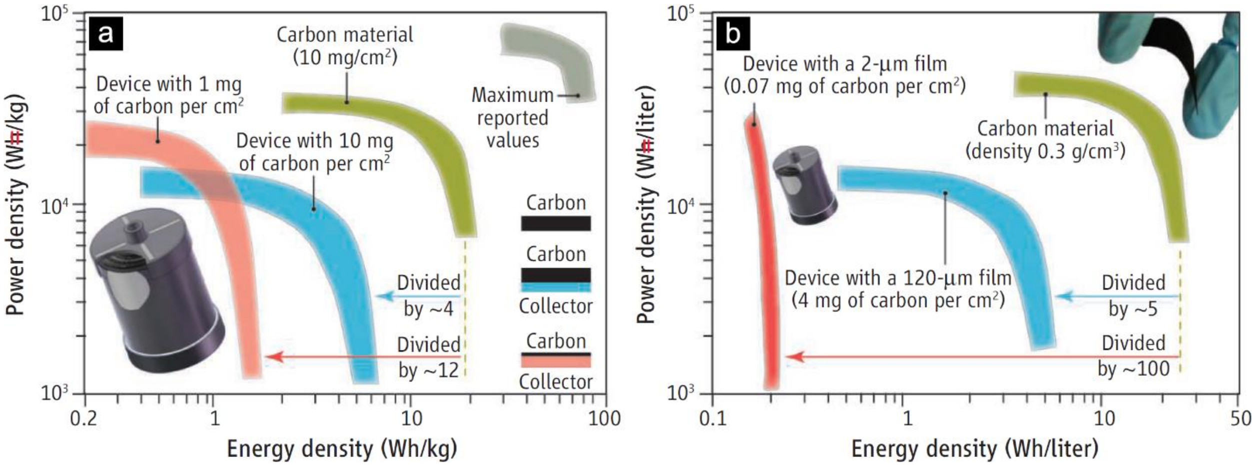

Figure 20. Interpretation of Ragone plots concerning the (a) mass loading and (b) thickness [51]. (Reproduced with permission from AAAS)

With a thin coating layer, gravimetric energy density can achieve a substantially higher value, however, it is usually a meaningless number. The Ragone plots in Figure 20 show that excellent properties of carbon materials will not translate to medium- and large-scale devices if thin-film and/or low-density electrodes are used [51]. With the increase of the coating layer thickness, the fraction of active materials would be higher than a thinner coating. However, the practical utilization of thick coating must overcome the problem of impaired power density due to prolonged charge transport distance and resistance (Figure 21a-b). An advanced thick electrode should overcome the barrier to gain high energy density and power density at the same time (Figure 21c). Also, enhancing the mechanical property and avoiding the fracture and delamination of the thick coating layer during the drying process is critical. Commercial AC electrodes are in a mass loading level of ca. 10 mg cm^{-2}, and thickness up to 200 µm. For MSCs, a threshold of 5 µm coating layer thickness is proposed to distinguish thin-film and thick-film technology-based MSCs [12].

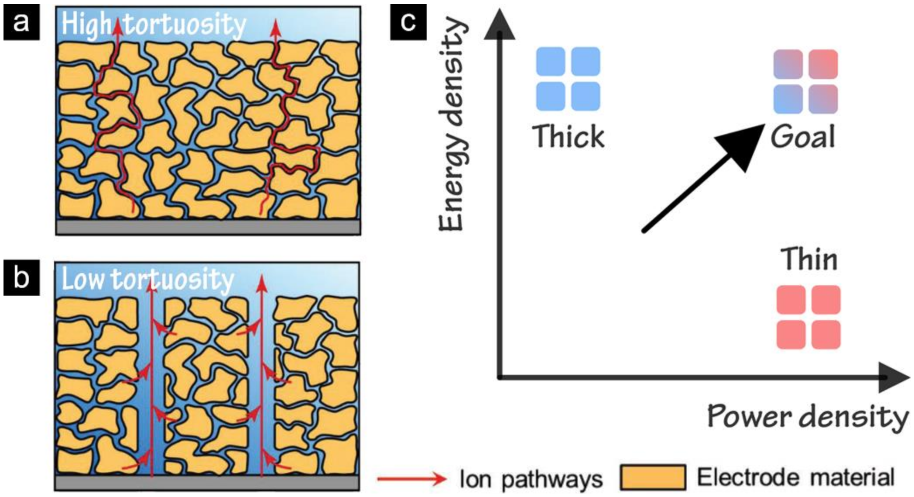

Figure 21. Schematics of thick electrodes with different pathways for ion transport, and the trade-off between energy and power. (a) A conventional thick electrode with high tortuosity [152]; (b) An advanced thick electrode with low tortuosity [152]; (c) The goal of the thick electrode approach. (a-b are reproduced with permission from Wiley)

To promote the power density of thick electrodes, the electrode should be designed for low tortuosity (Figure 21b) according to the effective ionic conductivity expression

$$\sigma_{eff} = \frac{\varepsilon}{\tau}\sigma \qquad \text{Equation 38}$$

where ε is the porosity (formed by the negative space of the solid particles), τ is the tortuosity and σ is the intrinsic ionic conductivity of the electrolyte. Although a high porosity increases the conductivity, the additional electrolyte uptake for a high porosity electrode may diminish the energy density boost by a thick electrode approach.

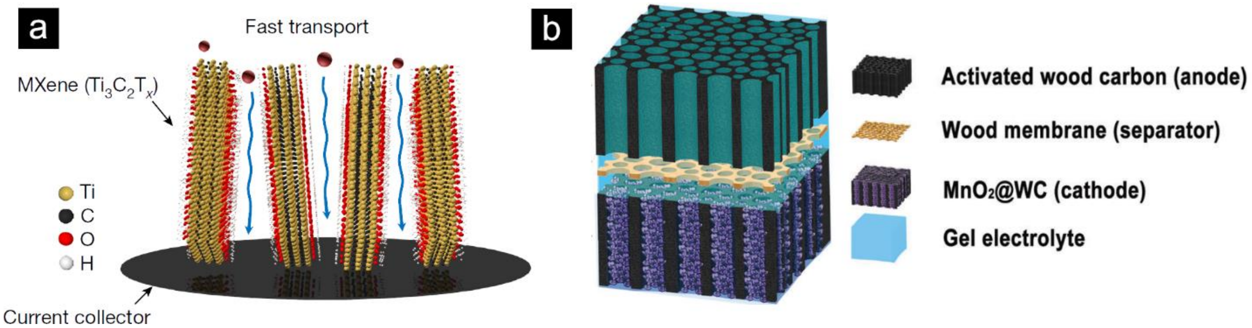

Figure 22. Low tortuosity thick electrodes. (a) Orienting liquid crystal phase MXene [153]; (b) Utilizing the channels in wood chips [154]. (Reproduced with permission from Springer Nature and RSC)

Orientating the electrode materials to form an anisotropic structure is a way to achieve a low tortuosity. The liquid crystal phase formed by an MXene material $Ti_3C_2T_x$ achieved the anisotropic structure. The resulting electrode films show excellent performance that is nearly independent of film thickness up to 200 μm, which makes them highly attractive for energy storage applications (Figure 22a) [153]. Taking advantage of the uni-directional structure of wood, thick electrodes up to 1 mm were fabricated and an AC//MnO$_2$ asymmetric device was demonstrated with an areal capacitance of 3.6 F cm^{-2} and volumetric capacitance of 14.4 F cm^{-3} (Figure 22b) [154].

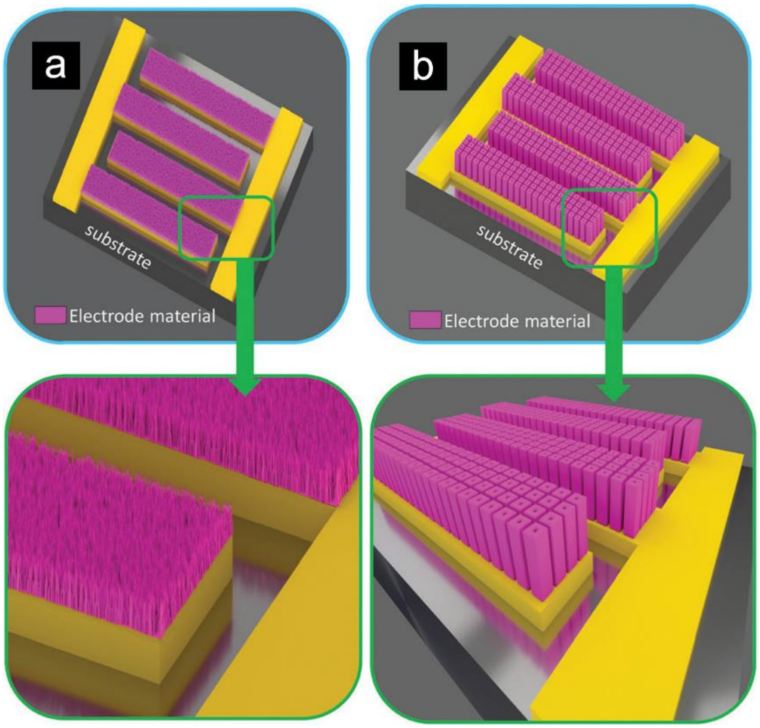

Figure 23. Thick-film technology for 3D MSCs. (a) Conformal coating of electrode materials on nano-structured scaffold (golden layers) [12]; (b) Coating materials on micro-structured scaffold [12]. (Reproduced with permission from RSC)

Except for the ionic conductivity, electronic conductivity is also a key for thick electrodes. A high conductivity network can be achieved by nanostructured 3D current collectors. This strategy proves effective in MSCs, where the active material is conformally coated on nanopillars (layer thickness limited to the spacing, typically less than 50 nm), or more preferably micro-tubes to achieve a higher coating layer thickness (Figure 23) [12]. The 3D current collectors increase the number of contact points and therefore decrease the resistance of thick electrodes. Besides, the foams of carbon, nickel, copper, etc. and networks of 1D or 2D materials can be used as 3D current collectors for percolation networks in conventional slurry coated electrodes.

The electronic conductivity of the electrode is ensured by the percolation network formed by the conductive agent and the electrode particles, which can be adjusted by tuning the conductive additive ratio. The percolation theory [155-157] indicates that for a random distribution of a conductive stick model, the density of the conductive sticks at the threshold of forming a percolation network is given by

$$l\sqrt{\pi N_c} = 4.236 \qquad \textbf{Equation 39}$$

where l is the length of the conductive stick, N_c is the percolation threshold, i.e. the density of the conductive sticks. The general message from Equation 39 is that at a greater length (aspect ratio) of the conductive agent, the amount of agent can be lower to achieve a conductive percolation network. Advanced electrode design involves a percolation network formed by 1D or 2D materials with a lower threshold but high conductivity as well as the potential for free-standing electrodes. Conventional conductive agent carbon black can be perceived as 0D material and requires binders (often insulating) to form electrode sheets, while e.g. 1D CNTs and 2D rGO can form a percolation network by mechanical interlocking, entangling or self-assembly, thus eliminating the use of binders and increasing energy density.

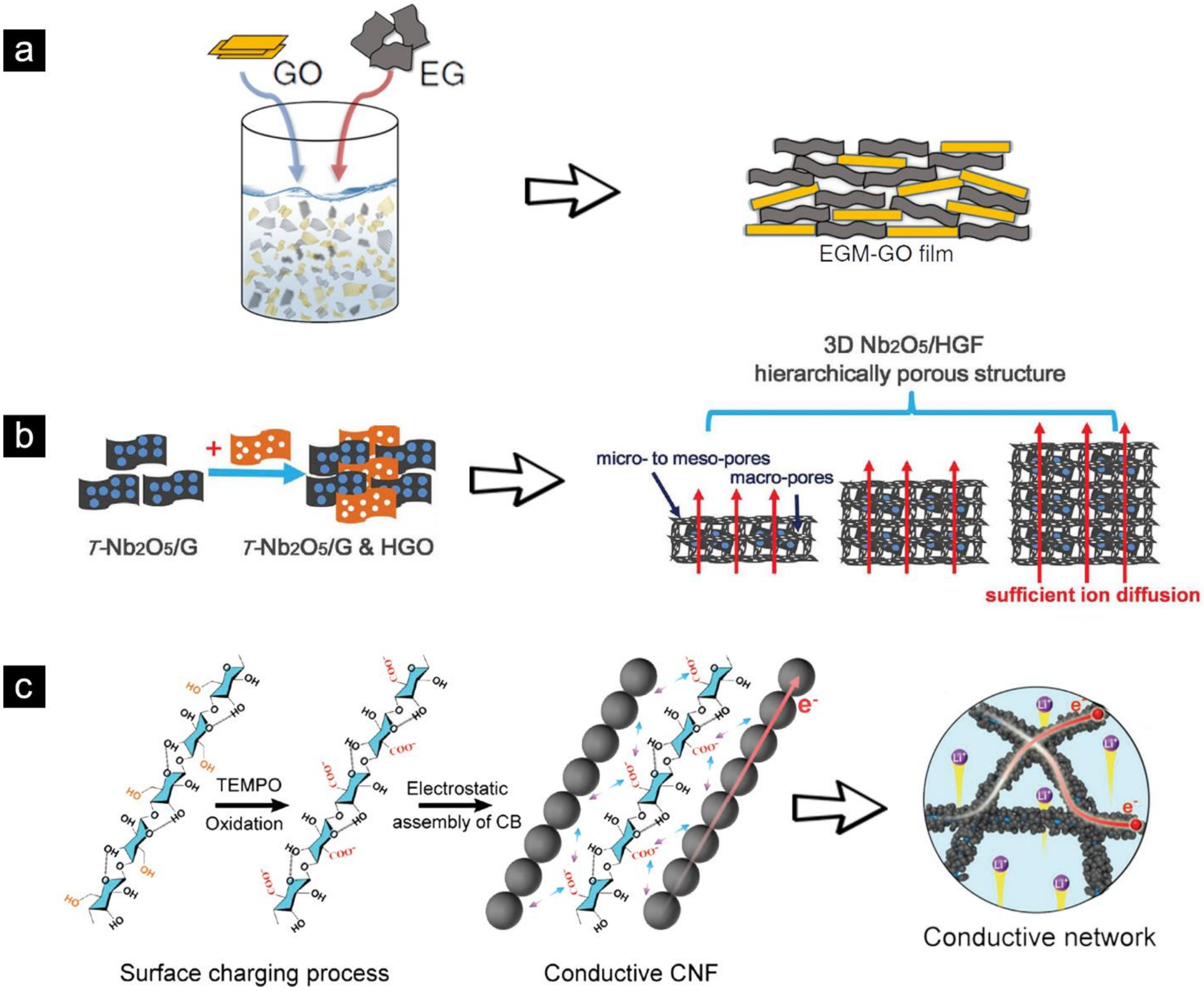

Figure 24. Percolation networks form by graphene, rGO, and conductive cellulose nanofibrils (CNF). (a) GO and EG (exfoliated graphene) form the EGM-GO (exfoliated graphene mediated graphene oxide) electrode [158]; (b) HGO (holey graphene oxide) composites with the Nb_2O_5/G (G stands for graphene) to form hierarchical porous electrode [159]; (c) Surface charged CNF absorb CB (carbon black) and forms a conductive network of the electrode [160]. (Permissions from Springer Nature, AAAS and Wiley)

For the 2D materials graphene or rGO, the restacking remains a challenge for the application. Restacking blocks the ionic pathway and deteriorates the performance, which may be prevented by pore engineering or adding “pillar” materials. A composite material of exfoliated graphene mediated GO film is free from the restacking of graphene or GO since they are the “pillar” material to each other, and the device shows a high volumetric energy density up to 88.1 Wh l^{-1} at a mass loading of 10 mg cm^{-2} (Figure 24a) [158]. Holey graphene and niobium composite presents a successful demonstration for the synergy of both approaches: achieving no limitation has been reached in mass loading at the rate of 10C (which corresponds to a current density of 22 mA cm^{-2}) at mass loading up to 11 mg cm^{-2} (Figure 24b) [159]. A percolation network with the feature of the free-standing electrode at a reduced production cost compared with CNTs and rGO may be achieved with cellulose nanofibrils together with carbon blacks (Figure 24c) [160]. The long cellulose nanofibrils with the surface coated by the 0D carbon black particles create the expressway for electron transport. This was demonstrated for $LiFePO_4$ materials, but the method may be implemented for capacitive materials [160].

The principle of the thick electrode approach for enhancing energy density is reducing the inactive component fraction. Along this vein, making the conventional inactive component, for example, electrolytes and binders, multifunctional to be active in energy conversion or storage is also a feasible way to enhance energy. Redox electrolyte has been studied quite intensively in recent years [79, 80], while the redox-active binder materials have been just demonstrated a few [161].

3.1.3 Device-level optimizations

3.1.3.1 Asymmetric design

Through a proper device design, the capacity and voltage can be improved to greater values and energy density can thus be maximized. The consideration of charge flow balance (charge conservation) between the positive and negative electrodes, i.e. Equations 40-41, poses several solutions to increase the working voltage range and thus working potential.

$$m_P C_P \Delta E_P = m_N C_N \Delta E_N \qquad \text{Equation 40}$$

or

$$m_P Q_P = m_N Q_N \qquad \text{Equation 41}$$

where m, C, ΔE and Q represents the mass, specific capacitance, working potential window and specific capacity, respectively, and the subscript label P and N refer to positive and negative electrodes.

Assuming in a device that the positive electrode show capacitive behavior within a potential range between E_{P1} to E_{P2}, as shown in **Figure 25**, and the negative electrode is within E_{N1} to E_{N2}, thus the limits of capacitive potential range (CPR) of the two electrodes are

$$CPR_P = E_{P2} - E_{P1} \qquad \text{Equation 42}$$

$$CPR_N = E_{N2} - E_{N1} \qquad \text{Equation 43}$$

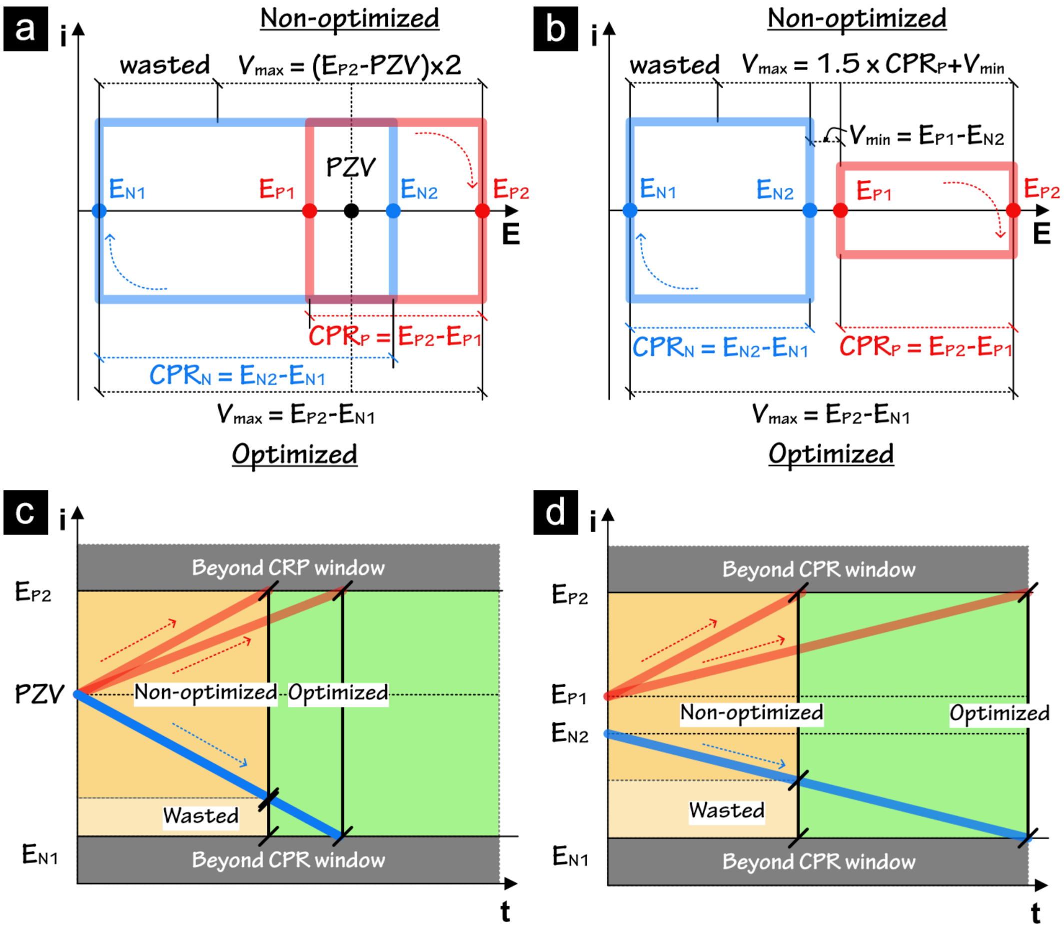

Figure 25. Schematic of electrode potentials variations during operation. (a) CV responses of positive and negative materials, assuming a case where the two electrodes have equal specific capacitances ($C_P = C_N$), and $E_{P1} < E_{N2}$. The non-optimized case assumes $m_P = m_N$; (b) CV responses of positive and negative materials, assuming a case where $C_P = 0.5 \times C_N$, and $E_{P1} > E_{N2}$. The non-optimized case assumes $m_P = m_N$. (c) Schematic of the potential change during galvanostatic charging, corresponding to the assumed case in (a); (d) Schematic of the potential change during galvanostatic charging, corresponding to the assumed case in (b). The dash arrows represent the direction of potential change during operation.

In many cases, the *CPR* range of the positive electrode overlaps that of the negative electrode, i.e. $E_{N2} > E_{P1}$ (Figure 25a, c). Then the device can be discharged to 0 V where the potential of positive electrode equals that of the negative electrode, and the equal potential at 0 V is defined as the potential of zero voltage (*PZV*). If $E_{N2} < E_{P1}$, the EC can only be discharged to a minimum operating voltage $V_{\min}$ defined by E_{P1} - E_{N2}, instead of 0 V, which is the case in Figure 25b, d.

When an EC is being charged, the potential of the positive electrode increases while the negative electrode potential decreases (following the arrows in Figure 25). The rate of potential change depends on the electrode mass and the specific capacitance so that the charge flow is always balanced. $V_{\max}$ is thus determined until either of the electrodes is ramped up to its potential limit (E_{P2} or E_{N1}). The electrode that first reaches its boundary potential is the *voltage-limiting electrode*. As an example in Figure 25a, the positive electrode is voltage-limiting, then there is a wasted potential on the negative electrode that is not exploited yet applicable for capacitive charge storage. To optimize the system to fully maximize $V_{\max}$, the capacitance of the positive electrode should be increased. This can be done by asymmetric design with the following methods.

(1) Method 1 - Increasing the mass of the voltage-limiting electrode

When loading a higher amount of material on the positive electrode, i.e. increasing the m_P in Equation 40, the working potential range of the negative electrode ΔE_N is accordingly enlarged, since other factors (C_P, ΔE_P, m_N, and C_N) remain unchanged in the equation. Because the reference potential *PZV* is relatively stable in EDLCs [162-165], the negative electrode potential is stretched to its limit of E_{N1}, and the $V_{\max}$ optimization is thus achieved. The theoretical mass ratio can be calculated through

$$\frac{m_P}{m_N} = \frac{C_N \cdot (PZV - E_{N1})}{C_P \cdot (E_{P2} - PZV)} \qquad \text{Equation 44}$$

This requires an experimental determination of electrodes' specific capacitances (C_P and C_N), the potential limits (E_{N1} and E_{P2}, mostly determined by electrolyte stability window) and *PZV*. For this purpose, in addition to the common two-electrode setup, a conventional three-electrode cell is needed to examine the stability window of electrolytes, which can also be used for a rough estimation of C_N and C_P. Besides, a special two-electrode system equipped with a reference electrode (T-type Swagelok cell used in **Paper I** is shown in Figure 8c) to gather information on the real-time change of electrode potential during device operation, measure the *PZV* and exactly calculate the electrode capacitances.

With this method (mass-balancing), it was demonstrated that $V_{\max}$ has been optimized in EDLCs with aqueous electrolytes [164-166], as shown in Figure 26. Similar cases can also be found in ionic liquid systems [167, 168].

It is quite common that the positive electrode is usually the voltage-limiting electrode in symmetric EDLCs, especially in neutral aqueous systems. This may be partly attributed to the fact that the negative electrode potential can be extended to a rather low potential by taking advantage of nascent hydrogen storage and thereby large HER (hydrogen evolution reaction) overpotential, making a large *CPR* range of the negative electrode.

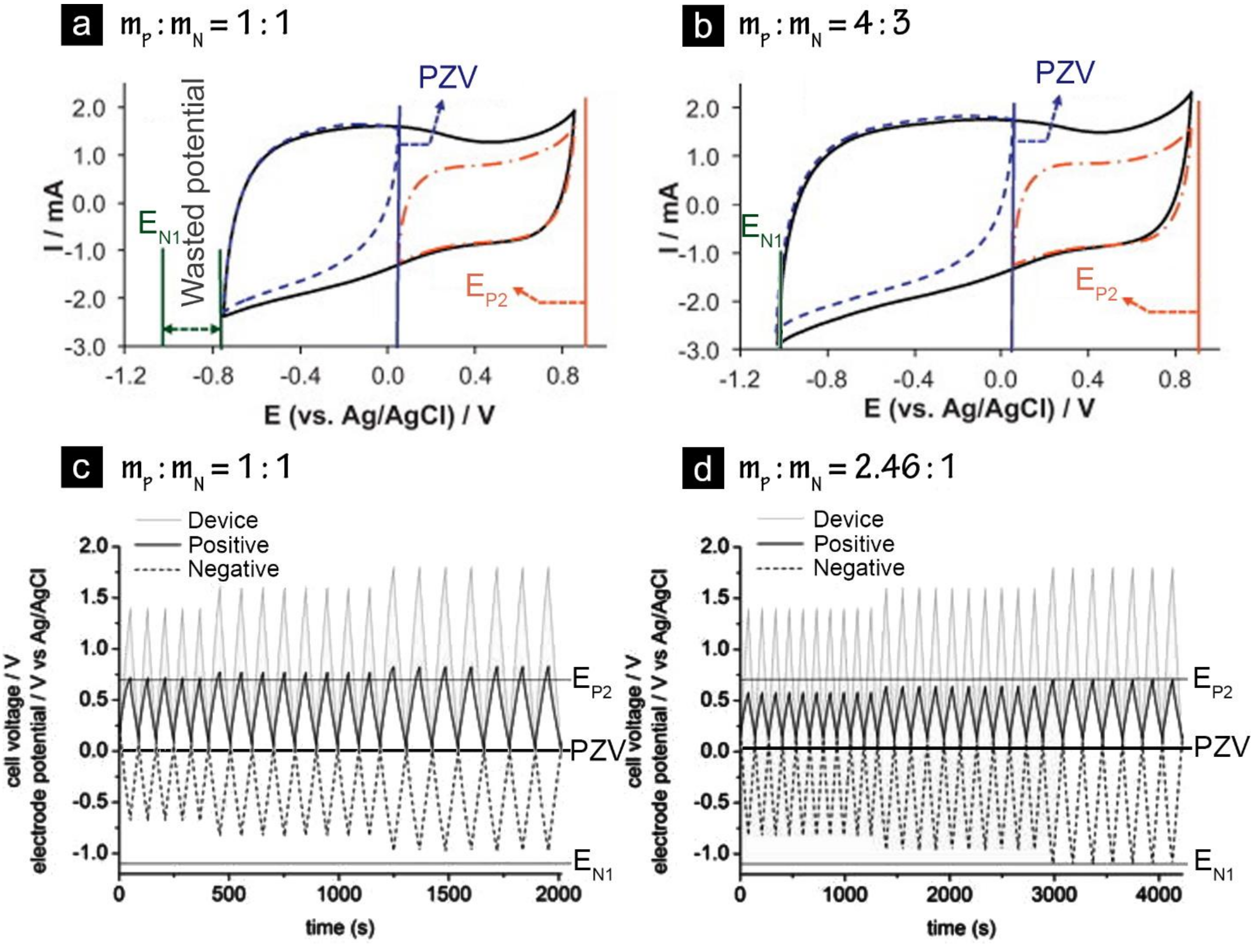

Figure 26. CV curves of a carbon electrode in a conventional three-electrode cell (0.3 M K_2SO_4) with *PZV* and working potential ranges (dashed curves) determined by a T-type cell: (a) non-optimized and (b) optimized [164]. GCD curves of device and electrodes at an operating voltage of 1.4, 1.6 and 1.8 V with E_{P2} and E_{N1} determined by a conventional three-electrode cell: (c) non-optimized and (d) optimized [165]. (Reproduced with permission from Elsevier and ESG)

(2) Method 2 - Increasing the specific capacitance of the voltage-limiting electrode

Similar to the increase of m_P, a higher value of C_P (while keeping others unchanged) leads to the same effect that E_N is stretched according to Equation 40.

It is worth noticing that a symmetric device exhibits asymmetric behavior. For symmetric EDLCs with the same porous carbon on both sides, the specific capacitance of positive and negative electrodes are *NOT* equal. A maximized specific capacitance is achieved when matching the pore size with the ion size [117, 169]. The sizes of cations and anions in an electrolyte are different, leading to a different degree of matching thereby different capacitances on the two electrodes.

Therefore, one can construct an asymmetric device by using a different carbon material with respect to the selection of electrolyte ions, to increase C_P and optimize V_{max}. This method could retain the most power capability and cycling stability of EDLCs. A more substantial change to the system is through replacing carbon with a pseudocapacitive material, i.e. asymmetric devices. Except for a high specific capacitance, another possible beneficial aspect of using pseudocapacitive materials is a high H_2O decomposition overpotential. For example, a high OER (oxygen evolution reaction) overpotential on a MnO_2/CNTs composite was found independent of the electrolyte pH [170] as shown in Figure 27a. Thermodynamically, OER potential at pH = 10 is 0.64 V and at pH = 6.4 is 0.85 V vs. NHE (normal hydrogen electrode). Experimental results show that the MnO_2 material can be polarized to a much higher potential without showing oxygen evolution, making it a suitable positive electrode material candidate. The maximum operating voltage of a device with an activated carbon negative electrode is possible to be over 2 V with optimization (Figure 27).

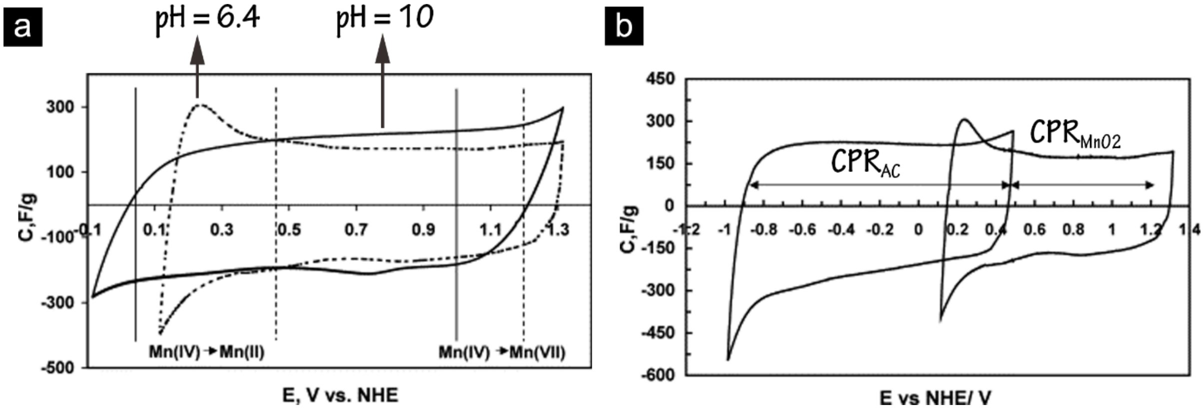

Figure 27. CV curves of MnO_2 in KOH (pH = 10) and KNO_3 (pH = 6.4) and (b) CVs of activated carbon and MnO_2 in KNO_3 solution (pH = 6.4) [170]. (Reproduced with permission from Elsevier)

Further, replacing the carbon electrode with another pseudocapacitive material will result in asymmetric devices based on all pseudocapacitive electrodes [150]. Constructing this type of device is an effective approach to maximizing $V_{\max}$ in aqueous media, but the application of organic electrolytes for a further boost in voltage limit remains a challenge [102]. Moreover, it is rather clear that a lack of cycling stability is a barrier for this type of device to be applied in self-powered systems - a considerable amount of demonstrations show capacitance retention less than 90% over only 5 000 cycles. A solution to this problem relies on materials development.

(3) Method 3 - Pinning the electrode potential of the voltage-limiting electrode

Another way of perceiving an apparent “increase in capacitance” is by slowing down the rate of potential increase during charging, i.e. a smaller slope on the GCD curve. Along this line, an extreme situation is that the potential of the voltage-limiting electrode (E_P in the case of Figure 25) is “pinned” at a certain value, then the potential range of the other electrode is thus stretched according to Equation 40. Pinning the electrode potential is effectively introducing a battery-like behavior that displays a plateau on GCD curves, and therefore hybrid ECs. Since battery behavior cannot be interpreted as capacitance, Equation 40 is converted to Equation 45 for those devices where a battery-like behavior appears on the positive electrode, or Equation 46 for the negative electrode counterparts.

$$m_P Q_P = m_N C_N \Delta E_N \qquad \text{Equation 45}$$

$$m_P C_P \Delta E_P = m_N Q_N \qquad \text{Equation 46}$$

where Q_P and Q_N refer to the specific capacities (C g^{-1} or Ah g^{-1}) of the battery-like electrodes.

It can be argued that between the two general methods for constructing hybrid ECs (incorporating battery electrode material or employing redox electrolytes), the use of redox electrolytes is more effective to improve the energy while keeping the high power and cycling stability, since it is developed on the base of EDLCs. The dimensional change caused by e.g. intercalation/deintercalation reactions of battery electrodes significantly impact their lifetime, which is highly detrimental for IoT applications.

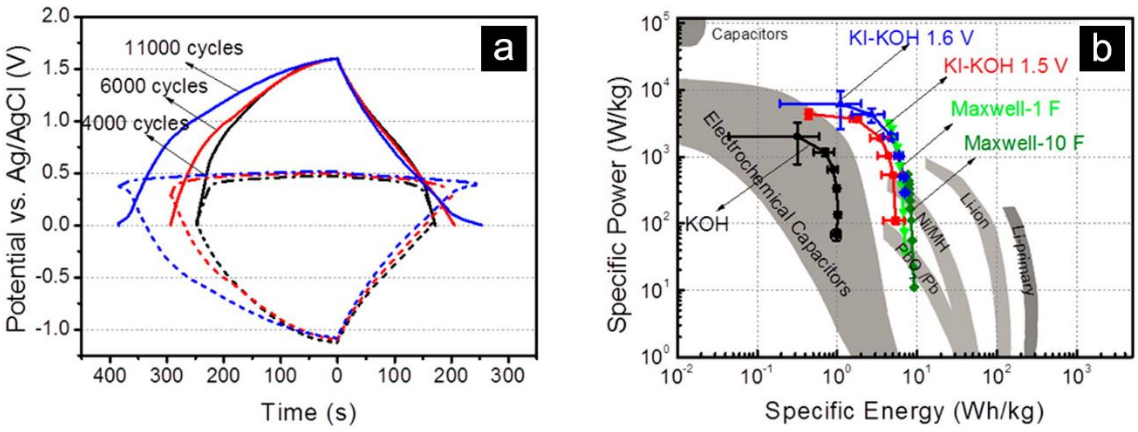

Figure 28. (a) GCD curves f device and electrodes at 1.6 V with KI-KOH electrolyte. (b) Ragone plot comparing energy and power densities with other systems [171]. (Reproduced with permission from ACS)

An example of pinning the electrode potential is shown in Figure 28 where the electrolyte is 4 M KI mixed with 1 M KOH [171]. Faradaic energy storage originates from iodine related reactions as

$$I^- + 6OH^- \rightarrow IO_3^- + 3H_2O + 6e^- \qquad \text{Equation 47}$$

The reaction generates a long plateau on the positive electrode, making the electrode potential E_P to be pinned at around 0.5 V vs. Ag/AgCl reference electrode (Figure 28a). The negative electrode potential is stretched to as low as around -1.1 V, with its *CPR* range fully exploited. The pinned potential prevents the potential from going further to invoke OER, therefore H_2O is protected from decomposition by the redox reaction. V_{max} of the aqueous electrolyte device is as high as 1.6 V, even with the presence of an alkaline KOH. The device operating at 1.6 V shows an improved energy density and an EC level power density is retained in this system (Figure 28b).

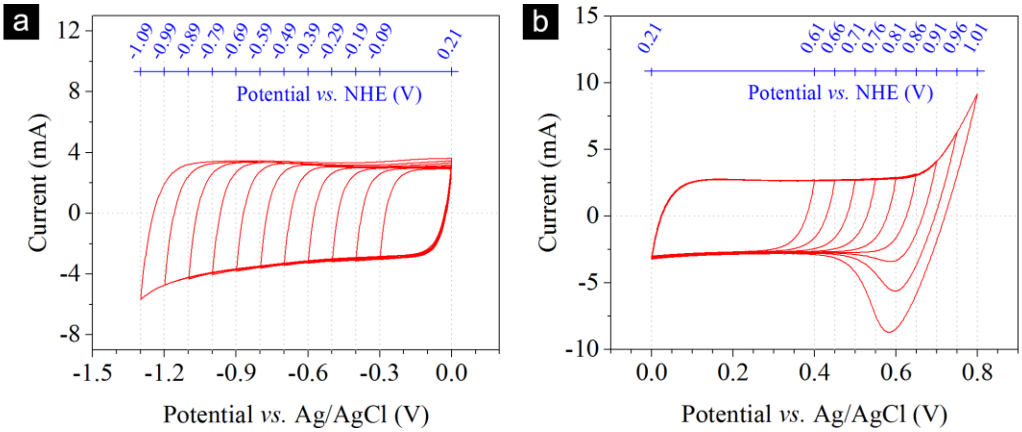

Figure 29. (a) Negative and (b) positive CV scans in a three-electrode cell with 1 M KBr (**Paper I**). (Reproduced with permission from Elsevier)

In **Paper I**, it is found that KBr in a simple form of salt is an effective redox-active electrolyte and also displays a pinning effect. The redox reaction starts to take place in terms of

$$3Br^- \rightarrow Br_3^- + 2e^- \qquad \text{Equation 48}$$

at a potential of about 0.65 V *vs.* Ag/AgCl, determined by CV scans of 1 M KBr with an AC working electrode (Figure 29b). The cathodic current during the negative scan (Figure 29a) increases continuously with the voltage ramping. No dramatic change is observed until -1.30 V although it seems -1.2 V is around the limit for a pure capacitive behavior. This indicates that a large overpotential of HER exists on the negative electrode. If E_{P2} is pinned by the redox reaction, E_{N1} will be stretched to a low potential and then a large V_{max} can be expected.

We measured the performance of a KBr-containing device with two identical AC electrodes at different V_{max} shown in Figure 30a-b. The experiment indicated that the device can reach 1.9 V without compromising stability in this aqueous system, which is remarkable considering the simplicity of the system. The electrode potential values were recorded using the T-type Swagelok cell. As shown in Figure 30, E_{P2} finally tends to saturate at around 0.8 V vs. Ag/AgCl when the cell operates at 1.9 V, which is close to the standard electrode potential of 0.84 V vs. Ag/AgCl for the redox reaction. Accordingly, E_{N1} eventually decreases to about -1.1 V. The 1.9 V high voltage aqueous device shows considerable improvement in energy density and its power density remains high (Figure 30d). Moreover, the energy efficiencies are still as high as 87.6% when battery-like reactions are heavily involved at 1.9 V.

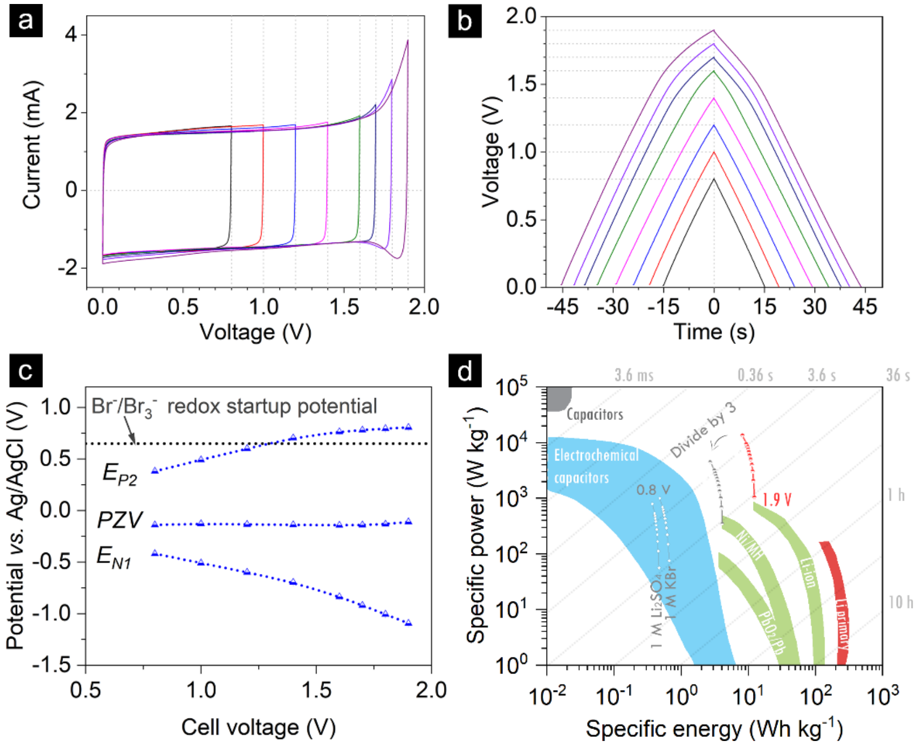

Figure 30. KBr-containing device: (a) CV scans and (b) GCD curves from 0.8 to 1.9 V, (c) variation of electrode potential as a function of operating voltage, and (d) Ragone plot (**Paper I**). (Reproduced with permission from Elsevier)

The approach of pinning electrode potential seems to be effective for developing ECs for self-powered systems, in terms of increasing energy at high power and high stability. Nevertheless, one should be cautious about the complexity of the system. The introduction of redox activity causes *voltage-dependent behavior* - it behaves as pure EDLC up to 1.6 V, and then hybrid features appear from 1.7 V and above. Moreover, we have also observed a *history-dependent behavior*. As shown in Figure 31, the GCD curve "swells" with the cycling process at 1.9 V operation. If the device is pre-cycled at 1.9 V for 500 cycles and then operated at 1.6 V, a small portion of redox activity is "triggered", evidenced by the changing of the GCD curve slope towards the high voltage (Figure 31c), in contrast to the pure EDL behavior when directly operated at 1.6 V (Figure 31a). We designate the pre-cycling process as a "triggering operation". The history-dependent behavior is accompanied by a variation of E_{N1}, E_{P2}, and *PZV* caused by complex redox chemistry as well as the transport and storage of redox-active ions. We believe the observations are not unique to KBr, but also to other redox enhanced EDLC systems. Therefore, one should be aware of these changes in the storage mechanism, and evaluate them carefully before bringing them into practical application.

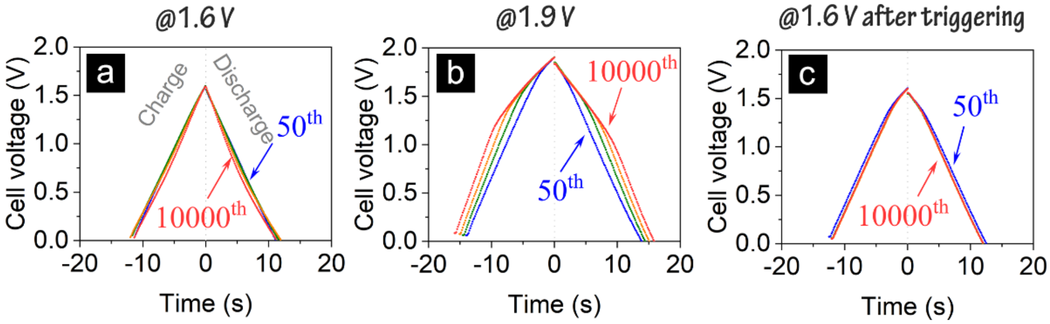

Figure 31. The history-dependent behavior of KBr-containing devices: GCD curves at specified cycle numbers at (a) 1.6 V, (b) 1.9 V and (c) 1.6 V after a triggering operation (**Paper I**). (Reproduced with permission from Elsevier)

A similar storage behavior evolution is reported in an iodine redox electrolyte system (Figure 32) [172]. When the mass ratio of $m_P : m_N$ is set as 2:1, the device behavior evolves from linear to non-linear, along with capacitance decay, over 100 GCD cycles. While with the mass ratio optimized to 1:2, the behavior changes and stability loss was avoided.

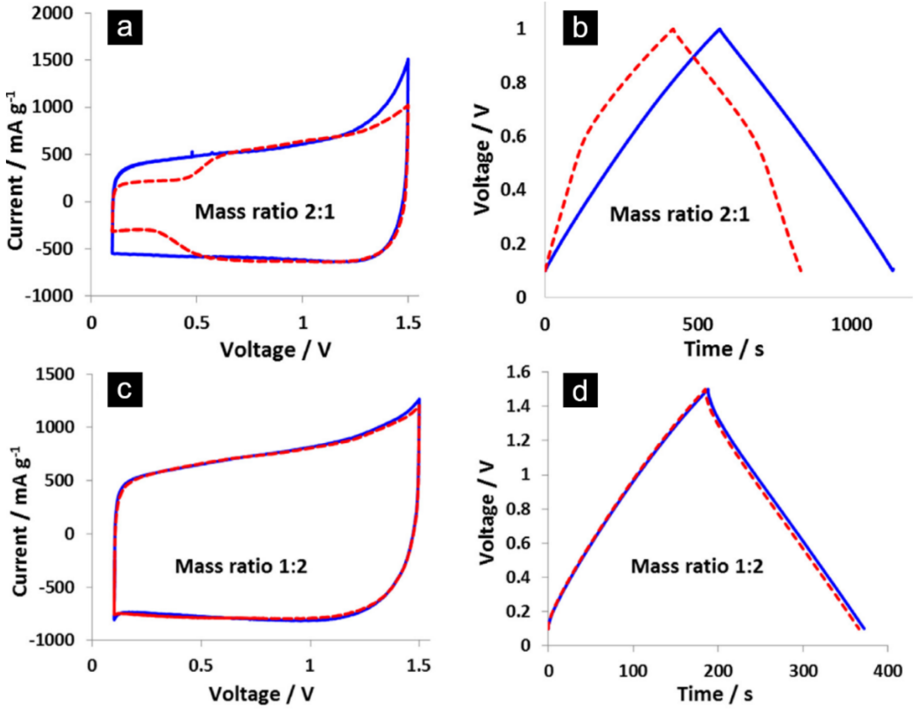

Figure 32. Mass balancing to avoid behavior change in 5 M $NaNO_3$ and 0.5 M NaI electrolyte with AC electrodes. (a-b) CV and GCD curves before (solid) and after (dash) 100 GCD cycles at m_P:m_N = 2:1 [172]; (c-d) CV and GCD curves before (solid) and after (dash) 100 GCD cycles at m_P:m_N = 1:2 [172]. (Reproduced with permission from Elsevier)

(4) Method 4 - Tuning PZV

PZV is a reference point of potential from which the two electrodes start to work. If *PZV* can be tuned to shift away from the *CPR* of the voltage-limiting electrode, V_{max} is enlarged. For example in Figure 25, a downshift of *PZV* towards E_{P1} would exploit the maximum *CPR* of the positive electrode, and at the same time, the working potential of the negative electrode is enlarged accordingly following a balanced charge flow i.e. Equation 40. Therefore, *PZV* is an important parameter that affects V_{max}, however, it is difficult to predict its exact value in practice, but it is located within the open-circuit potentials of the positive and negative electrode. It is believed that when operated at 0 V, there is a fast potential balance between the two electrodes and *PZV* is determined when the balancing process reaches equilibrium [173].

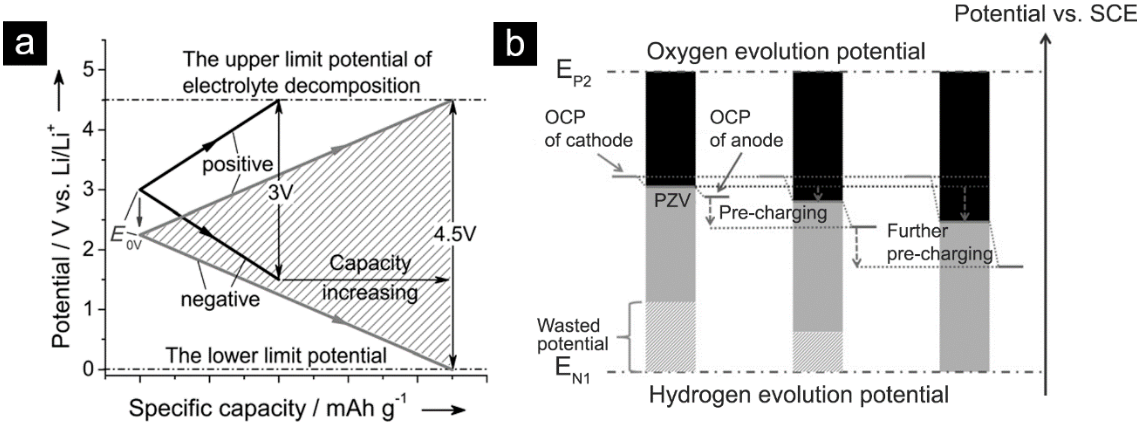

Figure 33. Charge injection and pre-charging methods of tuning *PZV*. (a) Charge injection to downshift the *PZV* (E_{0V}) of a graphene-based EC with 1 M $LiPF_6$ in EC/DMC electrolyte [174]; (b) Pre-charging method employed in an EC with 5 M LiCl electrolyte [173]. (Reproduced with permission from Wiley)

The charge injection method was demonstrated to maximize the energy density of a graphene-based EC (Figure 33) [174]. Researchers first assembled two half-cells with two identical graphene electrodes. Then one of the two cells was discharged the one to 1.16 V vs. Li/Li$^+$ and held at this voltage for 2 hours for stabilizing the injected charge, while the other cell was first cycled between 0.01 to 1.16 V until a solid electrolyte interface (SEI) film was formed and subsequently held at 1.16 V for 2 hours. The two half cells were disassembled and the electrodes were retrieved and assembled again for the final EC, with the first electrode as the positive and the other as the negative. The *PZV* was brought down from above 3 V to 1.16 V, and the maximum voltage range is increased to 4.5 V.

Along with this vein, researchers pre-charged the voltage-limiting electrode (positive electrode) at lower potential values than its OCP in a conventional three-electrode cell, then assembled the device with the pre-charged positive electrode, and managed to downshift *PZV* to from 0.17 to -0.1 V vs. SCE (saturated calomel electrode). The downshift of *PZV* leads to utilization of wasted potential on the negative electrode, and finally optimized V_{max} from 1.4 to 1.8 V in 5 M LiCl electrolyte [173]. The schematic of *PZV* tuning by pre-charging is shown in Figure 33b.

Besides the charge injection and pre-charging method, there can be other applicable methods, especially when redox reactions are involved and the surface charge of the electrode becomes complex. The complexity can allow for the possibility of more tuning methods or even self-adjustment of *PZV*. *PZV* shifts can be caused by the “triggering operation” in the KBr-containing system, i.e. the *PZV* shifts positively over the cycling process at 1.9 V (Figure 34a), but remains stable when cycling at 1.6 V. However, it is not clear at the moment how to manipulate the *PZV* in this system. A recent study [172] indicates that the mass ratio of positive to negative electrodes can influence the *PZV* in redox electrolyte systems. When the mass ratio of $m_P : m_N$ changes from 1:1 to 1:2, the *PZV* shifts positively. Therefore, the 1:2 cell is less prone to hydrogen evolution side reactions on the negative side, and the cycling stability is enhanced. The *PZV* shift was explained qualitatively relating to the immobilization of iodide inside the pores.

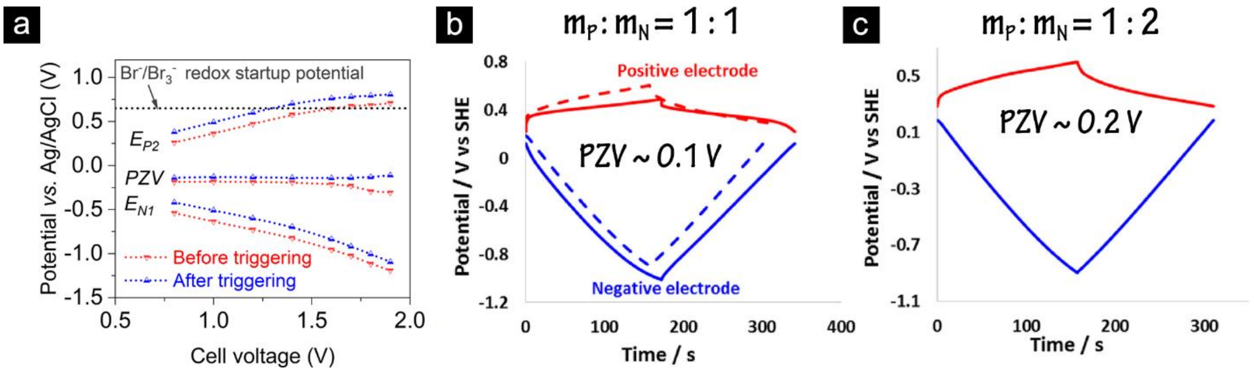

Figure 34. *PZV* shift in redox electrolyte systems. (a) In the KBr electrolyte in **Paper I**, *PZV* shifts positively during pre-cycling at 1.9 V (triggering operation); (b-c) In a 5 M $NaNO_3$ + 0.5 NaI electrolyte system in ref. [172], *PZV* shifts positively by changing the mass ratio; *PZV* also shifts positively after 100 cycles (dash line) for the m_P:m_N = 1:1 cell. (Reproduced with permission from Elsevier)

3.1.3.2 Bipolar design

Bipolar design of storage devices is an effective way to increase the maximum operating voltage, and it also increases the overall energy density because of the reduction in inactive component fraction. In essence, a bipolar design is simply to stack devices, but through bipolar electrode plates. A bipolar electrode plate can serve as a current collector for a positive electrode in one cell, while as a negative electrode’s current collector in the adjacent cell. In this way, only N+1 plates are needed for stacking N devices, while normal stacking requires 2N plates together with 2N individual packages. The bipolar design was demonstrated for a 20 V bipolar device consisting of 19 PPy-CNTs (+) | 3 M KCl | AC (-) cells [175]. Other examples of bipolar design devices can be found in references [176-180].

Paper IV designed a bipolar device based on a double-sided graphite/VACNTs (DSGC) material as the bipolar electrode, the single-sided graphite/VACNTs (SSGC) as the terminal electrodes. The VACNTs are grown on both sides of the graphite paper in a one-step self-joule heating method. The schematics of the devices are shown in Figure 35. The electrolyte for the devices is a gel polymer electrolyte PVA/H_3PO_4. The performance comparison indicates a doubling of the operating voltage (Figure 36a) and a 22% volumetric energy density increase compared with a series connection of two unit devices, i.e. device 1× + 1× (Figure 36b). The energy enhancement is obtained from a lower thickness of the device stack because of using one less layer of the graphite paper and one less separator in this case: device 1× + 1× thickness 115 μm, device 2× thickness 70 μm.

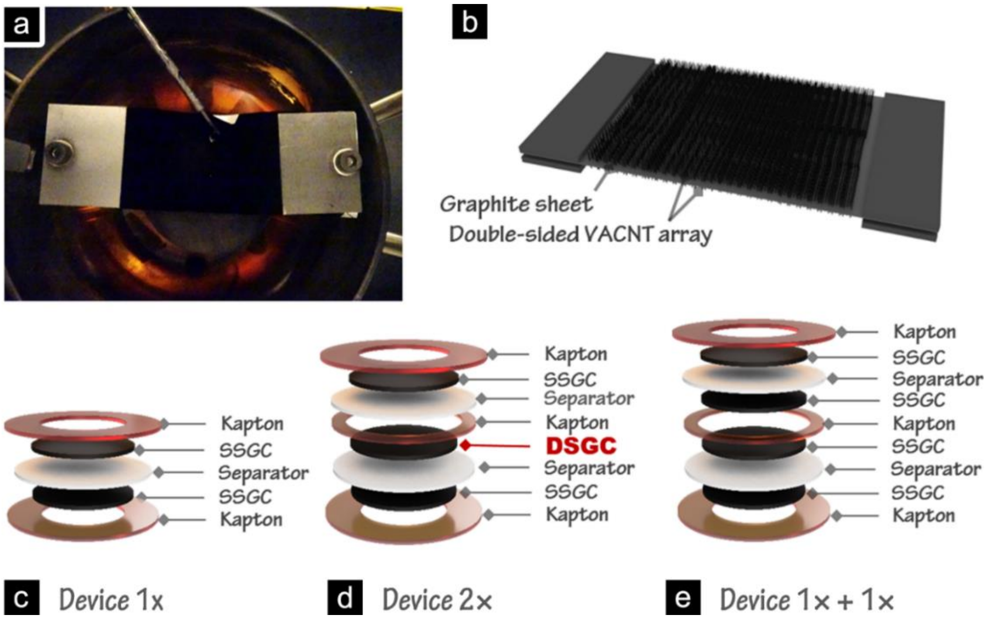

Figure 35. Bipolar design using graphite/VACNTs (**Paper IV**). (a) Picture of the CVD setup for growing double-sided graphite/VACNTs (DSGCs) with the self-joule heating method; (b) Schematic of directly using the graphite sheet as a heater for the self-joule heating CVD growth; (c) Sketch of device 1×, with single-sided graphite/VACNTs as the electrodes; (d) Sketch of the bipolar device 2× with a DSGC as the bipolar electrode; (e) Sketch of device 1× + 1×. (Reproduced with permission from Elsevier)

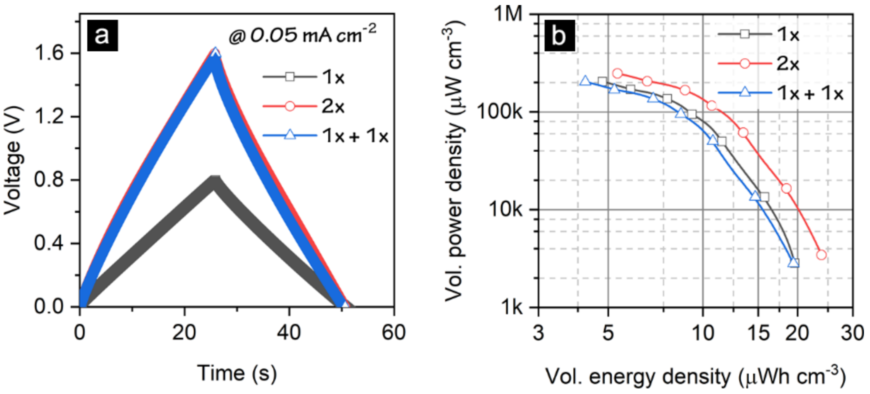

Figure 36. Performance comparison between bipolar devices and regular devices (**Paper IV**). (a) GCD curves of device 1×, 2× and 1× + 1×; (b) Ragone plots of the three devices. (Reproduced with permission from Elsevier)

Assuming the thickness of a unit device is t_0, and a bipolar device (consisting of two units) thickness is t_1. Then the thickness reduction for each added unit in the design is $t_1 - t_0$. For an N-unit bipolar device, the total thickness is $t_0 + (t_1 - t_0) \times (N - 1)$, then the volumetric energy density is expressed as

$$E_{N,vol.} = \frac{N \times E_0}{A_0 \times (t_0 + (t_1 - t_0) \times (N-1))} \quad \text{Equation 49}$$

where A_0 is the footprint area, and E_0 is the energy value of a unit device. For a simple series connection of N unit devices, the volumetric energy density is the same as the unit device

$$E_{0,vol} = \frac{E_0}{A_0 \times t_0} \quad \text{Equation 50}$$

Then the percentage of volumetric energy increase compared to a series connection is expressed as

$$\%Increse = \frac{E_{N,vol.} - E_{0,vol.}}{E_{0,vol}} \times 100\% = \left(\frac{t_0 \times N}{t_0 + (t_1 - t_0) \times (N-1)} - 1\right) \times 100\% \quad \text{Equation 51}$$

Therefore, a limit exists for energy increase through bipolar designs. For the DSGCs based bipolar devices, t_0 is 70 um, and t_1 is 115 um, inserting and solving the equation we can find that the limit is about 55%. Energy density gain is substantial when N is in the range of 2 to 10. Further increasing N does not gain much in energy density, while the operating voltage would keep increasing linearly.

Due to the nature of series connection in bipolar ECs, the capacitance density of bipolar ECs keep decreasing following

$$C_{N,vol.} \propto \frac{1}{V_{max}^2} \equiv \frac{1}{N^2} \frac{1}{V_0^2} \quad \text{Equation 52}$$

where $C_{N,vol}$is the volumetric capacitance for an N-unit bipolar device, $V_{\max}$ is the maximum operating voltage of the bipolar device, and V_0 is the operating voltage of the unit device.

3.1.4 Remarks

Energy density enhancement of ECs towards battery level energy density is a broad and hot topic. The enhancement must be at a limited sacrifice in the power density as well as cycling stability, otherwise, the device is hardly competitive in comparison to high power batteries. A general rule-of-thumb is that ECs should be capable of working in the time range of less than minutes, and batteries in hours. However, exceptions may exist depending on the application scenarios. An EC that can work stably in a capacitive manner under a low current density is wanted for systems coupled with miniature harvesters. The consideration of energy density improvement can be done from material-, electrode- and device-levels. Among a large number of specific solutions in each category for advanced designs, the question remains how to make manufacturing scalable and cost-effective.

Concerning the thesis research work, the redox electrolyte and bipolar design approaches are relevant. The aqueous redox electrolyte system is promising for applications in self-powered systems, considering the effectiveness in energy improvement, low cost of electrolyte and requiring no inert atmosphere for device assembly. The diffusion in a liquid phase can still ensure relatively fast kinetics comparing with diffusion in solid-state for common battery materials. In fact, the adsorption of redox-active species in the micropores of porous carbon limits the diffusion thus the redox reaction proceeds at the interface in a facile manner; the strategy of grafting redox-species through chemical bonding on the carbon surface can further anchor the redox-active sites for better kinetics and less cross-diffusion. However, the incorporation of a redox-active electrolyte in an EDLC system complicates the charge storage mechanism. The KBr enhanced EDLC system in **Paper I** exhibits the intriguing "triggering" phenomenon, and displays continuous changes in the shape of GCD curves at 1.9 V operation, which can cause difficulties in behavior prediction and power management in practical applications. Device design for controlling the shift of *PZV* is essential to stabilize the performance.

As for the bipolar designs, it reduces the inactive component fraction for energy density enhancement. Exploiting advanced materials and designs for the bipolar plate can further strengthen this advantage in energy enhancement. The bipolar design is perhaps more known for the purpose of increasing the maximum operating voltage. When using high voltage bipolar devices for low voltage applications, each unit cell works at only 1/N of the voltage applied on the device, which is beneficial for achieving slow self-discharge or low leakage current, as well as high cycling stability. The main drawback associated with a bipolar design is its relatively complicated manufacturing process. Unit cells must be isolated from each other, which is challenging when using liquid electrolytes, and especially when fabricating miniature devices for microsystems. Employing solid- or quasi-solid-state electrolytes can alleviate the problem. Furthermore, the bipolar design requires high uniformity of unit cells, meaning that the cells should have the same capacitance, working voltage range, etc. Otherwise, the system is not balanced and lifetime is thus seriously shortened, similar to battery system balancing. Another concern comes with the fact that malfunction of any unit cell in a series connection leads to a failure of the whole device. Therefore, the bipolar design poses very high requirements for manufacture engineering.

3.2 Towards high operating voltage

The discussion of improving operating voltage is inseparable from the discussion of improving energy density. The previous section has presented the strategies of improving the energy density through the device-level optimizations, i.e. the asymmetric design and bipolar design. This section emphasizes the material-level optimization for higher device operating voltage.

3.2.1 Interaction between electrodes and electrolytes

Electrolyte materials play a decisive role in determining the maximum operating voltage. In general, aqueous-based electrolytes work at a lower voltage of below 2 V, organic electrolytes enable voltage up to 3 V and ionic liquid electrolytes can withstand more than 3 V. By reviewing the research progress in carbon-based devices, it can be found that the maximum operating voltage, using the same type of electrolyte, can be significantly different, as shown in Figure 37, highlighting the important role of the interplay between electrode properties and electrolyte.

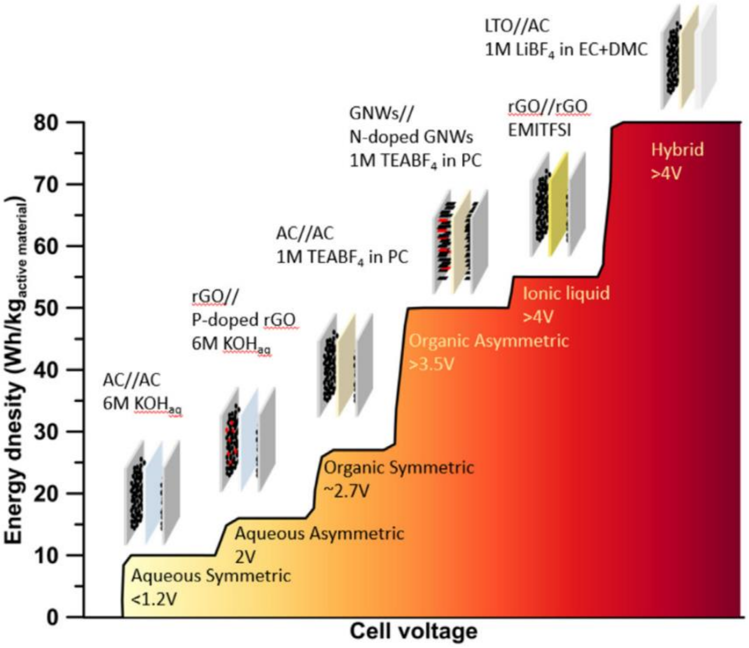

Figure 37. The device voltage and energy density with different electrolytes and configurations [123]. (Reproduced with permission from Elsevier)

It is generally acknowledged that the electrochemical stability window of the electrolyte defines the operating voltage (note the misconception of relating HOMO and LUMO the stability window [181]). The interaction of the electrode surface and the electrolyte can either extend or shorten the stability window of pure electrolytes.

For the aqueous systems, the overpotential of HER and OER reactions extensively enlarge the operating voltage well above the thermodynamic limit of 1.23 V. For neutral aqueous electrolytes, the overpotential is caused by (1) H^+ and OH^- equilibrium. The concentrations of H^+ and OH^- ions in a neutral electrolyte are extremely low, hence neither hydrogen nor oxygen evolution is favored. (2) Strong solvation of both cations and anions [182]. Cations and anions exist in the form of hydrated ions, and the surrounding H_2O molecules have to depart from the hydration shell before getting involved in H_2 or O_2 evolution reactions (HER or OER). The extra energy required for dehydration contributes to an overpotential to HER or OER. (3) Hydrogen electrosorption in micropores of the carbon electrode [183, 184]. A record-high voltage of 2.2 V was demonstrated for 1 M Li_2SO_4 electrolyte with AC//AC symmetric configuration, following 2.0 V for 0.5 M Na_2SO_4. Proper device optimization can lead to 1.9 V in K_2SO_4 by mass-balancing, and 1.9 V in KBr redox enhanced symmetric system. Taking advantage of the overpotential of OER on pseudocapacitive electrode MnO_2 and the overpotential of HER on AC electrodes, a 2.4 V operation voltage can be achieved using 0.5 M Na_2SO_4 [185]. With a proper selection of electrodes and specialized device design, a 4.2 V aqueous device is possible [186]. The water-in-salts electrolyte (WiSE) [187] concept (highly concentrated LiTFSI salt solution) also promises high voltage aqueous electrolytes (2.4 V [188], 2.9 V [189]) enabling high energy devices, but there is a clear trade-off between an improved energy density and decreased power density and cycling stability [188]. Concentration optimization is needed to minimize this effect.

For organic electrolyte systems, the intrinsic electrochemical stability window is usually high. For example, the commonly used solvents PC and AN have a stability window of 6.6 V and 6.1 V, respectively. However, the achievable voltage window for practical devices can be as low as 2.7 V for commercial cells. The comprised window is due to the side reactions due to the impurities in the electrolyte, and the oxygen-containing functional groups (OFGs) on the carbon surface, the adsorbed water in porous carbons as well as carbon defects. The general strategies for improving the performance of AC in organic systems are (1) removal of OFGs; (2) incorporating heteroatoms into carbon; (3) attachment of hydrophobic groups to the carbon surface. The side reactions with OFGs can also be suppressed through surface passivation, in a similar way to the SEI layer on graphite anode in LIBs and LICs. Moreover, the operating voltage of organic electrolytes in AC devices is influenced by the size of ions. Studies on the influence of salts on the maximum voltage in organic systems indicate that cations of larger size are less susceptible to electrochemical reduction and therefore beneficial for high voltage [190].

For ionic liquid-based systems, the reason for compromised stability window is similar to that of organic systems, and the size match between the pore and the electrolyte ions is also critical for the operating voltage. It was shown that the asymmetric behavior of the electrolyte cation and anion toward the two electrodes limits the voltage [191], the corresponding solution to this problem was proposed by formulating the IL electrolyte mixtures to balance the capacitance of electrodes in a symmetric EC [192].

3.2.2 Service windows of electrodes and redox electrolyte species

As a result of the thermodynamics, as well as the interplay with the electrolyte, electrode materials can exhibit distinct stability windows in various types of electrolytes. The service potential range of a variety of common electrode materials in aqueous and organic media, as well as redox potentials of redox electrolyte species, are generalized in Figure 38 [150] and Figure 39 [193, 194], which can be used as a reference map for materials selection when designing high voltage and high energy ECs.

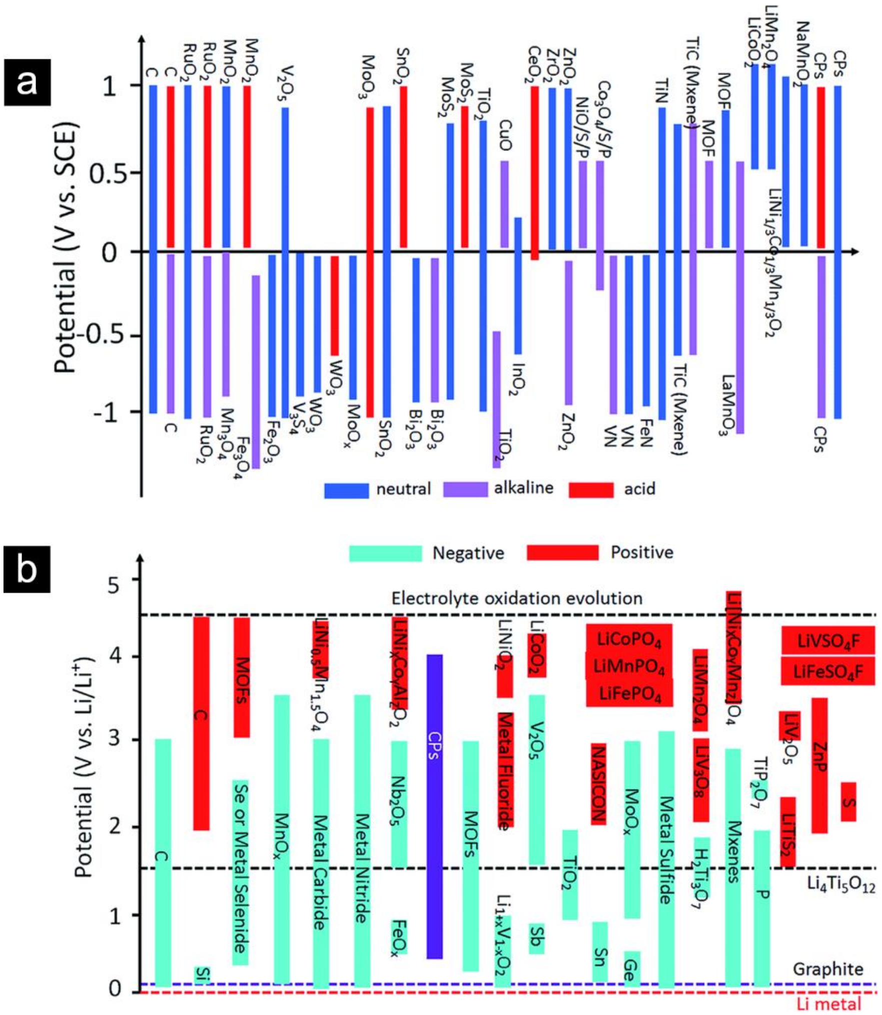

Figure 38. Working potential windows of electroactive materials in (a) aqueous and (b) organic electrolytes [150]. (Reproduced with permission from RSC)

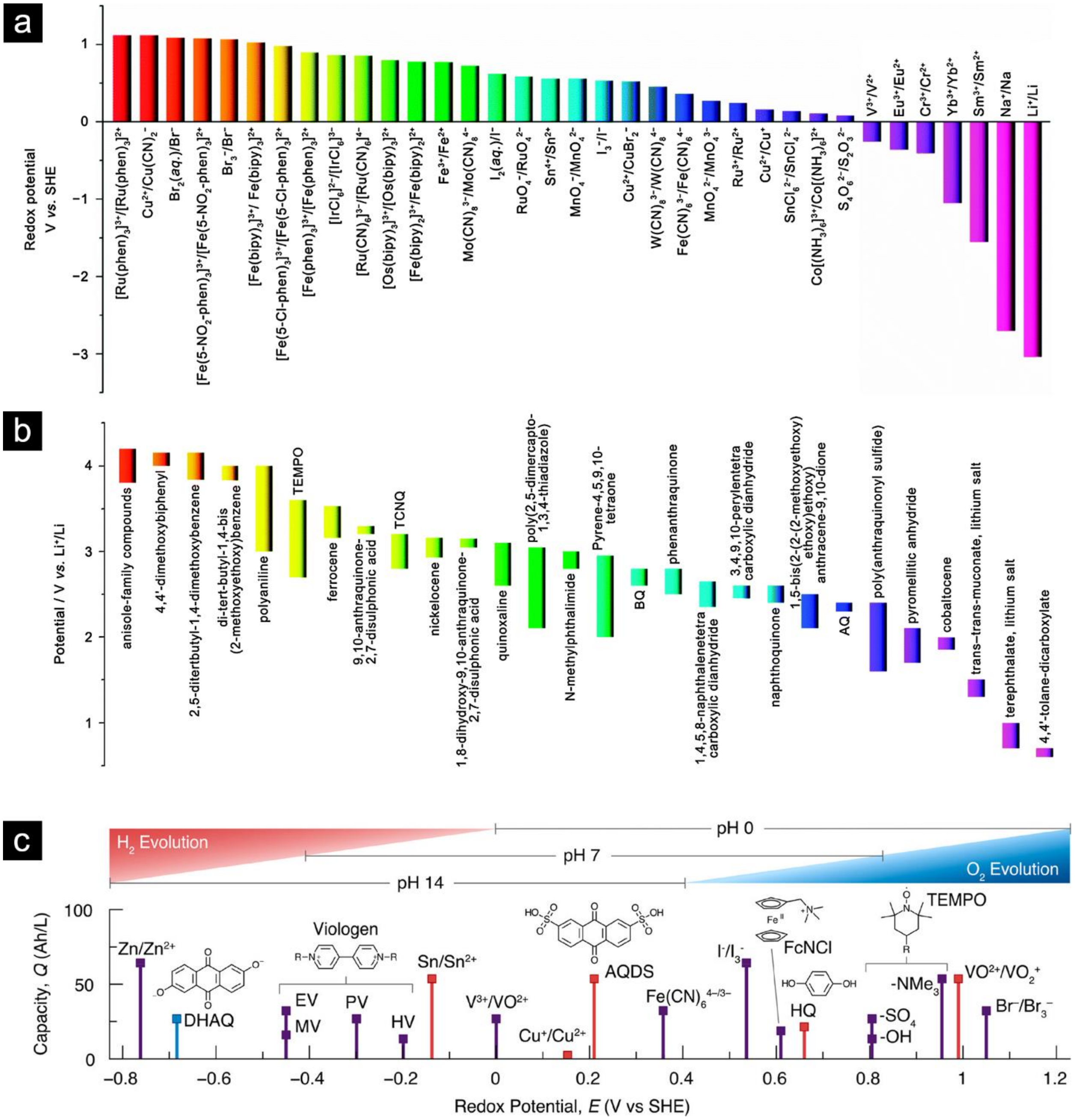

Figure 39. Redox potentials of redox electrolyte species. (a) Redox potential of various reversible redox couples suitable for constructing Li/Na-redox cells with aqueous/aprotic hybrid electrolyte system [194]; (b) Redox potential of representative redox-active organic and organometallic compounds with potential for organic-based Li/Na-redox cells [194]; (c) Redox potential of selected aqueous redox couples used in redox ECs, flow batteries, and redox batteries. The redox-active electrolytes illustrated in red, purple, and blue operate in acidic, neutral, or basic conditions, respectively [193]. (Reproduced with permission from ACS and RSC)

3.2.3 Remarks

Increasing the voltage of ECs from 2.7 V commercial level to match the voltage of LIBs is meaningful for practical applications in buffering batteries, which will eliminate the need for a converter. The optimization of the interplay between electrodes and electrolytes is essential to maximize the voltage of ECs. However, the voltage increase can come at a cost of power density and cycling stability. High values of viscosity and decreased ion mobility could increase the voltage but obviously, decrease the rate capability. Although this section discusses with a focus on materials aspects, the bipolar design is the most straightforward way for elevating the voltage limit by a factor of 2 or more at the cost of reducing the capacitance.

3.3 Towards extreme temperature operation

For extreme temperature performance, the electrolyte is the most critical component. At low temperatures, energy and power are limited by ionic conductivity of the electrolytes, while electrolyte decomposition causes safety and reliability issues at high temperatures. Therefore, kinetics-related parameters (such as ionic conductivity) and thermal stability properties are the main factors when evaluating electrolyte for extreme temperature operations.

The influence of temperature on electrolyte physicochemical properties is presented in Figure 40 [195]. A temperature change directly alters the ionic conductivity, viscosity and diffusion coefficient, and the latter two factors are highly relevant to ionic conductivity via different governing rules. All the variations are reflected by the capacitance and resistance. The intrinsic properties of an electrolyte, i.e. glass transition temperature (T_g) and decomposition temperature determine the usable temperature range, and T_g also influences ionic conductivity of particularly solid- or quasi-solid state electrolytes. The relation network should help scrutinize electrolyte options for ECs that target extreme working temperatures.

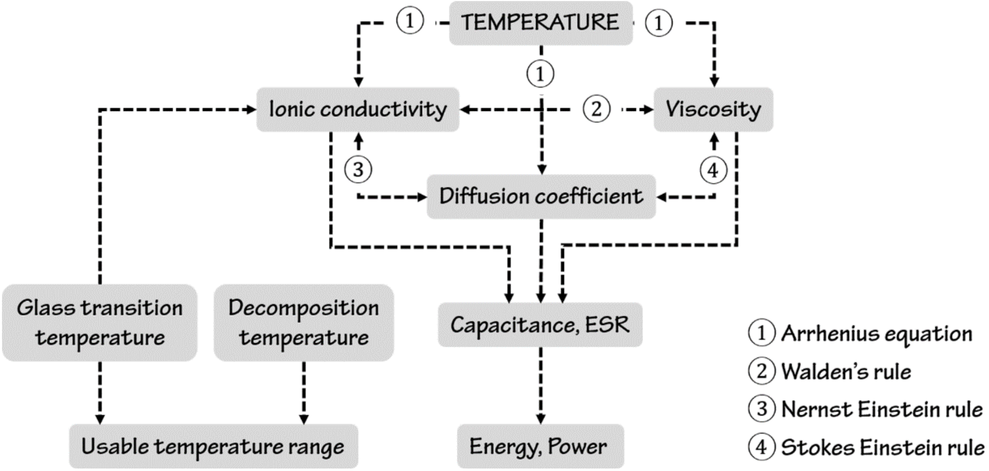

Figure 40. Relation network of temperature and different properties of electrolytes [195]. (Reproduced with permission from Springer)

3.3.1 Towards extreme low-temperature

3.3.1.1 Aqueous electrolyte systems for low-temperature operation

It is of industrial interest to develop low-temperature ECs based on aqueous electrolytes because of their low cost compared to other electrolytes. Aqueous electrolytes typically cease to work when the temperature below -10 °C, because most electrolytes start to freeze and the solubility of salts sharply decreases, which significantly diminishes ionic conductivity, although -52 °C was reported for RuO_2 pseudocapacitor using 39 wt% (5.26 M) H_2SO_4 without no additional treatment [196].

To extend the low-temperature limit, industrial anti-freeze (ethylene glycol, methanol or formamide) can be considered as an electrolyte additive that maintains a liquid phase at extremely low temperatures. An anti-freeze agent of ethylene glycol was added into Li_2SO_4 and achieved a limit of -20 °C for an EDLC [197]. The addition of the same agent into solutions of sodium, lithium, potassium and ammonium sulfate resulted in -30 °C aqueous electrolytes for a MnO_2/carbon pseudocapacitor, and it was found that the addition of ethylene glycol increases viscosity and decreases ionic conductivity [198], therefore alternative electrolyte systems have been developed. Methanol, an alternative to ethylene glycol, was used as an anti-freeze additive in a $NaClO_4$ electrolyte for AC based EDLCs, and a limit of -40 °C was achieved at an operation voltage window of 1.2 V [199]. Further, a 1.6 V window operating at -40 °C in 7:3 volume ratio water/methanol Li_2SO_4 system was reported demonstrating reasonable EDL behavior [200]. Also, formamide was also used as an anti-freeze agent, and an electrolyte of calcium chloride ($CaCl_2$) dissolved in formamide/water (1:1 volume ratio) was proposed as an electrolyte for down to -60 °C application in a CNTs-based EDLC system.

In general, the use of anti-freeze agents extends the low-temperature limit, but at the same time decreases the solubility of salts due to a low dielectric constant of the organic moiety promoting ionic association [201], resulting in low conductivity and impairing room temperature performance. For example, the solubility of Li_2SO_4 is reduced to around 0.7 M in water/methanol (7:3 volume ratio) mixture and the conductivity decreases to 40.6 mS cm^{-1} compared to 64 mS cm^{-1} for 1 M Li_2SO_4 in water at 24 °C, correspondingly capacitance drops from 103 to 89 F g^{-1} at room temperature for the mixture, and further to 68 F g^{-1} at -40 °C [200]. In an effort of searching highly conductive neutral (for high voltage operation) electrolytes that withstand freezing conditions, binary mixtures of 5 M cholinium chloride $[HOCH_2CH_2N(CH_3)_3]^+Cl^-$ water solution was demonstrated as a low-temperature electrolyte capable of working as low as -40 °C with a capacitance drop from 126 F g^{-1} at room temperature to 106 F g^{-1} at -40 °C [202].

3.3.1.2 Organic electrolyte systems for low-temperature operation

Many commercial ECs can already work reliably at a low-temperature of -40 °C based on AN based organic electrolytes. A further extension of the limit is restricted by similar concerns as for aqueous electrolytes, i.e. freezing point of the solvent, the solubility of salts and viscosity, etc. Accordingly, methods of extending the low-temperature limit of organic electrolytes include using low freezing/melting point solvent or use such chemicals as co-solvent and employing salts of high solubility to maintain adequate ionic conductivity and minimize the resistance at low temperatures [203-207].

Adding low melting point co-solvent (such as formates, esters, and cyclic esters) into the $TEABF_4$/AN electrolyte can enable carbon EDLCs to work at -75 °C but the limit is -55 °C with a moderate resistance value [203]. Interestingly, the study found that the capacitance value shows less dependency on the electrolyte variation, while ESR seems to be quite sensitive. By employing a zeolite-templated porous carbon as the electrode, a low-temperature limit of -70 °C was demonstrated in $SBPBF_4$ (spiro-(1, 1')-bipyrrolidinium tetrafluoroborate) in AN to show up to 86% of the energy density available at room temperature [206]. Note that the addition of co-solvents could limit the upper-temperature tolerance to 50 °C [208].

3.3.1.3 Ionic liquid electrolyte systems for low-temperature operation

Ionic liquids are well known for their high thermal stability that is suitable for high-temperature operations, however, ILs are restricted for low-temperature applications due to high viscosity, a melting point that is greater than 0 °C, and low conductivity. Strategies to enhance low-temperature performance includes mixing an IL with organic solvents [209-211] and mixing an IL with another IL [208, 212-215]. The former strategy improves ionic conductivity at a cost of thermal stability. Comparably, the eutectic mixture of ILs represents an important direction to obtain electrolytes with a very wide temperature range of operation.

Eutectic mixtures of ILs have a large stable liquidus temperature range (the span of temperatures between the freezing point and boiling point of a liquid). The size and symmetry of cations strongly influence the melting points of ILs. Usually, one of the two pairing ions (usually the cation) is particularly large and possesses a low degree of symmetry, leading to inefficient packing of the large irregular cations with small charge-delocalized anions, which is why organic salts have a reduced crystal lattice energy and hence a lower melting point compared to inorganic salts [212].

It was demonstrated that the selection of a proper mixture of cations prevents an ordered arrangement and crystallization, thereby inhibiting the formation of a lattice. The liquid state of the mixture can then be maintained several tens of °C lower compared to the mixture component IL taken individually [208]. A eutectic mixture of N-methyl-N-propylpiperidinium bis(fluorosulfonyl)imide ($PIP_{13}FSI$) and N-butyl-N-methylpyrrolidinium bis(fluorosulfonyl)imide ($PYR_{14}FSI$) was used as the EC electrolyte in conjunction with exohedral nanostructured carbon (CNTs and OLC) electrodes. The system exhibits a remarkable working temperature range from -50 to 100 °C as shown in Figure 41, with a liquid state maintained down to -80 °C [208]. Recently, a new eutectic IL mixture based on 1-ethyl-3-methylimidazolium bis(trifluoromethylsulfonyl)imide (EMImTFSI) and 1-propyl-3-methylpyrrolidinium bis(trifluoromethylsulfonyl)imide (PMPyrrTFSI) was developed and the low temperature limit has been lowered to -70 °C [216].

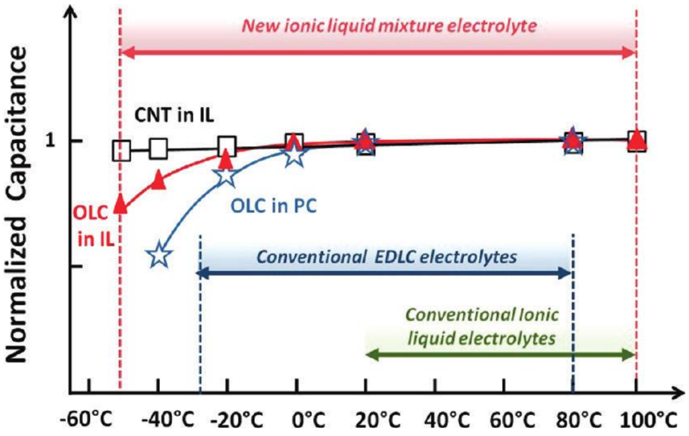

Figure 41. Change of capacitance versus the temperature for OLC and CNT electrodes in $PIP_{13}FSI$-$PYR_{14}FSI$ eutectic IL [208]. (Reproduced with permission from ACS)

3.3.1.4 Solid- or quasi-solid-state electrolyte systems for low-temperature operation

Solid- or quasi-solid-state electrolytes have an advantage in high package compatibility for leak-proof encapsulations and find applications in consumer electronics, microelectronics, and wearable or printable electronics. Application of this type of electrolytes for low-temperature operation is challenging, as their ionic conductivity is already moderate at room temperatures (at a level of 10^{-3} S cm^{-1}). There has been no comprehensive work addressing the low-temperature performance of solid-state electrolytes, but it was shown that the PVA/KOH based electrolyte is capable of working at -20 °C for a NiO-AC system [217].

Ionic conductivity in solid- and quasi-solid-state electrolytes is governed by the concentration of dissociated carrier ions and their mobility [195]. The mobility is highly relevant to the polymer matrix applied. Therefore, it could be beneficial to use low T_g polymers to facilitate ion movement.

3.3.2 Towards extreme high-temperature

3.3.2.1 Aqueous electrolyte systems for high-temperature operation

Limited by the water evaporation issue, aqueous electrolytes are not likely to be used at very high temperatures above 80 °C. Some research work demonstrated H_2SO_4 aqueous electrolyte can be operated at up to 73 °C at a 17% capacitance drop compared to room temperature [196]. The capacitance drop can be explained by the increasing thickness of the Helmholtz layer (increased charge separation distance) caused by accelerated Brownian motion [218].

Unfortunately, there seems to be no obvious solution from the materials development point of view to address the issue. Instead, one can apply thermal management (cooling) systems for aqueous EC packs to keep the temperature constant. However, this measure increases both size and cost and reduces energy density and reliability, and more importantly, it necessitates maintenance which is against the vision of IoT systems. Therefore, aqueous ECs are not recommended for high-temperature applications.

3.3.2.2 Organic electrolyte systems for high-temperature operation

The typical upper-temperature limit for organic electrolytes is 70 °C. Under extreme high-temperature operation, an organic electrolyte undergoes decomposition causing safety issues and impairing the cycling stability.

PC and AN based organic electrolytes are the most common among commercial products and in research reports. Comparably, PC are less thermally stable than AN (although in some cases PC based organic electrolytes are used up to 100 °C [219]). AN has a boiling point of only 80 °C and it is not recommended for temperatures above 70 °C due to safety concerns. In the event of abusive electrical, thermal, or mechanical conditions, a very toxic substance of hydrogen cyanide can be generated. AN also has a low flash point (5.6 °C), which also poses safety issues. In general, organic electrolytes are not suitable for extreme high-temperature applications, the same as aqueous ones.

3.3.2.3 Ionic liquid electrolyte systems for high-temperature operation

Ionic liquids are an important candidate for constructing ECs that can withstand extreme high-temperature conditions, due to their high decomposition temperature (typically 200 to 400 °C [220]). The thermal stability of ILs is influenced by water and impurities [221]. In principle, ILs can be used at an operating temperature below the decomposition point. However, at extremely high temperatures, the interaction between different components (electrode, binder, current collector and electrolyte) becomes predominant thus limiting operations under extreme conditions. Moreover, at high temperatures, the thermal expansion of components is not negligible. We have observed that the Swagelok cells (with stainless steel current collector and a Teflon jacket) are not suitable for high-temperature experiments, because of the mismatch in thermal expansion coefficients of different materials in the device. Likewise, the coin cell configuration is unsuitable since the pressure build-up at relatively high temperatures destroys the encapsulation, and the plastic gasket ring is not thermally stable. The above reasons may explain why a good amount of work exists demonstrating IL electrolytes working at temperatures from 60 to 80 °C, while it is rarely reported above 100 °C. To deepen the knowledge of the performance of IL above 100 °C, a special measurement set-up may be necessary.

In **Paper II**, a measurement setup for temperatures above 100 °C is custom-made and shown in Figure 42. The customized setup consists of a top and a bottom housing made of stainless steel. The housings provide one end connection to the EC cell from an external power supply. The second end connection is maintained by a flat head pin (made of stainless steel) through the top housing. A thin Teflon gasket is kept between the top housing and the flathead pin to avoid any connection with the rest of the housings. The EC cell is placed inside a cavity of the bottom housing. The cell is separated from the wall of the cavity by an inner Teflon body to make sure that the external connection through the housings is maintained only at the one side of the cell. A thin Teflon gasket on the surface of the bottom housing provides isolation for a piston-shaped current collector that is attached to the flat headpin with a stainless steel spring which could compensate thermal expansion issues at elevated temperatures.

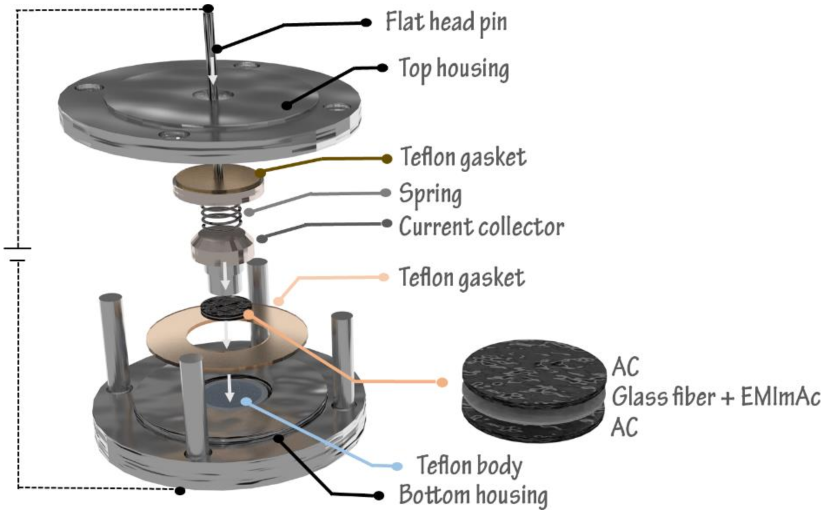

Figure 42. Schematic of the customized chamber and EC cell assembly (**Paper II**). (Reproduced with permission from Elsevier)

3.3.2.4 Trading Vmax for stability under extreme high-temperature operation

Although a high V_{max} results in a high energy density, it accelerates the aging process of ECs. An increase of the voltage window by 100 mV can reduce lifetime by a factor of two [222]. Charging to a voltage of 200 mV above the rated voltage can increase the ageing rate by a factor of 64, equivalent to increasing temperature by 40 °C above room temperature (25 °C) [223]. Therefore, it is not uncommon to lower the voltage limit to gain higher stability at high temperatures. Of particular practical significance, for neat ionic liquid electrolyte systems, this action can gain stability at no energy and power sacrifices.

With the measurement setup in Figure 42, an AC-based EDLC system with an ionic liquid electrolyte EMImAc was evaluated at up to 150 °C. Note that the selection of EMImAc as an electrolyte is mostly driven by the smart-MEMPHIS project which requires device assembly to be conducted in an uncontrolled environment and therefore the component (EMImAc) should be of low toxicity [224, 225] for staff safety. The maximum voltage limits V_{max} at different temperatures were determined by a series of CV measurements. At room temperature up to 80 °C, the limit is set at 1.5 V, while it is lowered to 1.4 V for 100 and 120 °C, and further down to 1.3 V when operating at 150 °C. The result of a thorough evaluation is listed in Table 7. Due to a high viscosity and low ionic conductivity of the neat IL EMImAc at room temperature, a large IR drop is observed leading to a usable voltage of 1.31 V. With an increased temperature, the ionic conductivity increases resulting in higher capacitance and at the same time a much smaller IR drop. As a result, the energy and power density are much greater at elevated temperatures than the ones obtained at RT with a higher V_{max}.

The above observation on EMImAc can be universal to other neat IL electrolyte systems. As high temperature greatly enhances the conductivity of neat ILs and therefore increases the effective voltage range during discharge, the energy and power loss as a result of decreasing V_{max} can be minimal. Neat ILs appear as very promising candidates for extreme high-temperature operations.

Table 7. Performance metrics of EMImAc containing EC (**Paper II**).

Temperature (°C)	$V_{\max}$ (V)	IR drop (mV)	Useable voltage (V)	Energy density (Wh kg^{-1})	Max. Power density (kW kg^{-1})	Capacitance (F g^{-1})
RT	1.5	186	1.31	4.3	4.6	84
40	1.5	79	1.42	6.1	12.8	98
80	1.5	35	1.46	8.3	30.5	122
100	1.4	29	1.37	7.3	32.5	121
120	1.4	26	1.37	7.4	36.0	121
150	1.3	23	1.28	7.7	35.6	142

3.3.2.5 Solid- or quasi-solid-state electrolyte systems for high-temperature operation

Compared to low-temperature applications, there is a great interest in using solid- or quasi-solid-state electrolytes at elevated temperatures. The accelerated ion diffusion rate in the electrolyte with less viscosity results in increased conductivity with increased operating temperature and gives a good energy storage capability. H_3PO_4 doped proton-conducting film poly[2,5 benzimidazole] (ABPBI) was evaluated up to 120 °C with AC electrodes, showing capacitance increased from 197 to 248 F g^{-1} from room temperature [226]. Similarly, a H_3PO_4-doped poly-[2, 20-m-phenylene-5, 50-bibenzimidazole] (PBI) electrolyte sandwiched between two rGO electrodes was demonstrated to have extremely high stability at up to 160 °C [227]. Record temperature of 200 °C was reported for an ionic liquid based ionogel [16, 78] and another ionic liquid infilled with clays [228]. For the most common PVA based electrolytes, the typical high-temperature limit is below 70 °C (T_g of PVA is 85 °C), and crosslinking of the PVA matrix may be beneficial in enhancing high-temperature performance [229].

3.3.3 Remarks

IoT systems such as wireless sensor networks with storage units are intended for a wide range of applications under diverse environmental conditions, but it is only in a very rare case that a specific application requires a range of temperatures from extremely low (-40 °C) to extremely high (200 °C), which can probably be tolerated only by eutectic ionic liquids without a thermal management system. Therefore, the design is mostly application-specified towards either low temperature or high temperature.

For extremely low-temperature applications, aqueous systems are advantageous because of relatively high conductivity and low cost. For extremely high-temperature, neat ILs are a good option, and trading voltage limit for stability can be considered. The benefit of gaining stability at little or no compromise in energy and power revealed in **Paper II** may also be observable for other room-temperature conductivity electrolytes such solid- or quasi-solid-state electrolytes. The use of neat ILs is also favored from a packaging point of view, as the absence of a solvent precludes an evaporation issue during a high-temperature encapsulation. Also, special encapsulation and package designs may be necessary for high-temperature ECs, taking into account the thermal expansion coefficient of the components.

This section addresses extreme temperature operation from the electrolyte options viewpoint, however, the consideration of electrodes, separators, current collectors and their interaction with electrolytes may not be trivial either.

3.4 Towards slow self-discharge and low leakage current

Self-discharge and leakage current are detrimental to preserving the harvested energy in a self-powered system. Especially in miniaturized systems where the magnitude of the current (converted from the harvested energy) for charging an EC is at as low as μA or even at the nA level. Self-discharge dissipates energy through a spontaneous voltage decay under open-circuit conditions, while the leakage current is related to a continuous energy loss when keeping the EC at a constant voltage (e.g. for buffering battery applications) and also determining the charging behavior at low current. Minimizing self-discharge and leakage current is a critical task for EC development targeting IoT applications.

3.4.1 Mechanisms

An ideally polarized capacitor has no pathway for current to leak in an open circuit, and the equivalent circuit can be represented by Figure 43a, in which the charging current i_t enters through a resistance R_S into the capacitor C. For a constant applied voltage V, the time-dependent charging current can be calculated as

$$i_t = i_i \exp(-\frac{t}{R_S C}) \qquad \text{Equation 53}$$

where i_i is the initial current at t = 0. In reality, self-discharge and/or leakage current will set in, and the equivalent circuit contains a potential- and time-dependent leakage resistance, R_{SD}, in parallel to the capacitor [230]. Under constant voltage charging, it is decomposed to i_C that charges the capacitor and the leakage current, i_{SD}, resulting from the self-discharge through R_{SD}. When $R_{SD} >> R_S$, self-discharge is slow and the charging current is close to that charging an ideal capacitor as in Equation 53. If $R_{SD} << R_S$, the rate of self-discharge is high and a large leakage current is required to maintain charge stored in the capacitor to sustain a constant voltage.

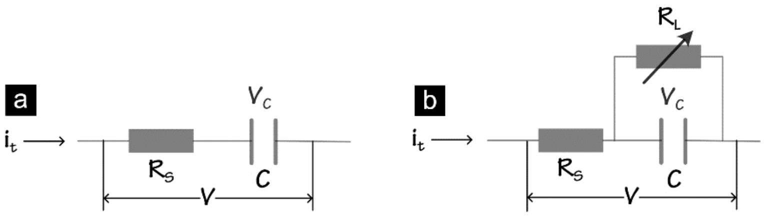

Figure 43. Equivalent circuits of ECs (a) without and (b) with self-discharge / leakage current [230].

When the circuit is charged to voltage V and then left in open-circuit, the capacitor discharges through R_{SD}, where the self-discharge process takes place. The identified self-discharge mechanisms are:

(1) *Activation-controlled Faradaic reaction*, which kinetically follows the Tafel equation. This corresponds to overcharging beyond the respective (plus or minus potential) decomposition limit of the electrolyte. The voltage decay as a function of time is mathematically represented as [27]

$$V = V_0 - \frac{RT}{\alpha F}\ln(\frac{\alpha F i_0}{RTC}) - \frac{RT}{\alpha F}\ln(t + \frac{C\tau}{i_0}) \qquad \text{Equation 54}$$

where V is the voltage at time t, R is the gas constant, T is the temperature, F is Faradaic constant, α is transfer coefficient, i_0 is the exchange current density, C is the capacitance and τ is an integration constant. Therefore, voltage declines linearly with $\log t$.

(2) *Discharge through ohmic resistance*, physically corresponding to any undesired imperfection of insulating material, e.g. short-circuit leakage currents between adjacent electrodes in imperfectly sealed bipolar configurations. In this case, voltage decay is in the mathematical form of [27]

$$\mathrm{V} = V_0 \exp(-\frac{t}{RC}) \qquad \text{Equation 55}$$

where V_0 is the initial voltage, R is the leakage resistance. Therefore, $\ln V$ declines linearly with t.

(3) *Diffusion-controlled processes*, which can take place in the case of e.g. the concentration of reactants for a redox reaction is very low. The dynamics of voltage decay is governed by Fick's law and in the mathematical form of [27]

$$V = V_0 - 2zFAC^{-1}D^{1/2}\pi^{1/2}c_0 t^{1/2} \qquad \text{Equation 56}$$

where A is the area of flux, D is the diffusion coefficient and c_0 is the initial concentration of the diffusive species. Therefore, V declines linearly with $t^{1/2}$. The pattern of the voltage decay as a function of time is generally used to detect the mechanism of self-discharge.

(4) *Charge-redistribution*, which is a phenomenon prominent in porous electrodes [231, 232]. Graphically, charge redistribution within one slit pore is displayed in Figure 44a, where the charge is first accumulated at the pore "mouth" and distributed down to the pore base gradually. To simulate the charge redistribution effect in porous carbon structures, the transmission line model (TLM, different RC sub-systems forming a ladder-like circuit) as shown in Figure 44a can be employed. Each R_iC_i system has its characteristic time τ_i (not necessarily equal to another time constant τ_j), at which it may be charged or discharged. The circuit is proposed to be universal for any porous electrode having non-branching pores [232]. Due to different time constants, the system cannot be charged synchronously, implying that smaller τ_i of RC circuit are firstly charged up and then the charge is redistributed throughout, causing the apparent voltage decay, i.e. self-discharge.

It was proven that charge redistribution leads to the same mathematical expression of voltage decay as activation controlled Faradaic reactions [231], in the form of

$$V = V_0 - a\ln(t + b) \qquad \text{Equation 57}$$

where a and b are constants.

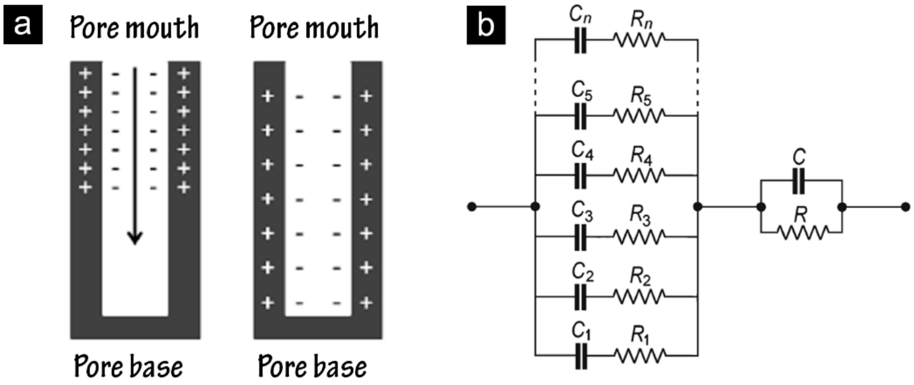

Figure 44. (a) Charge redistribution in a slit pore; (b) Vertical ladder network of TLM [232]. (Reproduced with permission from Springer)

Except for the above classic mechanisms, different theories were claimed throughout self-discharge mechanism research and accepted in recent studies. These theories include, for example, divided potential driven self-discharge [233]. Nevertheless, these theories leading to the voltage decay expression taking similar forms of Equations 54-57.

3.4.2 Mathematical treatments

Several ways of the mathematical treatment of self-discharge curves can be found in the literature. Qualitatively, the governing equations indicate different patterns of voltage decay as a function of time. The linear pattern of different mechanisms is summarized in Table 8.

Table 8. Summary of self-discharge mechanisms and the voltage decay relation with time

Self-discharge mechanism	Voltage linear relation with time
Activation controlled Faradic process or Charge redistribution	V *vs.* $\ln(t + \theta)$ where θ is a term involving integration constant
Diffusion-controlled process due to impurities	V *vs.* $t^{1/2}$
Ohmic leakage	$\ln(V)$ *vs.* t

In some reports, the self-discharge curve is divided into several sections by time, and under each time domain, a single self-discharge model is applied. As shown in Figure 45b, researchers claim the rapid voltage decay is caused by a diffusion-controlled process (region 1), while in the intermediate time region, the process is governed by a divided potential driven process (DPD, region 2) and subsequently a single potential driven process (SPD, region 3). Plotting the voltage-time relationship as $\ln(V)$ vs. $t^{0.5}$ as in Figure 45c (a method claimed to be suitable for self-discharge without involving Faradaic reactions [234]) the self-discharge curve is divided into two sections, with the first section fitted with a diffusion-controlled model, and the second is fitted with an ohmic leakage model [233, 234].

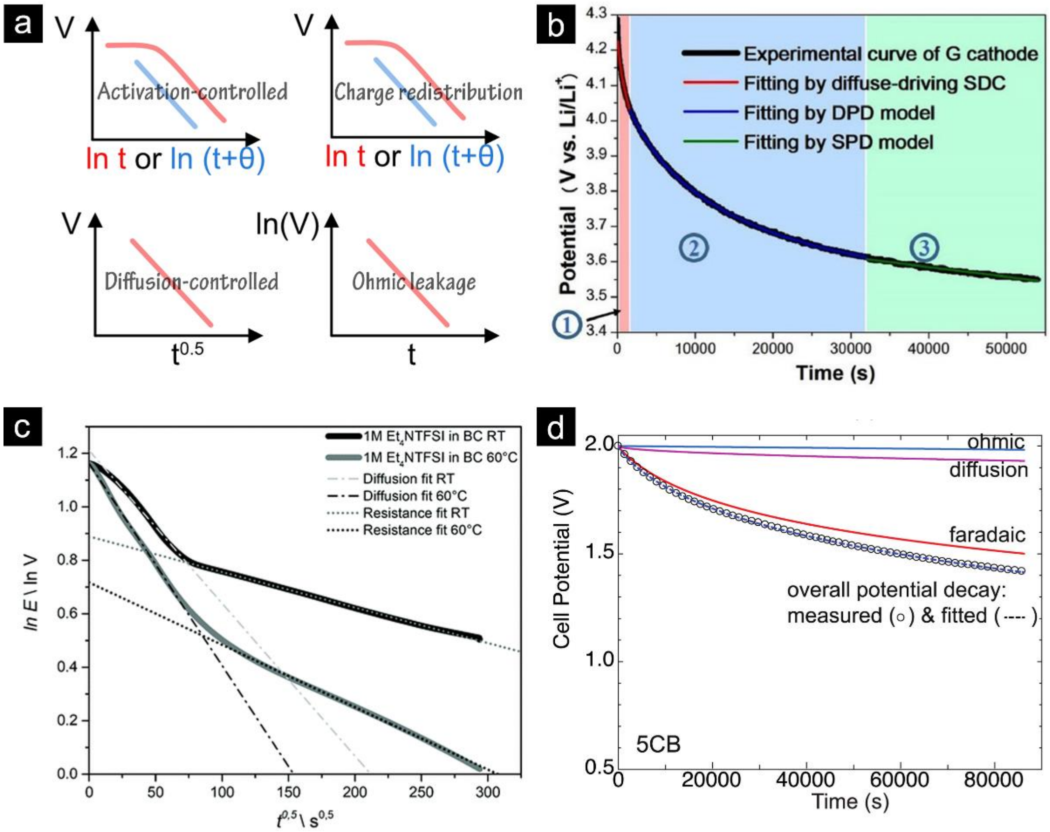

Figure 45. Examples of the self-discharge curve mathematical treatment. (a) Qualitative analyses of voltage decay pattern. Depending on the logarithm argument, the activation-controlled and charge redistribution mechanisms show a linear voltage decay (blue curve) or linear decay following a plateau (red curve); (b) Self-discharge curve is divided into three parts and treated separately with diffusion-controlled (region 1), divided-potential-driven (DPD, region 2) and single potential driven (SPD region 3) models [235]; (c) Self-discharge curve is plotted as ln(V) vs. $t^{0.5}$, and divided into two parts, the initial part is diffusion-controlled and the second part follows the pattern of ohmic leakage [234]; (d) Self-discharge curve is fitted with Equation 58, with different mechanisms identified simultaneously [236]. (b - d Reproduced with permission from Elsevier and RSC)

The curve fitting taking into account the whole self-discharge curve can be done by combining all the different expression forms

$$V(t) = V_0 \exp\left(-\frac{t}{a}\right) - b\sqrt{t} - c - d\ln(t+e) \qquad \text{Equation 58}$$

where a - e are all constants (e.g. in Figure 45d).

3.4.3 Influence of charging history and temperature

The charging history and ambient temperature significantly influence the rate of self-discharge and leakage current [237]. Applying a small $V_{\max}$ and charging current, and holding the voltage for a long time at a low temperature will lead to minimal self-discharge and leakage current.

The observation for porous carbon-based ECs can be understood by the charge redistribution model. Bearing in mind the role of pores with different sizes, bigger pores at the periphery adsorb/de-adsorb ions at a faster rate than meso- and micropores due to the higher resistance of the latter. Upon charging at high current for a short period, ions accumulate at the big pores and the small pores remain unoccupied. A charge redistribution process will then set in so that the meso- and micropores reach an equilibrium potential with the big pores, and a rapid voltage decay will be observed. However, if the EC is charged for a long time before being open-circuited, the ions reach the micropores of the electrode, and this sudden voltage drop can be averted. The time constant of charge redistribution for porous carbon-based ECs can be more than 50 hours [231]. A low charging current will allow more time for ion distribution into small pores, which in turn will alleviate the fast voltage decay.

Regarding temperature, the Arrhenius equation is used to model its relation with self-discharge current I, in connection to leakage current, and temperature T [27]

$$I(T) = A\exp(-\frac{\Delta E_a}{RT}) \qquad \text{Equation 59}$$

where ΔE_a is in the order of 40-80 kJ mol^{-1} for Faradaic processes, and 16-20 kJ mol^{-1} for diffusion-controlled processes. Assume an ΔE_a of 40 kJ mol^{-1}, the leakage current is 37 times higher at 70 °C than at 0 °C.

3.4.4 Strategies of suppressing self-discharge and leakage current

Similar to batteries, a charged EC is at a relatively high free energy state compared to its discharged state, therefore the phenomenon of self-discharge and leakage current is thermodynamically driven. It cannot be prohibited but the process can be kinetically slowed down to a certain degree until meeting application requirements.

To reduce self-discharge and leakage current, modification of all the components of the SC were reported: electrodes, electrolyte, separator, and current collectors. To find a solution, one can first identify the mechanism based on the mathematical simulation discussed in section 3.4.1. It is advised to employ three-electrode systems to identify the individual behavior of the two electrodes [27, 238]. This procedure is useful if there are different mechanisms or rates of self-discharge at the positive and negative electrodes, which is usually the case. For example, Chen and co-workers [239] used this method and identified that in a hydroquinone/H_2SO_4 redox electrolyte system, self-discharge takes place through a shuttle transport of redox species BQ (*p*-benzoquinone) between the two electrodes. Accordingly, remedies including using an ion-exchange membrane Nafion® 117 as a separator to block the diffusion pathway of BQ, or selecting a redox electrolyte which is converted into insoluble species during a charging process. Besides, Tevi et al. [240] proposed to deposit an ultra-thin layer of poly(p-phenylene oxide) (PPO) to block electron transfer to prevent reactions related to redox-active impurities of the electrode or electrolyte. Adding electrolyte additives such as surfactants of sodium dodecyl sulfate (SDS) and p-t-octylophenol (Triton X-100) [241] has also been reported to be effective solutions in suppressing self-discharge. Recently, separator modification to shift the zeta potential for a negative surface charge [242], and new solid-state electrolytes [243, 244] confining the movement of ions are developed for suppressing self-discharge.

As the general strategy is to create a "barrier" for ion diffusion or charge redistribution, the reduction of self-discharge usually comes at a cost of power rate capability, capacitance or cycle life. For example, the influence of alumina coated electrodes for suppressing leakage current was studied theoretically and experimentally, demonstrating that a 0.5 nm Al_2O_3 coating may reduce the rate of the faradic reactions by 17% and the leakage current by 77.73%. However, the specific capacitance of the electrical double layer may decrease by 45.35% [245]. A method that improves self-discharge and leakage current properties with minimal compromise in other performance characteristics is of high significance. So far, the electrolyte additive approach, with the Triton X-100 [241] or with liquid crystals has been proven successful in this regard.

3.4.5 Liquid crystal as an electrolyte additive

Liquid crystals (LCs) are thermodynamically stable phases characterized by long-range orientational order and various degrees of positional order of the building blocks (mesogens). LCs combine the fluidity of liquids with anisotropy (optical, mechanical, electrical, and magnetic) typical of crystals. The simplest LC phase (nematic) is a 3-dimensional anisotropic liquid characterized by a long-range orientational order

The material 5CB is a well-studied commercial thermotropic (the order is determined by temperature) LC with robust electrochemical stability. It is composed of two phenyl aromatic rings terminated by a CN (cyanonitrile) head group at one end and a 5 membered alkyl chain (pentyl) at the other end. It is part of the nCB family (n is the number of members in the alkyl chain). Generally, the alkyl chain determines the melting point, introduces flexibility, and controls the stable alignment of the LC phase [246]. The nematic phase of 5CB exists below the nematic to the isotropic phase transition temperature, which is at 308.5 K, around 35 °C [247].

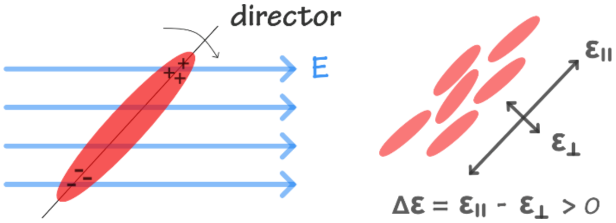

Figure 46. Schematic of positive anisotropy

5CB has a positive dielectric anisotropy (Figure 46) $\Delta\varepsilon = \varepsilon_{||} - \varepsilon_{\perp} > 0$, where $\varepsilon_{||}$ and $\varepsilon_{\perp}$ are the dielectric permittivities measured along and normal to the director, respectively. Upon applying an electric field, the dielectric torque wants the director to become parallel to the electric field with a characteristic response time on the order of milliseconds [248, 249]. As the shear viscosity of a nematic layer depends on the LC director orientation, the effective viscosity of the nematic fluid can increase significantly during the process [247, 250]. This is an example of an electrorheological effect (ER) [250].

A significant reduction of the self-discharge and leakage current in an EC has been demonstrated when adding 2% of 5CB to an organic electrolyte (TEMABF$_4$/AN) [236]. The researchers attributed the effect of the added liquid crystal in terms of electrorheology (Figure 47). The LC-additive was proposed to be gathered in the vicinity of the electrode surface, and the field-induced reorientation of the LC in the double layer would make the effective conductivity of the electrolyte-LC system strongly voltage-dependent [236]. The electrorheological effect [247, 250] should hereby decrease the ionic conductivity of the electrolyte, and accordingly, the self-discharge of the SC.

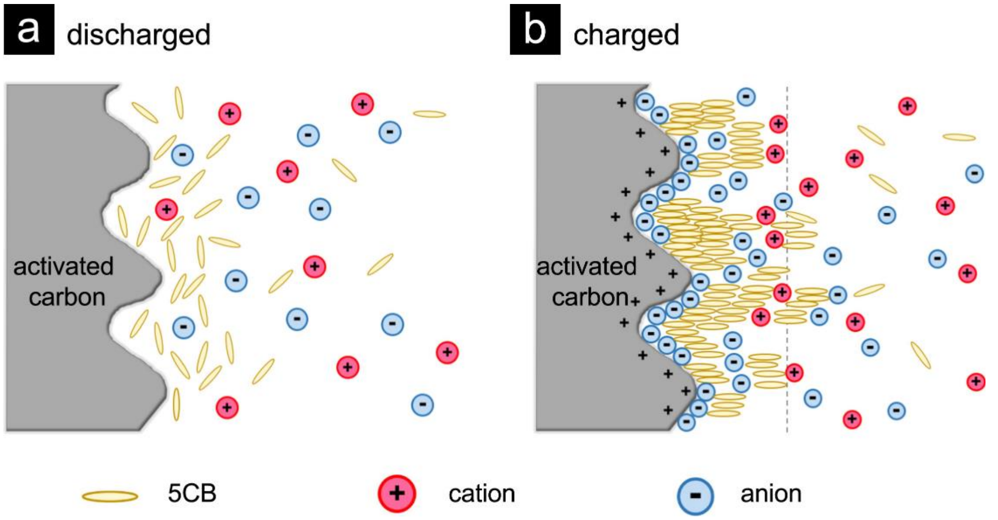

Figure 47. Mechanism of suppressing self-discharge with 5CB in an electrolyte [236]. (a) At discharged state, the cations, anions and 5CB molecules in the electrolyte are distributed evenly. (b) When the electrode is charged, the electric field near the electrode surface causes 5CB molecules to align towards the field and enhances flow viscosity. (Reproduced with permission from Elsevier)

Paper V investigated 5CB as an electrolyte additive in the aqueous electrolyte Li$_2$SO$_4$ in AC//AC symmetric system. It was found that the self-discharge and leakage current was decreased at all operating voltages in the study – a comparison at 1.3 V is shown in Figure 48. The energy density and power density remain almost unchanged for the 5CB-containing device (Table 9).

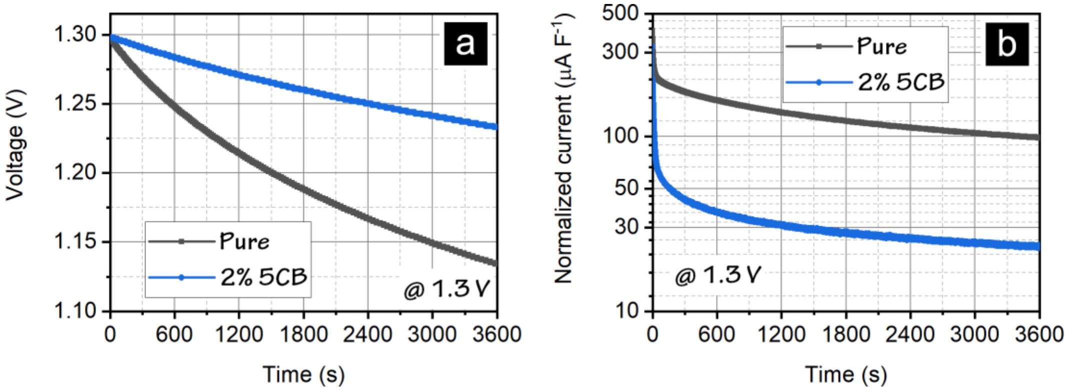

Figure 48. (a) Self-discharge and (b) leakage current comparison at 1.3 V for the pure Li$_2$SO$_4$ and the one with 5CB additive (**Paper V**). (Reproduced with permission from Elsevier)

Table 9. Energy density, power density, and leakage energy at a different voltage. (**Paper V**)

	Li_2SO_4		Li_2SO_4/5CB	
Voltage (V)	Energy density (Wh kg^{-1})	Power density (W kg^{-1})	Energy density (Wh kg^{-1})	Power density (W kg^{-1})
1	3.8	25	3.8	25
1.2	5.7	30	5.6	30
1.3	6.8	32	6.7	32
1.4	8.0	35	7.9	35
1.5	9.3	37	9.2	37
1.6	10.9	40	10.7	40

The impedances of the 5CB-free and 5CB-containing devices were compared in Figure 49. Interestingly, the semicircle of the 5CB-containing device is found to be voltage-dependent while the 5CB-free device has a much more constant semicircle (slightly reduced at high voltage). The voltage dependency is usually found in Faradaic systems, however, herein it is assumed no obvious Faradaic reaction would happen except when approaching the stability window of the device 1.6 V, and the semicircle is assigned to be an interfacial resistance between the electrode interface and electrolyte. The increased resistance for the semicircle may be due to the presence of 5CB which at higher voltages increases the solution resistivity at the interface.

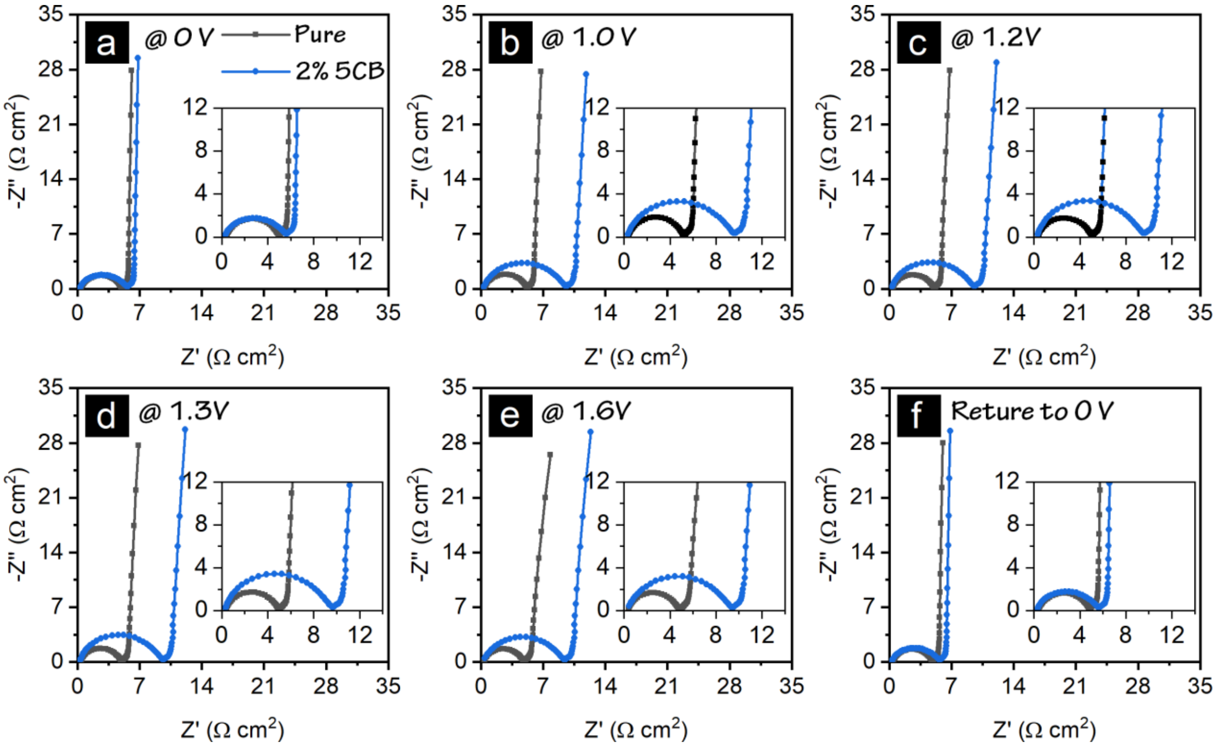

Figure 49. Nyquist plots at different d.c. voltages for 5CB-free and 5CB-containing devices with 1 M Li_2SO_4 electrolyte (**Paper V**). (a) 0 V; (b) 1 V; (c) 1.2 V; (d) 1.3 V; (e) 1.6 V; (f) return to 0 V after charging to 1.6 V. (Reproduced with permission from Elsevier)

At the moment, it can only be speculated that a similar effect occurs in this system as claimed in the previous 5CB-containing system study, Figure 47 [236], i.e. the orientation of 5CB increases the local viscosity being a barrier for absorbed ions diffusing back to the bulk electrolyte. Yet how the reorientation of the LCs decreases the conductivity is still not clear from a physics point of view. The ionic conductivity in a nematic LC is normally larger along with the director than perpendicular to it [247], which seems to contradict the picture that field-induced reorientation of the director into the field direction should decrease the conductivity. It should also be pointed out that the porous carbon electrodes are not flat. Instead, they have pores, valleys, and hills with characteristic dimensions from nanometers up to several micrometers. Hence, close to the electrodes, the LC director field is probably significantly non-uniform and might even contain topological defects. It is not clear whether these topological defects and their response to electric fields could have an impact on the field controlled effective conductivity. Further mechanistic study is needed to elucidate the mechanism.

3.4.6 Remarks

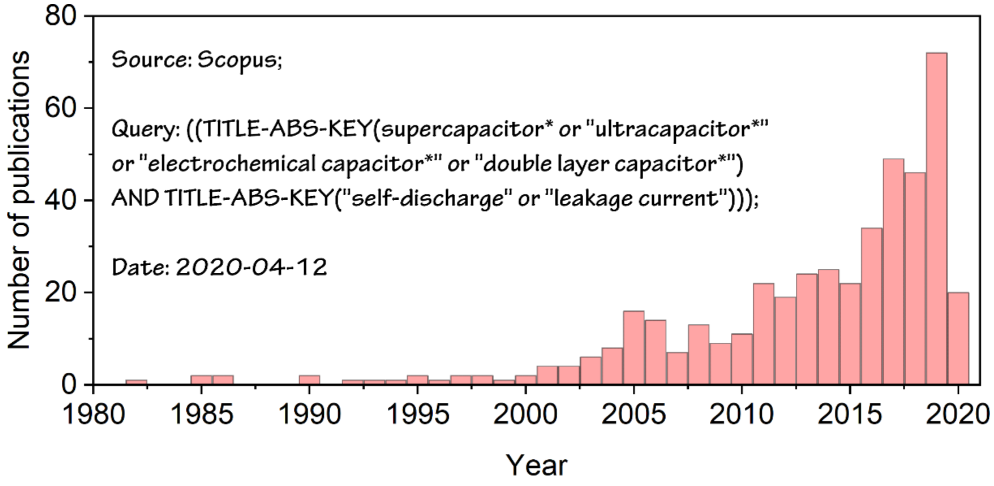

Figure 50. The number of publications reporting self-discharge and leakage current of ECs.

The number of publications reporting self-discharge and leakage current of ECs keeps growing, a substantial increase in the year 2019 can be found. Indeed, minimizing the loss through self-discharge and leakage current is essential for a practical application. From materials and devices development point of view, the solutions differ from one system to another, with respect to different mechanisms, but it seems most of the measures proven effective would inhibit kinetics of ion movement and therefore would decrease power performance, except with a few exceptions. The relation between charging history, temperature and self-discharge rate may help to design PMUs that operate the EC in a favorable way for low losses, i.e. applying low current charging and voltage holding at low temperatures. Another engineering method is through a bipolar design, in which individual EC units take low voltage distribution on them, thereby achieving low self-discharge while retaining all the other merits of ECs. Yet again, high-level manufacturing control conditions are desirable to minimize the negative effects of non-uniformity of the constituting units.

The mathematical treatments are mostly qualitative and semi-quantitative in terms of mechanism analysis. Due to the same form of voltage decay for an activation-controlled process and charge redistribution, distinguishing the two mechanisms is difficult. It is demanding but indispensable to carefully design experiments so that different characterization techniques can be combined to corroborate the mathematical modeling interpretation. Moreover, the electrode history must be taken into account for comparing self-discharge of materials in the literature where slight differences in charging procedures might significantly impact the observed self-discharge [251].

3.5 Towards improved high-frequency performance

3.5.1 Capacitor metrics concerning high-frequency response properties

Every capacitor has a “comfortable” frequency range to work properly, otherwise, the behavior deviates from capacitive features and the device transforms from a capacitor to a resistor if being charged/discharged at an overrated current. The work towards high-frequency EC is driven by the need for system size reduction for IoT systems, where a suitable EC could substitute conventional bulky electrolytic capacitors for line filtering and smoothing ripples on a rectified wave. A high-frequency EC as a storage unit is also believed to be better able to absorb the energy pulse from an energy harvester in the self-powered systems [252].

A capacitive behavior of a capacitor implies that current leads voltage by 90° in an a.c. circuit. Due to the nature of the device structure and the working mechanisms, conventional capacitors, i.e. electrostatic capacitors and electrolytic capacitors, can perform as ideal capacitors (phase angle close to -90°) at high frequencies up to the order of 10^7 and 10^4 Hz, respectively. In contrast, common ECs are in a range from a low frequency to 10^{-1} or 10 Hz, depending on the size and material used. The development of high-frequency ECs is intended to increase the operating frequency to a substantial value, hopefully to a kHz level, with EDL mechanism unchanged for a higher energy density than in conventional capacitors.

The laboratory technique to evaluate the frequency range is through an EIS measurement, and a phase angle variation against frequency can be obtained. The frequency at which the phase angle is -45° is a characteristic frequency, also called cut-off frequency f_0. At operation frequencies beyond f_0, the resistive behavior starts to dominate. The reciprocal of f_0 is the relaxation time constant τ_0, i.e. the *RC* time constant in relation to charging a series RC circuit. This is an indicator of how quickly an EC can be charged or discharged. For electrostatic capacitors, τ_0 is generally below 1 μs, and for electrolytic capacitors, the *RC* product is generally < 1 ms. An ideal capacitor discharges about 63% of its energy during one *RC* time constant. Another figure of merit is the phase angle at 120 Hz, φ_{120Hz}. For a.c. line filtering purposes, φ_{120Hz} is normally used for comparison in performances of smoothing ripples of 60 Hz (U.S. city power line frequency) a.c. after a full-wave rectification.

3.5.2 Design guidelines of high-frequency ECs

The understanding of the transmission line model from the vertical ladder RC circuits in Figure 44b should provide insights into designing ECs with excellent frequency response properties. The reason that conventional ECs with a porous carbon electrode has low f_0 is asynchronous charging. The rich porosity leads to a distribution of the ionic resistance network, corresponding to different branches of the ladder circuit, with each of them having a different RC time constant. Therefore, charge redistribution takes place through different time domains. The resistance of micropores is high and it can take a long time to reach a fully charged state [231]. If the pores of the electrodes are uniform in size and shape, the ladder network can be modeled as a single branch RC circuit as in Figure 43a. In this way, the EC is charged in a synchronous manner. Further, if the equivalent resistance R is substantially small, together with a moderate capacitance, the RC product (i.e. time constant τ_0) could reach down to the order of milliseconds, in contrast to seconds for common ECs with porous carbon electrodes.

Based on the discussion above, an ideal electrode material should be of high electronic conductivity with an optimal porosity. The latter implies that the pores are preferably well-connected and relatively large in diameter. Micropores, dead pores and tortuous pore geometry should be avoided. Moreover, the resistance is a result of an optimized combination of the electrodes, electrolytes and current collectors, therefore, the contact between the components should also be optimal.

In terms of applications in miniaturized systems, the footprint or space allocated for an EC component is limited. This indicates that instead of specific capacitance in Farads per gram, the areal and volumetric capacitance should be examined. Thus, the electrode fabrication is preferably to be scalable in terms of mass loading or thickness, with little compromise in the frequency response property.

3.5.3 Carbon-based high-frequency ECs

The first report on high-frequency ECs was published in 2010 with graphene as an electrode material [13]. Graphene is a compelling material for such an application because of the extremely high electronic conductivity and a pore-less structure. The monolayer or few-layer graphene-based devices have shown good frequency response [253], but the extremely low mass loading severely limits the energy content (per footprint) of such devices: a basal plane produces only 3 $\mu F\ cm^{-2}$, estimated from a polished graphite electrode in NaF electrolyte [254] or 21 $\mu F\ cm^{-2}$ for a 0.3 nm thick graphene layer in $BMImPF_6$ electrolyte [254]. The low areal capacitance is generally a common concern for many nm-layered devices. Although high metrics can be calculated based on the ultrathin layer device, the true performance may not be the same as ultrathin layer devices when scaling up to achieve a desired areal device capacitance [51]. Vertically aligned graphene sheets [13] enable the utilization of edge planes which have a greater areal capacitance of 50 to 70 $\mu F\ cm^{-2}$ [254], and therefore a decent capacitance of 0.4 $mF\ cm^{-2}$ at 0.01 Hz was achieved, though the capacitance is still less than 0.2 $mF\ cm^{-2}$ at 120 Hz.

A recent review [252] compiled the materials development of high-frequency ECs. The materials option has expanded over nearly all carbon allotropes, and further to some of the pseudocapacitive oxides and conducting polymers. As one can find, increasing areal capacitance remains a challenge to overcome. Most devices rely on thin-film electrodes for a high-frequency response property. For example, by reducing a CNT film thickness to nm scale, a cut-off frequency of nearly 16 kHz can be obtained, while the areal capacitance is as low as 58 μF cm^{-2} [255]. By increasing the film thickness and mass loading to a proper extent, a higher capacitance can be obtained, however at a certain degree of compromise in frequency response. For instance, a 0.28 mF cm^{-2} EC with 1995 Hz cut-off frequency was demonstrated for a 298 nm thick CNT film on gold-coated Al foil with a vacuum filtration method [255], and a 0.6 mF cm^{-2} device with 1425 Hz cut-off frequency was fabricated with CNT film pressed on gold-coated roughened stainless steel rods [256].

A hybrid structure of graphene/VACNTs can potentially solve the problems associated with their constituting material components. Integrating VACNTs with graphene could increase the areal capacitance of the latter, and graphene as the substrate for VACNTs could be a solution to replace metal layers. The hybrid formation mechanism is preferred to be chemical bonding rather than a mere physical mixture, to reduce the contact resistance. A hybrid structure between graphene and VACNTs was investigated by Tour's group [257], and an MSC (on a rigid Si substrate) based on this hybrid material was demonstrated exhibiting 1343 Hz cut-off frequency, -81.5° phase angle, 0.23 mF cm^{-2} capacitance at 120 Hz for a 10 μm VACNTs device. The performance is encouraging but this graphene/VACNTs hybrid material requires chemically active copper or nickel metal underlayers for growing single-layer graphene. Moreover, the areal capacitance could be further enhanced.

In **Paper III**, we demonstrate a graphite/VACNTs hybrid material as an electrode with high areal capacitance (1.38 mF cm^{-2}) and volumetric capacitance (345 mF cm^{-3}) at 120 Hz, with phase angle around -85°. This represents the state-of-art performance of high-frequency ECs (Table 10).

The material was fabricated through chemical vapor deposition of CNTs on a highly oriented graphite film with a plasma treatment to introduce oxygen groups for hydrophilicity with an aqueous 6 M KOH electrolyte. The material has great flexibility (Figure 51a) and roughly 40 μm long CNTs vertically aligned on the substrate (Figure 51b). The length of the CNTs is longer than those reported previously [258], which enables a high capacitance (Figure 51d) due to high mass loading, and encouragingly superior frequency response with a cut-off frequency of 1.9 kHz and phase angle of -84.82° at 120 Hz (Figure 51c). The connection between CNTs and the graphite substrate was examined. There is a sign from TEM observations that the CNTs are covalently bonded to the graphite substrate, which optimizes the contact between active electrodes (CNT array) and the current collector (graphite paper).

Table 10. Comparison of high-frequency ECs (**Paper III**).

Material	Electrolyte, Voltage	$\phi_{120\ \mathrm{Hz}}$ (°)	f_0 (Hz)	τ_0 (ms)	$C_{A,\ 120\ \mathrm{Hz}}$ (mF cm^{-2})	$C_{V\text{-}e,\ 120\ \mathrm{Hz}}$ [a] (mF cm^{-3})	$C_{V\text{-}d,\ 120\ \mathrm{Hz}}$ [b] (mF cm^{-3})	Ref.
VACNTs on graphite	**KOH, 0.8 V**	**-84.82**	**1980**	**0.51**	**1.38**	**690**	**345**	**Paper III**
SWCNTs	H_2SO_4, 1.0 V	-81	1425	0.7	0.601	13065	-	[256]
SWCNTs	TEA BF_4, 2.5 V	-82.2	1995	0.501	0.282	4732	69.3	[255]
Graphitic carbon / CNT	TEA BF_4, 2.5 V	-80.3	1000	1	0.3	3947	72.4	[259]
Carbon nanofiber	KOH, 0.9 V	81 [c]	1300	0.77 [c]	2.25	187.5	-	[260]
VOGN [d]	KOH, 1 V	-82	15000	0.06	0.175	1458	24.3	[13]
VOGN [d]	KOH, 0.9 V	-83	10000	0.1	0.3	150	-	[261]
VOGN [d]	KOH, 0.9 V	-82	4000	0.248	0.36	-	7.5	[262]
VOGN [d]	KOH, -	-85	6300	0.16 [c]	0.265	-	17.2	[263]
Holey graphene	KOH, 0.8 V	-81.2	1220	0.819	0.478	1200	-	[264]
rGO	KOH, 0.8 V	-84	4167 [c]	0.24	0.283	70	6.4	[265]
Ketjen black	TEA BF_4, 2.8 V	-79.8	1000	1	0.574	3679	137.8	[266]

[a] $C_{V\text{-}e}$ is the volumetric capacitance considering only electrode thickness, and $C_{V\text{-}d}$ is volumetric capacitance considering electrode and current collector thicknesses. Estimated/inferred from the presented data. [c] Estimated or derived from the presented data. [d] VOGN stands for vertically oriented graphene nanosheets.

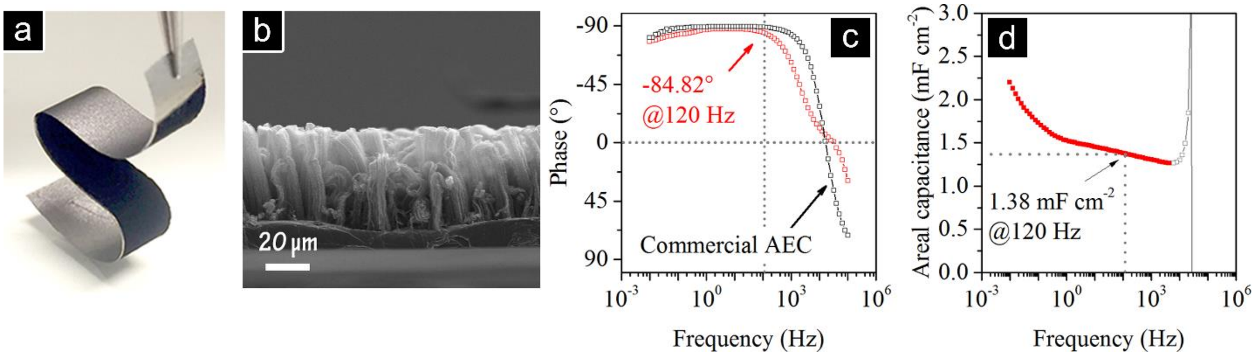

Figure 51. (a) Optical picture and (b) SEM image of graphite/VACNTs electrodes. (c) Phase angle and (d) frequency-dependent capacitance of the graphite/VACNTs based EC (**Paper III**). (Reproduced with permission from Elsevier)

3.5.4 Remarks

High-frequency ECs can replace bulky electrolytic capacitors, one of the biggest components on circuit boards, with an advantage in higher energy density and thus size reduction of circuit boards for IoT systems. However, for high operating voltages, designs such as bipolar capacitors must be employed to stack ECs together in series. Since the capacitance density of ECs scales up as $1/V^2$ (V is the device operating voltage), and by contrast, capacitance density of an electrolytic capacitor scales like $1/V$ because the CV product of anodic dielectric is approximately constant [267]. Therefore, the advantage of capacitance density for ECs will disappear at a particular voltage (43 V for the high-frequency EC in **Paper III**). Fortunately, in portable electronics equipment, 2 V can be sufficient for bypass and filtering purpose capacitors [13]. At such low voltages, the size advantage of ECs is rather significant.

CHAPTER 4

Encapsulation and integration challenges

As a practical device, the best combination of core EC materials, i.e. the electrodes, electrolytes, and separators, must be properly encapsulated, and then be integrated with other system components such as energy harvesters, sensors, and PMUs to construct effective miniaturized self-powered systems. The encapsulation and integration aspects pose mostly engineering challenges in device design and fabrication of ECs, and also materials challenges that the EC materials must be compatible with the ambient conditions that occur during the encapsulation and integration processes. This chapter starts with overviewing common COTS ECs with emphasis on their configurations, then elaborates the need for surface-mount designs for the purpose of high circuitry density and system miniaturization, and in the end briefly discusses the solutions from EC development point of view.

4.1 Common COTS electrochemical capacitor configurations

The configuration design of COTS ECs is strongly linked to the targeted market and cost-efficiency. Common options are coin cells, cylindrical (wound) cells, prismatic cells, and pouch cells. Large modules of unit cells in the above configurations connected in series or parallel are also commonly seen in the market for high energy and power applications.

Coin cells, also known as button cells, are usually shaped like a squat cylinder typically 5 to 25 mm in diameter and 1 to 6 mm in height. Materials are encapsulated by metal cans separated by an insulating gasket in a coin cell configuration, and the positive and negative terminals are thus located on the opposite side of the squat cylinder.

Cylindrical cells are also called wound type cells by some manufacturers. The electrode and separator layers are rolled up, fitted with pin connectors and placed in a cylindrical casing. The positive and negative terminals can be arranged either on the same base plane (e.g. radial or radial snap-in type) or on the two different base planes of the cylinder (axial type. Before the winding process for encapsulation, a rubber gasket is placed on the top, and the case opening is folded over and then pressed into the rubber to form hermetic sealing. A safety vent can be provided for releasing excessive pressure (usually over 7 atm) built up during operation [43].

In prismatic cells, the materials (rolled-up sheets) are wrapped in a metallic housing resembling a box of chewing gum. This configuration is suitable for high energy and power applications since a relatively large surface area in dissipating heat from the cell interior to the exterior is available. There is a debate on which of the cylindrical and prismatic types is the better choice. It is acknowledged that large prismatic cells have a higher energy density, especially when they are assembled in modules for geometric reasons, however, prismatic cells contain more parts than cylindrical cells and are more expensive to manufacture [43].

In pouch cells, a number of “positive electrode - separator - negative electrode” stacks are piled up, and the electrodes of the same polarity are connected and welded to the terminal conductive foil-tabs which are brought to the outside in a fully sealed way. The pouch cell makes the most efficient use of space and achieves 90-95% packaging efficiency. However, the pouch cell has little tolerance for swelling due to gassing from electrolyte decomposition, and are vulnerable to puncture and similar types of mechanical influence because of soft packaging. Pouch cells use aluminum laminated film containing polymer layers [105] for the casing. Polymer-based sealed wraps are not water- and air-tight for long-term applications. Thermal management efficiency is low compared to other configurations, though it may be a minor issue for miniaturized systems.

4.2 Design considerations for system miniaturization

4.2.1 Surface-mount ECs

For a small size of the whole system, besides requiring that the constituting unit components are small, it is furthermore essential to consider the method of integration for high spatial efficiency. In electronic industries, surface mount technology (SMT) is regarded as a revolutionary change [268]. By mounting flat leaded or leadless components and electronic packages on the surface of printed circuit boards (PCBs), SMT allows a higher degree of automation, higher circuitry density, and smaller volume, as opposed to the counterpart through-hole technology (THT). Using surface mount devices (SMDs) could deliver up to 90% reduction in weight and volume, compared to using through-hole devices (THDs) [268] as sketched in Figure 52. Therefore, it is advantageous to design surface-mountable ECs for miniaturized self-powered systems based on PCBs.

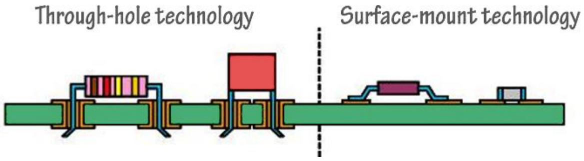

Figure 52. Through-hole technology and surface-mount technology [269].

A few types of surface-mount ECs are available on the market. Some designs are basically a coin type capacitor sitting on a surface mountable holder, which unfortunately leads to a high profile. The same concern comes with the cylindrical type ECs that can sit on a holder, or with their terminal leads designed to be flat for surface mountability. Comparatively, prismatic and pouch cells have smaller dead volumes on the module level and higher degrees of design freedom. The companies of Cap-XX, AVX and muRata have presented a series of pouch type ECs with very thin profiles, down to 0.4 mm for a 35 mF muRata product [270]. The pouch ECs can be surface mountable with flat leads. Cellergy, another player in the market, utilizing conventional screen or stencil printing techniques for the fabrication of prismatic type of ECs. Cellergy ECs are also surface mountable with a low profile by designing flat leads. Using the printing technology, the smallest footprint achievable is 12×12.5 (L×W) mm^2, and the highest capacitance of 12 mF is at

2.4 mm thickness and 3.5 V voltage, the highest voltage is 6.3 V at 3.4 mm and 7 mF [271]. Specifically, aiming for applications in microsystems, SEIKO and CLC Factory have presented the smallest 3.2×2.5×0.9 (L×W× H) mm^3 surface-mount chip type ECs with capacitances on the order of 10 mF [272, 273].

The successful commercialization of the devices above can be taken as evidence of the effectiveness of their designs. Nevertheless, there is still room for improvement. For example, sizing down of the footprint may be problematic for pouch cells, considering that sufficient sealant area on the edge should be preserved for hermetic sealing, otherwise the device would be more vulnerable to mechanical shocks and pressure build-up caused by gas generation. The water- and airtightness may also be questionable under harsh climate conditions. For printing technology, the choice of electrode and electrolyte materials could be limited, indicating that the advanced materials developed in the laboratory cannot be directly utilized. Additional development of stable inks may be necessary. Moreover, the allocation of terminals is difficult to design on the flat surface for the conventional configurations. This makes it necessary to use glue or adhesive tape on the flat surface (to attach on PCBs) for mechanical stability, unfortunately aggravating reliability concerns.

In a nutshell, novel encapsulation and integration concepts are always appreciated. Ideally, the design and manufacturing technology should allow for surface mountability, convenient allocation of terminal positions, easy adaptation in geometry design as well as an arbitrary choice of materials, and moreover, compatibility with bipolar designs.

4.2.2 Reflow-soldering

SMDs can be assembled onto PCBs with the use of solder paste reflow, wave soldering or conductive adhesive curing processes. The last is mostly used in some flexible circuit boards or boards with heat-sensitive components, while the wave soldering is more efficient for THDs [268].

To start the reflow-soldering process, the solder powder and flux are pre-blended to form a sticky thixotropic solder paste, and the paste is used to temporarily attach SMDs on their contact pads. Afterward, the entire assembly is subjected to controlled heat above the liquidus temperature of the solder paste for a short period, which melts the solder, permanently connecting the joint [268]. Although the heat may be applied by soldering individual joints with a hot air pencil, a higher degree of automation and productivity is through the use of a reflow oven for batch processing (Figure 53a). This could pose challenges to EC technology, since the peak temperature can go up to more than 300 °C, depending on the solder material. Therefore, the EC encapsulation and the core materials should preferably be able to withstand high-temperature exposure, usually for a short period of time, on a scale of minutes.

The reflow-soldering process can cause performance deterioration of the device if the materials or packaging solution is inappropriate. For example, heat will cause thermal expansion of the components, and if the electrolyte can be vaporized, substantial pressure is produced inside the cell. The increased pressure can break the encapsulation, leading to total device failure, or deform the exterior packaging as shown in Figure 53b. After the temperature cools down, the electrolyte vapor re-liquidifies, and the electrode material may lose contact with the current collector, etc., thus increasing the device resistance.

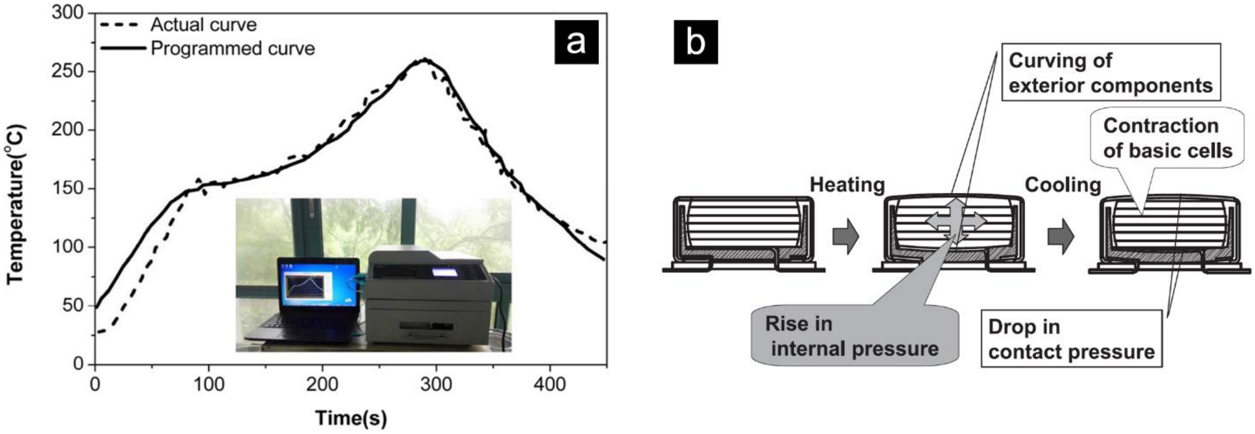

Figure 53. (a) Example of a reflow curve (solid – programmed; dash - actual) with inset of reflow equipment [17]. (b) Mechanism of ESR increase due to reflow [274]. (Reproduced with permission from IEEE and NEC)

In this regard, solid-state electrolytes can eliminate the effect of the pressure build-up by electrolyte vaporization, in addition to their advantages in leakage-free features, ease for packaging, etc. An ionogel electrolyte employing the co-condensation of tetramethoxysilane (TEOS) and dimethyldimethoxysilane (DMDMS) as precursors for the silica matrix confining EMImTFSI was demonstrated as a promising solid-state electrolyte for MSCs with good compatibility with the reflow-soldering process [16]. Only a few studies on reflow-soldering ECs have been reported [16, 17, 274, 275], but this property could be very critical for the successful application in miniaturized systems, as the state-of-art heterogeneous packaging solutions for high-density circuits call for surface mount devices and reflow-soldering step is indispensable.

4.3 On-chip MSCs and multi-function ECs

The on-chip MSC technology may be a great fit for miniature systems due to their freely designable form factors, high compatibility with heterogeneous integrations and potentially large scale and cost-effective production. In the past decades, developments in novel fabrication processes, new materials, and unconventional configurations have generated a large number of high-performance device prototypes towards the applications in IoT systems. The transition to thick film technology and 3D structures present ways to enhance the energy density of MSCs. However, one of the most challenging issues facing MSCs is encapsulation. The encapsulation is even more problematic if a liquid electrolyte is used. The vaporization, in addition to the decomposition limit, must be taken into account which can rule out several high-temperature, yet sophisticated MEMS techniques e.g. diffusion wafer bonding, glass frit wafer bonding, etc [276]. Low-temperature encapsulation of on-chip storage devices are demonstrated with a conformal coating of parylene film (Figure 54a), and the aid of UV curable epoxy resist and a glass lid covering of the electrode/separator/electrolyte stack or finger structures in an etched cavity [277, 278] (Figure 54b). High temperature durable solid-state MSCs are more advantageous in terms of encapsulation, making it possible to be used as a bare die, to be molded together with other components in the final step of system encapsulation (Figure 54c).

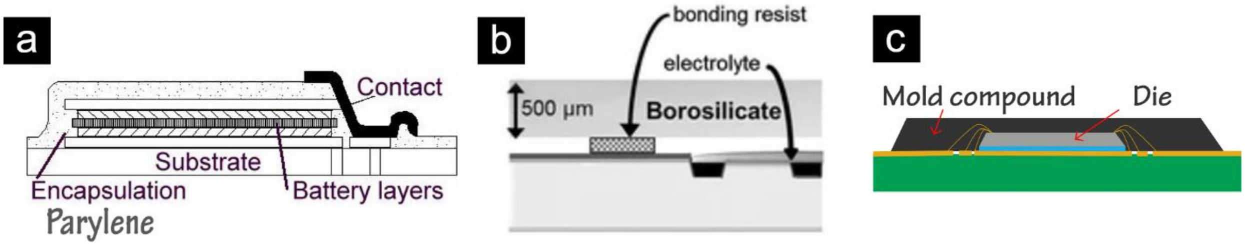

Figure 54. Schematics of encapsulation. Low-temperature encapsulation with (a) parylene film [279] and (b) epoxy glue and a glass lid [278]; (c) Bare die packaging in a mold compound. (a – b reproduced with permission from IOP and Springer)

Besides the on-chip MSCs, the material innovations have resulted in more unconventional prototype devices [280] – flexible [281], transparent [282], stretchable [283] and/or compressible [284], viable to be of almost arbitrary form factors such as fiber-like [285], being space efficient. Also, recent novel devices show multi-functions, for example, structural ECs, electrochromic ECs [286], thermo-switchable ECs [287], and self-healing ECs [288]. With the maturing of the new technologies and encapsulation solutions, these emerging ECs are promising for IoT systems with heterogeneous functions.

CHAPTER 5

Summary and perspectives

The market of ECs is diversified, ranging from kilo-Farad devices for automotive applications to milli-Farad ECs for microelectronics, and the application domains expand from energy storage to a.c. line filtering. The miniaturized self-powered systems for IoT which call for high efficiency, reliability and durable storage units are a new arena that ECs characteristics fit in. However, the critical implementation requirements present manifold challenges in the electrochemical performance, device form factors, and packaging solutions. The solutions to these challenges are diverse, and each specific application scenario calls for different answers and technologies. The step-by-step optimization starting from the materials properties, up to the electrode structures, and further to the device configurations can surely tune the performance to the desired level. Exploiting the innovation in packaging technologies, encapsulating the device in a favorable geometry and dimension for integration on chips or PCB boards is the next key step for enabling miniature autonomous systems for IoTs.

Advanced carbon electrode materials with suitable porosity in relation to the electrolyte properties, with a hierarchical porous network, and which are starvation effect-free are essential to building EDLCs with high capacitance, high power, high cycling stability and short time constant. Heteroatoms doping and favorable surface groups could further enhance the energy density through pseudocapacitance, but the aging due to oxygen-containing groups with organic electrolytes is a concern and challenge for long lifetime designs. Pseudocapacitive materials, leveraging fast surface redox reactions, enhance the energy density to a higher magnitude in theory. However, materials engineering for high conductivity and fast ion transport is indispensable to come close to the theoretical capacitance. Compositing carbon and pseudocapacitive materials is an effective strategy to create high-performance electrodes. The interface should be designed for optimal synergy between the constituting components. Searching for new materials and chemistry which enables multi-electron redox reactions [33] markedly increases the energy density, while the chemistry complexity could present a barrier for long cycling lifetime. Electrolyte materials as the provider of ionic charge carriers determine critical parameters including mass transport kinetics, working voltage window, and thermal durability. High voltage, wide temperature range and solid-state are the ideal features for many advanced systems. Ionic liquids with high voltage window and decomposition point are promising for high energy density and wide temperature ranges that are favored by applications in self-powered systems. The ionogels consisting of ionic liquid and a polymer network in a solid-state form make device encapsulation and integration convenient. Redox electrolytes provide the opportunity of turning the conventionally inactive electrolyte into an active component for efficient energy enhancement. The complexity in storage mechanisms presents both challenges and opportunities for device engineering. Advanced electrolyte additive materials may significantly influence the conductivity, temperature range, and self-discharge properties.

Building the electrodes into a compact and thick film while preserving sufficient pathways for electron and ion transport is a powerful approach for enhancing the energy density. The thick electrodes increase the weight and volume fraction of active materials, which is an important improvement for small-sized devices. Decreasing the tortuosity is essential for minimal power density loss. Creating a 3D structured electrode and conductive percolation network is effective to minimize the power loss for high mass-loading electrodes. Materials from wood are promising for processing advanced electrodes, e.g. wood chips with an ultra-long tunnel-like structure for low tortuosity, and cellulose nanofibrils with a high aspect ratio as the backbone of percolation networks. To process thick electrodes, novel fabrication methods and binder materials are key to ensure adequate mechanical properties, good cohesion between electrode particles and strong adhesion to current collectors.

The asymmetric device design efficiently enlarges the working voltage range. The exploration of metal-ion capacitors e.g. lithium-, sodium-, potassium-ion capacitors brings the performance of EC technology to a new level. The consideration from the charge flow balance generates a number of approaches for device design that upgrade the voltage and energy density. In this regard, the *PZV* value is a critical parameter. Although it has been shown that the *PZV* value can be tuned by mass balancing, pore-ion size matching, and cyclic charging/discharging, more systematic approaches are needed to control the *PZV* for maximum performance. This may be a complicated scientific issue and vary from system to system, as *PZV* is closely related to the interaction between electrode and electrolyte, and sensitive to the surface chemistry of the electrodes as well as the device operating history. The bipolar configuration is an effective solution that scales the voltage linearly. An efficient bipolar design keeps the same performance in self-discharge and leakage current at maximum voltage, temperature durability, and frequency response, while improving the energy density per weight and volume due to space efficiency. However, bipolar device fabrication presents great challenges in reproducibility and reliability because all the unit cells should be "balanced". Automation production is promising to upscale miniature bipolar ECs. The device topology and configurations of MSCs are critical to their performance. The 3D MSC structures are effective to increase the loading of materials per footprint, therefore, the areal energy density.

Encapsulating the devices for a miniature form factor while also enabling convenient integration is challenging but vital for practical applications. The ability of surface mounting and endurance to reflow-soldering processes are the sought-after properties of the encapsulation solution, for the sake of high-density circuit and system miniaturization, and leveraging the existing fabrication technologies. The MSC encapsulation is crucial for producing complete laboratory cell prototypes and advancing to its first commercial product. In general, the encapsulation challenge can be greatly alleviated for solid-state devices, thereby calling for high-performance solid-state electrolytes.

The ultimate improvements lie in high energy, high voltage, high power, short time constant, long lifetime, wide temperature range, low self-discharge and leakage current device encapsulated in surface mountable, reflow-soldering tolerant and freely designable form factors. Unfortunately, the physics goes against the wish – e.g. high power characteristics are indicative of poor energetic performances – meaning that one has to deal with the trade-offs in reality, improve the most critical performance characteristic at the minimal sacrifice of others.

Although this thesis has emphasized extensively on the application aspects in the miniaturized self-powered systems, the fundamental studies related to the charge storage mechanisms, the influence of pore surface properties, ion dynamics, with the aid of *in situ* and *operando* characterization techniques, theoretical modeling and simulation will greatly facilitate the understanding for efficient device design towards specific applications. Moreover, the standardization of performance evaluation is urgently required. For the miniaturized self-powered systems application, new characteristic evaluation standards can be required, e.g. the effective capacitance as a function of pulse width, self-discharge with short voltage holding, leakage current equilibration time, and capacitive charging at ultra-low current, etc.

Seeing the great advancement in miniature energy storage technology, although still lagging behind miniaturization of other technologies, the brilliant prospects of IoT, even further to IoE and tactile internet is probably not too distant from becoming reality.

CHAPTER 6

Summary of appended papers

At this point, hopefully my readers have acquired the necessary background to appreciate the work in the appended papers of the thesis. A brief summary of each paper (arranged in chronological order in terms of publication year) is presented in this chapter.

Paper I presents a study on KBr as a redox liquid electrolyte in the case of a symmetric EC, for enhancing the energy density while retaining capacitor level power and cycling stability. The bromide ion is involved in a redox couple of Br^-/Br_3^- with a standard electrode potential at 1.05 V vs. NHE. The high standard potential is one of the motivations for employing Br^-/Br_3^- to enhance the energy density, as the energy is the product of capacity and voltage. At the same time, the high potential enables several interesting electrochemical signatures. One of them is the voltage-dependent behavior, with 1.6 V device voltage as a threshold – at a lower voltage, the device corresponds to an EDLC; at a higher voltage up to 1.9 V, the device operates as a hybrid type EC. Moreover, the KBr-containing device also presents a history-dependent behavior. It is found that the capacity increases with cycling at 1.9 V. After pre-cycling at 1.9 V, then lowering the voltage to 1.6 V, the device has been incorporated with Br^-/Br_3^- redox activities and energy density is thus enhanced comparing with directly running the device at 1.6 V without pre-cycling. The pre-cycling seems to activate the redox reaction at 1.6 V, therefore the pre-cycling step is denoted as a “triggering operation” in the paper. It is proved that the history-dependent behavior is accompanied by shifts of the electrode potentials and *PZV* values. After the triggering operation, *PZV* is pushed positively by about 70 mV, and the upper limit of the positive electrode potential is lifted by 110 mV, being higher than the onset potential and thus initiating the Br^-/Br_3^- redox couple at device voltage 1.6 V. Finally, we offer an explanation to the phenomenon with speculative electro-oxidation of the positive electrode and redox reaction kinetics.

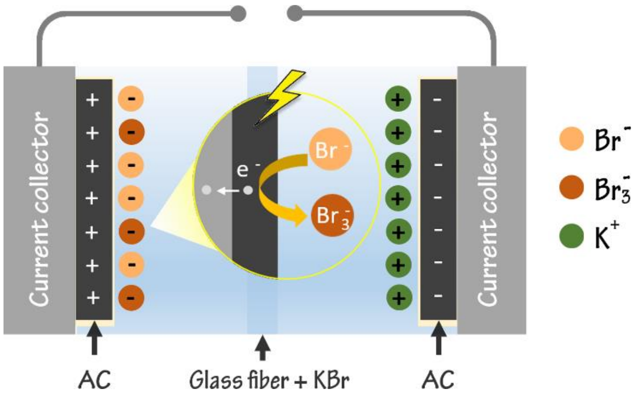

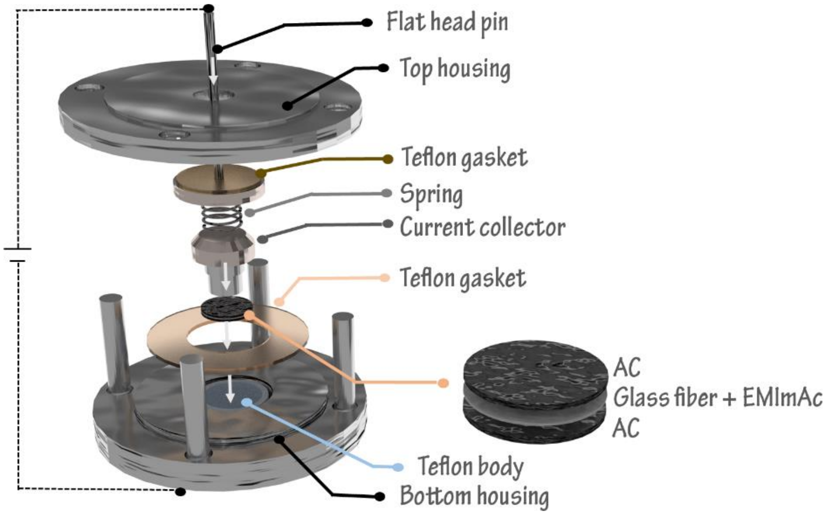

Paper II investigates the ionic liquid EMImAc as an electrolyte, for extreme-high-temperature ECs. This paper highlights several important hints for how to operate the device at a high temperature. Due to enhanced activities at elevated temperatures, the maximum operating voltage is decreased from 1.5 V at room temperature to 1.4 V at 120 °C and further to 1.3 V at 150 °C. At the same time, the resistance and thus the voltage drop also decreases from 186 mV at room temperature to 26 mV at 120 °C and 23 mV at 150 °C. The overall influence on the energy and power densities at an elevated temperature is actually positive – the energy storage ability is enhanced despite trading operating voltage for stability at a high-temperature. The electrolyte ionic liquid EMImAc and evaluation conditions were selected in view of specific requirements motivated by the smart-MEMPHIS project, but the obtained conclusions and hints for applications in this paper are generic to other neat ionic liquids as well as high-room-temperature-viscosity electrolytes. Moreover, to enable the extreme-high-temperature study and a practical device, the encapsulation and packaging need a specific design to cope with the influence caused by the mismatch in thermal expansions of different cell components.

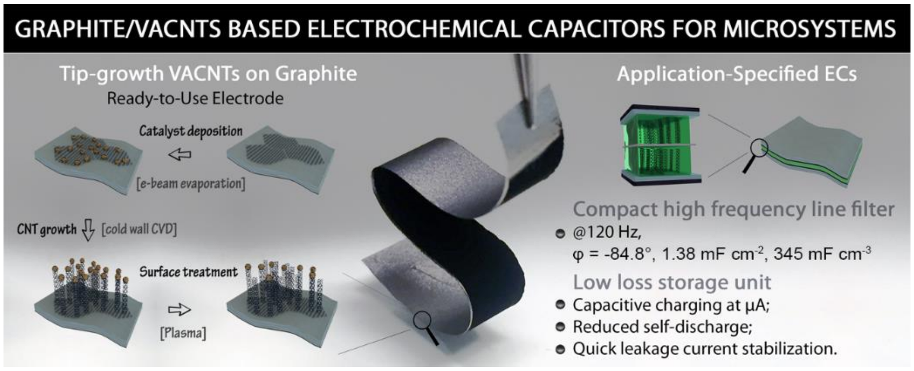

Paper III demonstrates different types of ECs for microsystems. One for a.c. line filtering purposes, and the other one for energy storage. All the devices' electrodes consist of a graphite/VACNTs material, which was fabricated through a CVD process with the tip-growth mechanism. The VACNTs were grown vertically on the top of a highly oriented graphite film, with the roots of the VACNTs closely connected to the surface layer of the graphite. The characterization indicates a similar covalent bonding structure as in graphene-CNT hybrid materials. This feature endows the ultra-fast response for a.c. line filter ECs with KOH as an electrolyte. For the storage ECs made of the same materials, a gel electrolyte PVA/H_3PO_4 was employed and low-current charging and slow self-discharge were demonstrated. In the end, the quick equalization of leakage current, which is beneficial to minimize the loss during voltage holding, was discussed briefly.

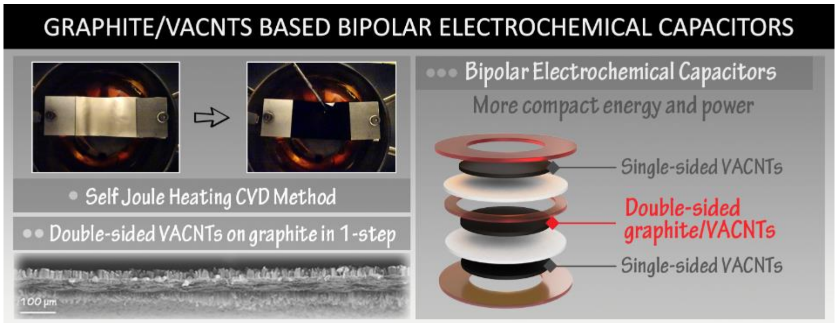

Paper IV continues the utilization of the CVD-grown VACNTs on graphite, and explores the bipolar configuration. In this paper, we utilized a double-sided graphite/VACNTs (DSGC) material as the bipolar electrode, and fabricated a two-unit bipolar device with PVA/H_3PO_4 gel electrolyte. The bipolar device exhibits ideal performance in terms of uncompromised capacitance, cycling stability and self-discharge, in conjunction with the doubling in voltage limit which results in a higher energy density than for the single units. These results indicate that the new self-joule heating method for growing the DSGC material is effective and promising for miniature bipolar ECs fabrication. This paper was initially motivated by the desire to achieve an increase in the voltage limits of the ECs in **Paper III**. However, developing *liquid* electrolyte based bipolar ECs is a more severe challenge, and the bipolar configuration demonstration for the KOH-containing a.c. line filter ECs remains to be developed.

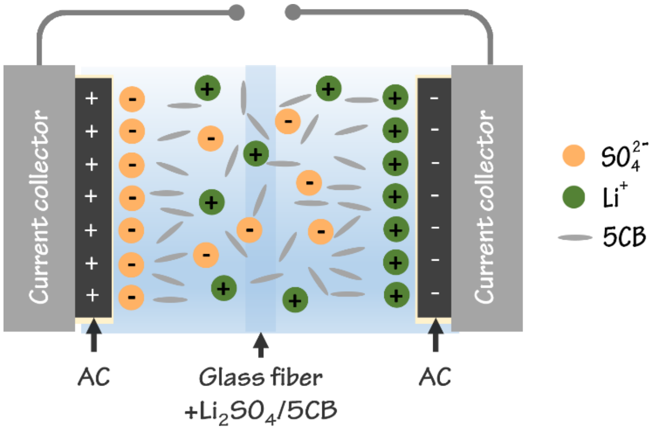

Paper V investigates the liquid crystal 5CB as an additive in the aqueous electrolyte Li_2SO_4, for suppression of the self-discharge and leakage current. The addition of 2% of 5CB reduces the self-discharge rates and leakage current at cell voltages from 1.0 to 1.6 V. Comparing with other reported methods, the 5CB additive method in this work has an advantage of little compromise in the capacitance, energy density, power density and cycling stability. This work was inspired by a report on mixing 5CB in an organic electrolyte system, where an electrorheological effect, causing an enhanced fluid viscosity that slows down charge redistribution and Faradaic reactions, was claimed to be the reason for mitigating self-discharge. For the aqueous system in this paper, the main difference is the low miscibility of 5CB in water and a phase separation may exist at room temperature for the Li_2SO_4/5CB system. We point out that the underlying mechanism of liquid crystal suppressing self-discharge is worth further investigation.

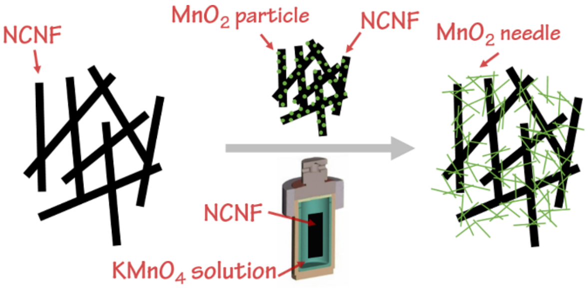

Paper VI reports a carbon/MnO_2 material as an electrode material. The incorporation of MnO_2 into a carbon network is a common strategy for enhancing the energy density through the synergy between the high pseudocapacitance of (poorly conductive) MnO_2 and high conductivity of (low capacitance) carbon. The carbon/MnO_2 composites usually have an inferior rate capability compared to pure carbon. Surprisingly, we observed that the composite between NCNF (nitrogen-doped carbon nanofiber derived from electrospun cellulose acetate) and MnO_2 in this work has an extraordinary rate capability, substantially higher than the pure NCNF. The results can be explained by the fact that (1) the MnO_2 component is mostly electrochemically inactive due to a non-intimate contact with the NCNF carbon, and (2) more importantly, the NCNF carbon property is significantly modified during the compositing process, i.e. the reaction with $KMnO_4$ under a hydrothermal condition. The hydrothermal condition presumably initiates the Ostwald ripening of MnO_2, finally concentrating it on the external surface of NCNF, and thereby making it easily removable from the NCNF surface. This structure offers an opportunity to study how the carbon substrate is modified by the compositing chemistry. The results highlight the importance of not overlooking the modification of the carbon substrate when investigating carbon composite electrodes such as carbon/MnO_2 networks.

REFERENCES

[1] Z. L. Wang, Nano Energy, 58 (2019) 669-672 doi: 10.1016/j.nanoen.2019.02.012.

[2] A. Othman, Energy storage system options in intelligent wireless sensor network, 2017 International Conference on Military Technologies (ICMT), 2017.

[3] G. Chen, et al., A cubic-millimeter energy-autonomous wireless intraocular pressure monitor, 2011 IEEE International Solid-State Circuits Conference, 2011.

[4] M. Choi, et al., Sensors (Basel), 17 (2017) doi: 10.3390/s17102190.

[5] I. Lee, et al., A 179-lux energy-autonomous fully-encapsulated 17-mm 3 sensor node with initial charge delay circuit for battery protection, 2018 IEEE Symposium on VLSI Circuits, 2018.

[6] S. Sudevalayam, P. Kulkarni, Ieee Commun Surv Tut, 13 (2011) 443-461 doi: 10.1109/Surv.2011.060710.00094.

[7] M. A. Hannan, et al., Renewable & Sustainable Energy Reviews, 69 (2017) 771-789 doi: 10.1016/j.rser.2016.11.171.

[8] A. Vlad, et al., Advanced Energy Materials, 5 (2015) 1402115 doi: 10.1002/aenm.201402115.

[9] S. Zheng, et al., Adv Mater, 31 (2019) e1900583 doi: 10.1002/adma.201900583.

[10] M. Beidaghi, Y. Gogotsi, Energy Environ. Sci., 7 (2014) 867-884 doi: 10.1039/c3ee43526a.

[11] H. G. Lee, N. Chang, Powering the IoT: Storage-less and converter-less energy harvesting, The 20th Asia and South Pacific Design Automation Conference, 2015.

[12] C. Lethien, et al., Energy & Environmental Science, 12 (2019) 96-115 doi: 10.1039/c8ee02029a.

[13] J. R. Miller, et al., Science, 329 (2010) 1637-1639 doi: 10.1126/science.1194372.

[14] D. Chapman, W. Trybula, Meeting the challenges of oilfield exploration using intelligent micro and nano-scale sensors, 2012 12th IEEE International Conference on Nanotechnology (IEEE-NANO), 2012.

[15] S. I. Inc., Cpx capacitors cpx3225a752d, https://www.sii.co.jp/en/me/datasheets/chip-capacitor/cpx3225a752d/, Acessed on 0429.

[16] M. Brachet, et al., J. Mater. Chem. A, 4 (2016) 11835-11843 doi: 10.1039/c6ta03142k.

[17] Y. Wang, et al., Ieee Transactions on Dielectrics and Electrical Insulation, 24 (2017) 676-681 doi: 10.1109/Tdei.2017.006234.

[18] J. Huang, et al., Chemistry, 14 (2008) 6614-6626 doi: 10.1002/chem.200800639.

[19] J. S. Huang, et al., Journal of Materials Research, 25 (2010) 1525-1531 doi: 10.1557/Jmr.2010.0195.

[20] H. V. Helmholtz, Annalen der Physik, 243 (1879) 337-382 doi: 10.1002/andp.18792430702.

[21] M. Gouy, J. Phys. Theor. Appl., 9 (1910) 457-468 doi. 10.1051/jphystap:019100090045700

[22] D. L. Chapman, The London, Edinburgh, and Dublin philosophical magazine and journal of science, 25 (1913) 475-481.

[23] O. Stern, Zeitschrift für Elektrochemie und angewandte physikalische Chemie, 30 (1924) 508-516.

[24] J. Chmiola, et al., Science, 313 (2006) 1760-1763 doi: 10.1126/science.1132195.

[25] A. Noori, et al., Chem Soc Rev, 48 (2019) 1272-1341 doi: 10.1039/c8cs00581h.

[26] B. Conway, Electrochimica acta, 38 (1993) 1249-1258 doi: 10.1016/0013-4686(93)80055-5.

[27] B. E. Conway, Electrochemical supercapacitors: Scientific fundamentals and technological applications, first ed., Springer Science & Business Media, New York, 2013.

[28] S. Sarangapani, et al., Journal of the Electrochemical Society, 143 (1996) 3791-3799 doi: Doi 10.1149/1.1837291.

[29] G. Z. Chen, Int Mater Rev, 62 (2017) 173-202 doi: 10.1080/09506608.2016.1240914.

[30] V. Augustyn, et al., Energy & Environmental Science, 7 (2014) 1597-1614 doi: 10.1039/c3ee44164d.

[31] Y. Gogotsi, R. M. Penner, ACS Nano, 12 (2018) 2081-2083 doi: 10.1021/acsnano.8b01914.

[32] M. Okubo, et al., J Am Chem Soc, 129 (2007) 7444-7452 doi: 10.1021/ja0681927.

[33] M. R. Lukatskaya, et al., Nat Commun, 7 (2016) 12647 doi: 10.1038/ncomms12647.
[34] T. Brousse, et al., Journal of The Electrochemical Society, 162 (2015) A5185-A5189 doi: 10.1149/2.0201505jes.
[35] A. Laheaar, et al., Electrochemistry Communications, 60 (2015) 21-25 doi: 10.1016/j.elecom.2015.07.022.
[36] Y. Jiang, J. Liu, Energy & Environmental Materials, 2 (2019) 30-37 doi: 10.1002/eem2.12028.
[37] J. Yue, et al., Journal of Materials Chemistry A, 5 (2017) 1978-1988 doi: 10.1039/c6ta06840e.
[38] M. Opitz, et al., Electrochimica Acta, 168 (2015) 125-132 doi: 10.1016/j.electacta.2015.03.186.
[39] H. Vogt, Electrochimica Acta, 39 (1994) 1981-1983 doi: Doi 10.1016/0013-4686(94)85077-1.
[40] M. Forghani, S. W. Donne, Journal of the Electrochemical Society, 165 (2018) A664-A673 doi: 10.1149/2.0931803jes.
[41] B.-A. Mei, et al., The Journal of Physical Chemistry C, 122 (2017) 194-206 doi: 10.1021/acs.jpcc.7b10582.
[42] S. L. Zhang, N. Pan, Advanced Energy Materials, 5 (2015) 1401401 doi: 10.1002/aenm.201401401.
[43] M. Lu, et al., Supercapacitors: Materials, systems and applications, John Wiley & Sons, 2013.
[44] P. L. Taberna, et al., Journal of the Electrochemical Society, 150 (2003) A292-A300 doi: 10.1149/1.1543948.
[45] J. Y. Zhao, et al., Journal of Power Sources, 363 (2017) 327-340 doi: 10.1016/j.jpowsour.2017.07.066.
[46] A. Balducci, et al., Journal of The Electrochemical Society, 164 (2017) A1487-A1488 doi: 10.1149/2.0851707jes.
[47] S. Pohlmann, A. Balducci, Electrochimica Acta, 110 (2013) 221-227 doi: 10.1016/j.electacta.2013.02.114.
[48] P. W. Ruch, et al., Electrochimica Acta, 55 (2010) 4412-4420 doi: 10.1016/j.electacta.2010.02.064.
[49] D. Weingarth, et al., Journal of Power Sources, 225 (2013) 84-88 doi: 10.1016/j.jpowsour.2012.10.019.
[50] R. De Levie, Electrochimica Acta, 8 (1963) 751-780 doi.
[51] Y. Gogotsi, P. Simon, Science, 334 (2011) 917-918 doi: 10.1126/science.1213003.
[52] N. A. Kyeremateng, et al., Nat Nanotechnol, 12 (2017) 7-15 doi: 10.1038/nnano.2016.196.
[53] V. Srinivasan, J. W. Weidner, Journal of the Electrochemical Society, 146 (1999) 1650-1658 doi: 10.1149/1.1391821.
[54] T. Y. Liu, et al., Journal of Materials Chemistry A, 5 (2017) 17705-17733 doi: 10.1039/c7ta05646j.
[55] Y. Zhai, et al., Adv. Mater., 23 (2011) 4828-4850 doi: 10.1002/adma.201100984.
[56] O. Crosnier, et al., Current Opinion in Electrochemistry, 9 (2018) 87-94 doi: 10.1016/j.coelec.2018.05.005.
[57] M. S. Balogun, et al., Journal of Materials Chemistry A, 3 (2015) 1364-1387 doi: 10.1039/c4ta05565a.
[58] X. Rui, et al., Nanoscale, 6 (2014) 9889-9924 doi: 10.1039/c4nr03057e.
[59] X. Li, et al., Small, 13 (2017) 1701530 doi: 10.1002/smll.201701530.
[60] G. A. Snook, et al., Journal of Power Sources, 196 (2011) 1-12 doi: 10.1016/j.jpowsour.2010.06.084.
[61] L. L. Peng, et al., Advanced Energy Materials, 8 (2018) 1702179 doi: 10.1002/aenm.201702179.
[62] D. B. Xiong, et al., Small, 14 (2018) 1703419 doi: 10.1002/smll.201703419.
[63] X. J. Li, et al., Journal of Materials Chemistry A, 5 (2017) 15460-15485 doi: 10.1039/c7ta04001f.
[64] J. Cherusseri, et al., Nanoscale Horizons, 4 (2019) 840-858 doi: 10.1039/c9nh00152b.
[65] M. Acerce, et al., Nat Nanotechnol, 10 (2015) 313-318 doi: 10.1038/nnano.2015.40.
[66] R. R. Salunkhe, et al., ACS nano, 11 (2017) 5293-5308 doi: 10.1021/acsnano.7b02796.
[67] R. R. Salunkhe, et al., Accounts of chemical research, 49 (2016) 2796-2806 doi: 10.1021/acs.accounts.6b00460.

[68] M. Y. Wang, et al., Chemelectrochem, 6 (2019) 2984-2997 doi: 10.1002/celc.201900298.
[69] N. A. Choudhury, et al., Energy Environ. Sci., 2 (2009) 55-67 doi: 10.1039/b811217g.
[70] C. Ramasamy, et al., J. Solid State Electrochem., 18 (2014) 2217-2223 doi: 10.1007/s10008-014-2466-3.
[71] C. Ramasamy, et al., J. Solid State Electrochem., 18 (2014) 2903-2911 doi: 10.1007/s10008-014-2557-1.
[72] P. M. Dicarmine, et al., J. Phys. Chem. C, 118 (2014) 8295-8307 doi: 10.1021/jp5016214.
[73] R. Yuksel, et al., ACS Appl. Mater. Interfaces, 6 (2014) 15434-15439 doi: 10.1021/am504021u.
[74] K. F. Chiu, S. H. Su, Thin Solid Films, 544 (2013) 144-147 doi: 10.1016/j.tsf.2013.03.135.
[75] M. F. Hsueh, et al., J. Phys. Chem. C, 117 (2013) 16751-16758 doi: 10.1021/jp4031128.
[76] Y. D. Chiou, et al., Nanoscale, 5 (2013) 8122-8129 doi: 10.1039/c3nr01980b.
[77] M. A. Neouze, et al., Chemistry of Materials, 18 (2006) 3931-3936 doi: 10.1021/cm060656c.
[78] X. H. Liu, et al., Journal of Materials Chemistry A, 2 (2014) 11569-11573 doi: 10.1039/c4ta01944j.
[79] L. Hu, et al., ChemSusChem, 12 (2019) 1118-1132 doi: 10.1002/cssc.201802450.
[80] J. Lee, et al., Progress in Materials Science, 101 (2019) 46-89 doi: 10.1016/j.pmatsci.2018.10.005.
[81] S. E. Chun, et al., Nat. Commun., 6 (2015) 7818 doi: 10.1038/ncomms8818.
[82] Q. Abbas, et al., Electrochimica Acta, 140 (2014) 132-138 doi: 10.1016/j.electacta.2014.04.096.
[83] A. K. Samantara, S. Ratha, Materials development for active/passive components of a supercapacitor: Background, present status and future perspective, Springer, 2017.
[84] Y. M. Shulga, et al., J. Power Sources, 245 (2014) 33-36 doi: 10.1016/j.jpowsour.2013.06.094.
[85] H. J. Yu, et al., J. Power Sources, 206 (2012) 463-468 doi: 10.1016/j.jpowsour.2012.01.116.
[86] A. M. Bittner, et al., J. Power Sources, 203 (2012) 262-273 doi: 10.1016/j.jpowsour.2011.10.083.
[87] G. Zhao, Reuse and recycling of lithium-ion power batteries, John Wiley & Sons, 2017.
[88] K. Tonurist, et al., J. Electrochem. Soc., 156 (2009) A334-A342 doi: 10.1149/1.3079339.
[89] K. Tonurist, et al., J. Electrochem. Soc., 160 (2013) A449-A457 doi: 10.1149/2.044303jes.
[90] Y. Yue, H. Liang, Small Methods, 2 (2018) doi: 10.1002/smtd.201800056.
[91] I. Ryu, et al., Langmuir, 30 (2014) 1704-1709 doi: 10.1021/la4044599.
[92] H. W. Cho, et al., Synth. Met., 162 (2012) 410-413 doi: 10.1016/j.synthmet.2011.12.025.
[93] X. F. Gong, et al., J. Power Sources, 267 (2014) 610-616 doi: 10.1016/j.jpowsour.2014.05.120.
[94] F. Xiang, et al., Carbon, 75 (2014) 201-208 doi: 10.1016/j.carbon.2014.03.053.
[95] N. A. Alhebshi, et al., J. Mater. Chem. A, 1 (2013) 14897-14903 doi: 10.1039/c3ta12936e.
[96] R. F. Zhou, et al., Nanotechnology, 21 (2010) 345701 doi: 10.1088/0957-4484/21/34/345701.
[97] J. Xu, et al., Acs Nano, 7 (2013) 5453-5462 doi: 10.1021/nn401450s.
[98] J. Ji, et al., ACS Nano, 7 (2013) 6237-6243 doi: 10.1021/nn4021955.
[99] R. S. Kuhnel, A. Balducci, J. Power Sources, 249 (2014) 163-171 doi: 10.1016/j.jpowsour.2013.10.072.
[100] A. Brandt, et al., J. Mater. Chem. A, 1 (2013) 12669-12678 doi: 10.1039/c3ta12737k.
[101] C. Portet, et al., Electrochim. Acta, 49 (2004) 905-912 doi: 10.1016/j.electacta.2003.09.043.
[102] P. Simon, Y. Gogotsi, Nat. Mater., 7 (2008) 845-854 doi: 10.1038/nmat2297.
[103] T. Takahashi, et al., Nippon Steel & Sumitomo Metal Technical Report, (2015) .
[104] Targray, Targray packaging materials for battery manufacturing, https://www.targray.com/li-ion-battery/packaging-materials, Acessed on September 11, 2018.
[105] MTI, Aluminum laminated film for pouch cell case, http://www.mtixtl.com/AluminumLaminatedFilmforPolymerBatteryCase100mmWx210mmL50pcs.aspx, Acessed on September 11, 2018.
[106] G. Gryglewicz, et al., Electrochimica Acta, 50 (2005) 1197-1206 doi: 10.1016/j.electacta.2004.07.045.
[107] O. Barbieri, et al., Carbon, 43 (2005) 1303-1310 doi: 10.1016/j.carbon.2005.01.001.

[108] G. Salitra, et al., J. Electrochem. Soc., 147 (2000) 2486-2493 doi: Doi 10.1149/1.1393557.
[109] L. Eliad, et al., J. Phys. Chem. B, 105 (2001) 6880-6887 doi: 10.1021/jp010086y.
[110] L. Eliad, et al., Appl. Phys. a-Mater., 82 (2006) 607-613 doi: 10.1007/s00339-005-3440-9.
[111] C. Vix-Guterl, et al., Carbon, 43 (2005) 1293-1302 doi: 10.1016/j.carbon.2004.12.028.
[112] J. Chmiola, et al., Angew. Chem. Int. Ed. Engl., 47 (2008) 3392-3395 doi: 10.1002/anie.200704894.
[113] M. Deschamps, et al., Nat. Mater., 12 (2013) 351-358 doi: 10.1038/nmat3567.
[114] E. Raymundo-Pinero, et al., Carbon, 44 (2006) 2498-2507 doi: 10.1016/j.carbon.2006.05.022.
[115] H. Nishihara, et al., Chem. Eur. J., 15 (2009) 5355-5363 doi: 10.1002/chem.200802406.
[116] J. Chmiola, et al., J. Power Sources, 158 (2006) 765-772 doi: 10.1016/j.jpowsour.2005.09.008.
[117] C. Largeot, et al., J. Am. Chem. Soc., 130 (2008) 2730-+ doi: 10.1021/ja7106178.
[118] G. Feng, et al., ACS Nano, 4 (2010) 2382-2390 doi: 10.1021/nn100126w.
[119] C. Merlet, et al., Nat. Mater., 11 (2012) 306-310 doi: 10.1038/nmat3260.
[120] L. Wei, et al., Adv. Energy Mat., 1 (2011) 356-361 doi: 10.1002/aenm.201100019.
[121] R. Mysyk, et al., Electrochemistry Communications, 11 (2009) 554-556 doi: 10.1016/j.elecom.2008.12.035.
[122] T. Lin, et al., Science, 350 (2015) 1508-1513 doi: 10.1126/science.aab3798.
[123] C. F. Liu, et al., Carbon, 145 (2019) 529-548 doi: 10.1016/j.carbon.2018.12.009.
[124] Z. F. Li, et al., ACS Appl. Mater. Interfaces, 7 (2015) 27087-27095 doi: 10.1021/acsami.5b05819.
[125] C. H. Yang, et al., Acs Sustainable Chemistry & Engineering, 6 (2018) 1208-1214 doi: 10.1021/acssuschemeng.7b03492.
[126] C.-C. Hu, W.-C. Chen, Electrochim. Acta, 49 (2004) 3469-3477 doi: 10.1016/j.electacta.2004.03.017.
[127] C. C. Hu, et al., J. Electrochem. Soc., 151 (2004) A281-A290 doi: 10.1149/1.1639020.
[128] C. C. Hu, et al., Nano Lett., 6 (2006) 2690-2695 doi: 10.1021/nl061576a.
[129] L. Y. Chen, et al., Adv. Energy Mat., 3 (2013) 851-856 doi: 10.1002/aenm.201300024.
[130] M. Toupin, et al., Chem. Mater., 16 (2004) 3184-3190 doi: 10.1021/cm049649j.
[131] Y. Zhang, et al., Powder Technol, 262 (2014) 150-155 doi: 10.1016/j.powtec.2014.04.080.
[132] S. L. Chou, et al., Electrochem Commun, 10 (2008) 1724-1727 doi: 10.1016/j.elecom.2008.08.051.
[133] X. Jin, et al., Small, 3 (2007) 1513-1517 doi: 10.1002/smll.200700139.
[134] G. Yu, et al., Nano Lett, 11 (2011) 2905-2911 doi: 10.1021/nl2013828.
[135] Q. Q. Tang, et al., Electrochim Acta, 125 (2014) 488-496 doi: 10.1016/j.electacta.2014.01.139.
[136] S. W. Lee, et al., J. Phys. Chem. C, 118 (2014) 2834-2843 doi: 10.1021/jp411176b.
[137] S. Chen, et al., ACS Nano, 4 (2010) 2822-2830 doi: 10.1021/nn901311t.
[138] J. T. Zhang, X. S. Zhao, Carbon, 52 (2013) 1-9 doi: 10.1016/j.carbon.2012.08.063.
[139] A. Zolfaghari, et al., J. Electroanal. Chem., 697 (2013) 60-67 doi: 10.1016/j.jelechem.2013.03.012.
[140] Y. Lei, et al., Microporous Mesoporous Mater., 110 (2008) 167-176 doi: 10.1016/j.micromeso.2007.10.048.
[141] W. Wei, et al., Phys. Chem. Chem. Phys., 14 (2012) 5966-5972 doi: 10.1039/c2cp23235a.
[142] K. Makgopa, et al., J. Mater. Chem. A, 3 (2015) 3480-3490 doi: 10.1039/c4ta06715k.
[143] C. Ramirez-Castro, et al., J. Electrochem. Soc., 162 (2015) A5179-A5184 doi: 10.1149/2.0221505jes.
[144] X. H. Lu, et al., Adv. Mater., 26 (2014) 3148-3155 doi: 10.1002/adma.201305851.
[145] Y. L. Huang, et al., Small Methods, 2 (2018) 1700230 doi: 10.1002/smtd.201700230.
[146] K. Karthikeyan, et al., Chemistry–An Asian Journal, 9 (2014) 852-857 doi: 10.1002/asia.201301289.
[147] G. Wang, et al., Nano Lett., 11 (2011) 3503-3509 doi: 10.1021/nl202316j.
[148] X. Yu, et al., Adv. Energy Mat., 8 (2018) doi: 10.1002/aenm.201702930.
[149] Y. Guo, et al., Small, 13 (2017) 1701649 doi: 10.1002/smll.201701649.
[150] J. F. Sun, et al., J. Mater. Chem. A, 5 (2017) 9443-9464 doi: 10.1039/c7ta00932a.

[151] M. Ghidiu, et al., Nature, 516 (2014) 78-81 doi: 10.1038/nature13970.
[152] Y. D. Kuang, et al., Advanced Energy Materials, 9 (2019) doi: 10.1002/aenm.201901457.
[153] Y. Xia, et al., Nature, 557 (2018) 409-412 doi: 10.1038/s41586-018-0109-z.
[154] C. J. Chen, et al., Energy & Environmental Science, 10 (2017) 538-545 doi: 10.1039/c6ee03716j.
[155] G. Pike, C. Seager, Physical review B, 10 (1974) 1421 doi: 10.1103/PhysRevB.10.1421.
[156] C. Seager, G. Pike, Physical Review B, 10 (1974) 1435 doi: 10.1103/PhysRevB.10.1435.
[157] L. Hu, et al., Nano Letters, 4 (2004) 2513-2517 doi: 10.1021/nl048435y.
[158] Z. Li, et al., Nature Energy, 5 (2020) 160-168 doi: 10.1038/s41560-020-0560-6.
[159] H. Sun, et al., Science, 356 (2017) 599-604 doi: 10.1126/science.aam5852.
[160] Y. D. Kuang, et al., Advanced Energy Materials, 8 (2018) doi: 10.1002/aenm.201802398.
[161] C. Benoit, et al., Angew Chem Int Ed Engl, 55 (2016) 5318-5321 doi: 10.1002/anie.201601395.
[162] Q. Gao, et al., Energy Environ. Sci., 5 (2012) 9611-9617 doi: 10.1039/c2ee22284a.
[163] Q. Abbas, et al., Faraday Discuss., 172 (2014) 199-214 doi: 10.1039/c4fd00056k.
[164] J. H. Chae, G. Z. Chen, Electrochim. Acta, 86 (2012) 248-254 doi: 10.1016/j.electacta.2012.07.033.
[165] S. Vaquero, et al., International Journal of Electrochemical Science, 8 (2013) 10293-10307 doi.
[166] I. Pineiro-Prado, et al., Front. Mater., 3 (2016) 16 doi: 10.3389/fmats.2016.00016.
[167] M. Lazzari, et al., J. Power Sources, 178 (2008) 490-496 doi: 10.1016/j.jpowsour.2007.12.029.
[168] M. Lazzari, et al., Fuel Cells, 10 (2010) 840-847 doi: 10.1002/fuce.200900198.
[169] N. Jackel, et al., Acs Energy Letters, 1 (2016) 1262-1265 doi: 10.1021/acsenergylett.6b00516.
[170] V. Khomenko, et al., J. Power Sources, 153 (2006) 183-190 doi: 10.1016/j.jpowsour.2005.03.210.
[171] X. Wang, et al., ACS Appl. Mater. Interfaces, 7 (2015) 19978-19985 doi: 10.1021/acsami.5b04677.
[172] Q. Abbas, et al., Electrochimica Acta, 337 (2020) doi: 10.1016/j.electacta.2020.135785.
[173] M. Yu, et al., Angew. Chem. Int. Ed. Engl., 56 (2017) 5454-5459 doi: 10.1002/anie.201701737.
[174] Z. Weng, et al., Angew Chem Int Ed Engl, 52 (2013) 3722-3725 doi: 10.1002/anie.201209259.
[175] X. Zhou, et al., AlChE J., 58 (2012) 974-983 doi: 10.1002/aic.12632.
[176] J. H. Chae, et al., Proceedings of the Institution of Mechanical Engineers Part a-Journal of Power and Energy, 224 (2010) 479-503 doi: 10.1243/09576509jpe861.
[177] K. K. Lian, et al., Electrochemical cell having symmetric inorganic electrodes, Patent No. 5,587,872, December 24, 1996.
[178] K. C. Ng, et al., J. Electrochem. Soc., 156 (2009) A846-A853 doi: 10.1149/1.3205482.
[179] P. Staiti, F. Lufrano, J. Electrochem. Soc., 152 (2005) A617-A621 doi: Doi 10.1149/1.1859614.
[180] X. Zhou, G. Z. Chen, J. Electrochem, 18 (2012) 548-565.
[181] P. Peljo, H. H. Girault, Energy & Environmental Science, 11 (2018) 2306-2309 doi: 10.1039/C8EE01286E.
[182] K. Fic, et al., Energy Environ. Sci., 5 (2012) 5842-5850 doi: 10.1039/c1ee02262h.
[183] K. Jurewicz, et al., Appl. Phys. a-Mater., 78 (2004) 981-987 doi: 10.1007/s00339-003-2418-8.
[184] K. Fic, et al., J. Electrochem. Soc., 162 (2015) A5140-A5147 doi: 10.1149/2.0251505jes.
[185] T. M. Ou, et al., Journal of the Electrochemical Society, 162 (2015) A5124-A5132 doi: 10.1149/2.0191505jes.
[186] W. Shimizu, et al., J. Power Sources, 241 (2013) 572-577 doi: 10.1016/j.jpowsour.2013.05.003.
[187] L. Suo, et al., Science, 350 (2015) 938-943 doi: 10.1126/science.aab1595.
[188] P. Lannelongue, et al., J. Electrochem. Soc., 165 (2018) A657-A663 doi: 10.1149/2.0951803jes.
[189] N. Kumar Thangavel, et al., Water-in-salt electrolytes for high-voltage supercapacitors, 233rd ECS Meeting, 2018.
[190] K. Xu, et al., Journal of the Electrochemical Society, 148 (2001) A267-A274 doi: 10.1149/1.1350665.
[191] S. Pohlmann, et al., Journal of The Electrochemical Society, 162 (2015) A5020-A5030 doi: 10.1149/2.0041505jes.

[192] K. L. Van Aken, et al., Angew Chem Int Ed Engl, 54 (2015) 4806-4809 doi: 10.1002/anie.201412257.
[193] B. Evanko, et al., Acs Energy Letters, 2 (2017) 2581-2590 doi: 10.1021/acsenergylett.7b00828.
[194] Y. Zhao, et al., Chem Soc Rev, 44 (2015) 7968-7996 doi: 10.1039/c5cs00289c.
[195] G. Xiong, et al., Thermal effects in supercapacitors, Springer, 2015.
[196] J. P. Zheng, T. R. Jow, J. Power Sources, 62 (1996) 155-159 doi: Doi 10.1016/S0378-7753(96)02424-X.
[197] R. Vellacheri, et al., Nano Energy, 8 (2014) 231-237 doi: 10.1016/j.nanoen.2014.06.015.
[198] A. J. Roberts, et al., Phys. Chem. Chem. Phys., 15 (2013) 3518-3526 doi: 10.1039/c3cp50359c.
[199] J. Yin, et al., Electrochim. Acta, 88 (2013) 208-216 doi: 10.1016/j.electacta.2012.10.047.
[200] Q. Abbas, F. Beguin, J. Power Sources, 318 (2016) 235-241 doi: 10.1016/j.jpowsour.2016.03.088.
[201] S. P. Pinho, E. A. Macedo, J. Chem. Eng. Data, 50 (2005) 29-32 doi: 10.1021/je049922y.
[202] Q. Abbas, F. Beguin, ChemSusChem, 11 (2018) 975-984 doi: 10.1002/cssc.201701957.
[203] E. J. Brandon, et al., J. Power Sources, 170 (2007) 225-232 doi: 10.1016/j.jpowsour.2007.04.001.
[204] E. Perricone, et al., J. Power Sources, 239 (2013) 217-224 doi: 10.1016/j.jpowsour.2013.03.123.
[205] A. Janes, E. Lust, J. Electroanal. Chem., 588 (2006) 285-295 doi: 10.1016/j.jelechem.2006.01.003.
[206] Y. Korenblit, et al., Adv. Funct. Mater., 22 (2012) 1655-1662 doi: 10.1002/adfm.201102573.
[207] W. C. West, et al., J. Electrochem. Soc., 155 (2008) A716-A720 doi: 10.1149/1.2961044.
[208] R. Lin, et al., The Journal of Physical Chemistry Letters, 2 (2011) 2396-2401 doi: 10.1021/jz201065t.
[209] L. Dagousset, et al., J. Power Sources, 359 (2017) 242-249 doi: 10.1016/j.jpowsour.2017.05.068.
[210] L. Dagousset, et al., Rsc Adv., 5 (2015) 13095-13101 doi: 10.1039/c4ra13933j.
[211] V. Ruiz, et al., Rsc Adv., 2 (2012) 5591-5598 doi: 10.1039/c2ra20177a.
[212] W.-Y. Tsai, et al., Nano Energy, 2 (2013) 403-411 doi: 10.1016/j.nanoen.2012.11.006.
[213] P. H. Huang, et al., Electrochem. Commun., 36 (2013) 53-56 doi: 10.1016/j.elecom.2013.09.003.
[214] Z. F. Lin, et al., Electrochim. Acta, 206 (2016) 446-451 doi: 10.1016/j.electacta.2015.12.097.
[215] Y. Zhou, et al., Rsc Adv., 5 (2015) 71699-71703 doi: 10.1039/c5ra14016a.
[216] R. Newell, et al., Electrochim. Acta, 267 (2018) 15-19 doi: 10.1016/j.electacta.2018.02.067.
[217] C. Z. Yuan, et al., Solid State Ionics, 177 (2006) 1237-1242 doi: 10.1016/j.ssi.2006.04.052.
[218] H. Michel, J. Power Sources, 154 (2006) 556-560 doi: 10.1016/j.jpowsour.2005.10.084.
[219] K. S. Hung, et al., J. Power Sources, 193 (2009) 944-949 doi: 10.1016/j.jpowsour.2009.01.083.
[220] C. Maton, et al., Chem. Soc. Rev., 42 (2013) 5963-5977 doi: 10.1039/c3cs60071h.
[221] M. E. Van Valkenburg, et al., Thermochim. Acta, 425 (2005) 181-188 doi: 10.1016/j.tca.2004.11.013.
[222] G. Xiong, et al., Energy Technology, 2 (2014) 897-905 doi: 10.1002/ente.201402055.
[223] O. Bohlen, et al., J. Power Sources, 172 (2007) 468-475 doi: 10.1016/j.jpowsour.2007.07.021.
[224] T. Liebert, T. Heinze, Bioresources, 3 (2008) 576-601.
[225] M. Zavrel, et al., Bioresour. Technol., 100 (2009) 2580-2587 doi: 10.1016/j.biortech.2008.11.052.
[226] R. S. Hastak, et al., Electrochim. Acta, 59 (2012) 296-303 doi: 10.1016/j.electacta.2011.10.102.
[227] S. K. Kim, et al., Acs Nano, 9 (2015) 8569-8577 doi: 10.1021/acsnano.5b03732.
[228] R. S. Borges, et al., Sci. Rep., 3 (2013) 2572 doi: 10.1038/srep02572.
[229] H. J. Fei, et al., Journal of Power Sources, 266 (2014) 488-495 doi: 10.1016/j.jpowsour.2014.05.059.
[230] J. J. Niu, et al., J. Power Sources, 135 (2004) 332-343 doi: 10.1016/j.jpowsour.2004.03.068.
[231] J. Black, H. A. Andreas, Electrochim. Acta, 54 (2009) 3568-3574 doi: 10.1016/j.electacta.2009.01.019.
[232] S. Fletcher, et al., J. Solid State Electrochem., 18 (2013) 1377-1387 doi: 10.1007/s10008-013-2328-4.
[233] B. W. Ricketts, C. Ton-That, Journal of Power Sources, 89 (2000) 64-69 doi: 10.1016/S0378-7753(00)00387-6.

[234] L. H. Hess, et al., Phys Chem Chem Phys, 21 (2019) 9089-9097 doi: 10.1039/c9cp00483a.
[235] Y. Z. Wang, et al., Journal of Energy Chemistry, 38 (2019) 214-218 doi: 10.1016/j.jechem.2019.04.004.
[236] M. Y. Xia, et al., Nano Energy, 47 (2018) 43-50 doi: 10.1016/j.nanoen.2018.02.022.
[237] J. Kowal, et al., J. Power Sources, 196 (2011) 573-579 doi: 10.1016/j.jpowsour.2009.12.028.
[238] H. A. Andreas, J. Electrochem. Soc., 162 (2015) A5047-A5053 doi: 10.1149/2.0081505jes.
[239] L. B. Chen, et al., Energy Environ. Sci., 7 (2014) 1750-1759 doi: 10.1039/c4ee00002a.
[240] T. Tevi, et al., J. Power Sources, 241 (2013) 589-596 doi: 10.1016/j.jpowsour.2013.04.150.
[241] K. Fic, et al., Electrochim. Acta, 55 (2010) 7484-7488 doi: 10.1016/j.electacta.2010.02.037.
[242] H. Peng, et al., Journal of Power Sources, 435 (2019) doi: 10.1016/j.jpowsour.2019.226800.
[243] K. Ge, G. Liu, Chem Commun (Camb), 55 (2019) 7167-7170 doi: 10.1039/c9cc02424g.
[244] Z. X. Wang, et al., Journal of Materials Chemistry A, 7 (2019) 8633-8640 doi: 10.1039/c9ta01028a.
[245] A. A. Salami, et al., Alumina's effect as blocking layer on self-discharge process: Case study of supercapacitors as energy storage devices, 2019 IEEE PES/IAS PowerAfrica, 2019.
[246] M. A. Kamarudin, et al., Liq Cryst, 45 (2018) 112-121 doi: 10.1080/02678292.2017.1302011.
[247] K. Negita, The Journal of chemical physics, 105 (1996) 7837-7841 doi: 10.1063/1.472564.
[248] V. M. Zamudio, et al., Physica A, 227 (1996) 55-65 doi: 10.1016/0378-4371(95)00379-7.
[249] R. Kishi, et al., Mol Cryst Liq Crys A, 280 (1996) 109-114 doi: 10.1080/10587259608040318.
[250] H. Block, J. P. Kelly, J Phys D Appl Phys, 21 (1988) 1661-1677 doi: 10.1088/0022-3727/21/12/001.
[251] M. A. Davis, H. A. Andreas, Carbon, 139 (2018) 299-308 doi: 10.1016/j.carbon.2018.06.065.
[252] Z. Y. Fan, et al., Nano Energy, 39 (2017) 306-320 doi: 10.1016/j.nanoen.2017.06.048.
[253] Z. S. Wu, et al., J. Am. Chem. Soc., 139 (2017) 4506-4512 doi: 10.1021/jacs.7b00805.
[254] J. P. Randin, E. Yeager, J. Electrochem. Soc., 118 (1971) 711-714.
[255] Y. Yoo, et al., J. Mater. Chem. A, 3 (2015) 11801-11806 doi: 10.1039/c5ta02073e.
[256] Y. Rangom, et al., ACS Nano, 9 (2015) 7248-7255 doi: 10.1021/acsnano.5b02075.
[257] Y. Zhu, et al., Nat. Commun., 3 (2012) 1225 doi: 10.1038/ncomms2234.
[258] J. Lin, et al., Nano Lett., 13 (2013) 72-78 doi: 10.1021/nl3034976.
[259] Y. Yoo, et al., J. Mater. Chem. A, 4 (2016) 5062-5068 doi: 10.1039/c6ta00921b.
[260] N. Islam, et al., Nano Energy, 40 (2017) 107-114 doi: 10.1016/j.nanoen.2017.08.015.
[261] G. F. Ren, et al., Carbon, 71 (2014) 94-101 doi: 10.1016/j.carbon.2014.01.017.
[262] G. F. Ren, et al., J. Power Sources, 325 (2016) 152-160 doi: 10.1016/j.jpowsour.2016.06.021.
[263] M. Cai, et al., ACS Nano, 8 (2014) 5873-5882 doi: 10.1021/nn5009319.
[264] Q. Zhou, et al., ACS Appl. Mater. Interfaces, 8 (2016) 20741-20747 doi: 10.1021/acsami.6b05601.
[265] K. Sheng, et al., Sci. Rep., 2 (2012) 247 doi: 10.1038/srep00247.
[266] Y. Yoo, et al., J. Power Sources, 360 (2017) 383-390 doi: 10.1016/j.jpowsour.2017.06.032.
[267] J. R. Miller, Ieee Electrical Insulation Magazine, 26 (2010) 40-47 doi: 10.1109/Mei.2010.5511188.
[268] N.-C. Lee, Reflow soldering processes, Elsevier, 2002.
[269] C. T. Lhii, El proyecto, http://bga.blog.tartanga.eus/descripcion-del-proyecto/, Acessed on May 5, 2020.
[270] Murata, DMH series, https://www.murata.com/en/products/productdata/8800373800990/MFCDSH1E.pdf, Acessed on May 5, 2020.
[271] Cellergy, Cellergy supercapacitor product specification, https://www.mouser.com/pdfDocs/Cellergy_LineCard.pdf, Acessed on May 5, 2020.
[272] C. Factory, CLC3225 model surface mount type, http://www.clcfactory.co.kr/?act=shop.goods_view&GS=6&GC=GD00, Acessed on May 5, 2020.
[273] Seiko, Cpx capacitors cpx3225a752d, https://www.sii.co.jp/en/me/datasheets/chip-capacitor/cpx3225a752d/, Acessed on May 5, 2020.

[274] K. Ogawa, et al., Nec Technical Journal, 4 (2009) 81-85.
[275] M. Haque, et al., J Phys Conf Ser, 922 (2017) 012011 doi: 10.1088/1742-6596/922/1/012011.
[276] M. Esashi, Journal of Micromechanics and Microengineering, 18 (2008) 073001 doi: 10.1088/0960-1317/18/7/073001.
[277] R. Hahn, et al., Dtip 2009: Symposium on Design, Test, Integration and Packaging of MEMS/Moems, 16 (2009) 292-+ doi: 10.1007/s00542-009-0954-7.
[278] H. Durou, et al., Microsystem Technologies-Micro-and Nanosystems-Information Storage and Processing Systems, 18 (2012) 467-473 doi: 10.1007/s00542-011-1415-7.
[279] R. Hahn, et al., Proc. of PowerMEMS, (2005) 17-20.
[280] L. Liu, et al., Chem Soc Rev, 45 (2016) 4340-4363 doi: 10.1039/c6cs00041j.
[281] F. Shao, et al., Chemical Engineering Journal, (2019) 123692 doi: 10.1016/j.cej.2019.123692.
[282] L. B. Wang, et al., Energy Storage Materials, 27 (2020) 150-158 doi: 10.1016/j.ensm.2020.01.026.
[283] Y. H. Shi, et al., Chemical Engineering Journal, 392 (2020) doi: 10.1016/j.cej.2019.123645.
[284] T. Liu, et al., Journal of Power Sources, 449 (2020) doi: 10.1016/j.jpowsour.2019.227532.
[285] L. Naderi, S. Shahrokhian, Chemical Engineering Journal, 392 (2020) 124880 doi: 10.1016/j.cej.2020.124880.
[286] P. Zhang, et al., Adv Mater, 29 (2017) doi: 10.1002/adma.201604491.
[287] P. P. Zhang, et al., Energy & Environmental Science, 11 (2018) 1717-1722 doi: 10.1039/c8ee00365c.
[288] Y. Yue, et al., ACS Nano, 12 (2018) 4224-4232 doi: 10.1021/acsnano.7b07528.